A Multi-Approach Study of Wave Energy Converters' Effects on Coastal Erosion and Flow Hydrodynamics

by

Mehrdad MORADI

MANUSCRIPT-BASED THESIS BY ARTICLES PRESENTED TO ÉCOLE DE TECHNOLOGIE SUPÉRIEURE IN PARTIAL FULFILLMENT FOR THE DEGREE OF DOCTOR OF PHILOSOPHY
Ph. D.

MONTREAL, 7 JULY, 2025

ÉCOLE DE TECHNOLOGIE SUPÉRIEURE
UNIVERSITÉ DU QUÉBEC

BOARD OF EXAMINERS

THIS THESIS HAS BEEN EVALUATED

BY THE FOLLOWING BOARD OF EXAMINERS:

M. Adrian Ilinca, Thesis Supervisor
Department of Mechanical Engineering, École de technologie supérieure

M. Richard Arsenault, President of the Board of Examiners
Departement of Construction Engineering, École de technologie supérieure

Mme. Marlène Sanjosé, Member of the Jury
Department of Mechanical Engineering, École de technologie supérieure

M. Marcelo Reggio, External Examiner
Department of Mechanical Engineering, École Polytechnique de Montréal

THIS THESIS WAS PRESENTED AND DEFENDED

IN THE PRESENCE OF A BOARD OF EXAMINERS AND PUBLIC

16 JUNE, 2025

AT ÉCOLE DE TECHNOLOGIE SUPÉRIEURE

UNE ÉTUDE MULTI-APPROCHE DES EFFETS DES CONVERTISSEURS D'ÉNERGIE HOULOMOTRICE SUR L'ÉROSION CÔTIÈRE ET L'HYDRODYNAMIQUE

Mehrdad MORADI

RÉSUMÉ

L'érosion des berges représente un défi majeur, accentué par les effets des changements climatiques. La protection des berges nécessite des structures conçues pour dissiper de l'énergie et prévenir la dégradation. Initialement, cet aspect constituait l'objectif principal de cette recherche; cependant, en raison de l'épuisement des combustibles fossiles et du besoin pressant de solutions énergétiques durables, l'orientation de l'étude a évolué vers l'atténuation de l'érosion tout en générant de l'électricité, plutôt que de simplement dissiper l'énergie. Les sources renouvelables, telles que l'énergie marine, suscitent un intérêt croissant. La captation de l'énergie des vagues, en particulier, constitue une alternative prévisible et respectueuse de l'environnement, offrant un double avantage: la production d'électricité et la protection côtière. Cette thèse examine d'abord l'hydrodynamique des jets submergés horizontaux multiples (MHSJ) et l'impact de leur niveau de submersion sur la dissipation d'énergie, ainsi que sur les contraintes de cisaillement au fond et sur les parois latérales qui contribuent à l'érosion, comme présenté au Chapitre 2. Les résultats indiquent que les contraintes de cisaillement de Reynolds et les magnitudes de vorticité augmentent avec la submersion croissante des jets. De plus, il a été constaté qu'une submersion accrue entraîne une réduction de 2,2 % de la contrainte de cisaillement maximale au sol et une diminution de 7,2 % de la contrainte sur les parois latérales. Ensuite, la thèse explore le potentiel des convertisseurs d'énergie des vagues (WEC) à travers trois études distinctes, détaillées dans les Chapitres 3, 4 et 5, en abordant à la fois les impacts techniques et environnementaux de l'énergie des vagues sur les zones côtières de la mer Méditerranée et de la mer Caspienne, ainsi que la production d'énergie du dispositif Wave Dragon.

Le Chapitre 3 se concentre sur le littoral de Palm Beach-Azur, près d'Alger, en mer Méditerranée, avec pour objectif d'exploiter l'énergie des vagues et de réduire l'érosion

côtière. En utilisant des données historiques et la modélisation numérique, l'étude évalue l'impact des WECs sur la réduction de la hauteur des vagues et le dépôt sédimentaire. Les résultats montrent une diminution de la hauteur des vagues de 0,3 mètre et une augmentation du dépôt sédimentaire de 0,8 mètre après l'installation des WECs, démontrant leur capacité à atténuer l'érosion côtière tout en favorisant l'accumulation de sédiments. Cette double fonctionnalité des WECs, combinant production d'énergie et protection côtière, illustre leurs avantages environnementaux et économiques dans la gestion du littoral.

Le Chapitre 4 approfondit cette analyse en explorant le déploiement des WECs au port d'Astara, en mer Caspienne. À l'aide du logiciel MIKE21, l'étude évalue différentes configurations de WECs en prenant en compte plusieurs facteurs : le nombre de dispositifs, leur emplacement, leur agencement structurel et leur orientation par rapport à la direction des vagues. Les configurations analysées incluent deux nombres de dispositifs (11 et 13), trois options d'emplacement (au nord, en face et au sud du port), des agencements linéaires et en quinconce, ainsi que deux orientations (nord-est et sud-est). Les résultats montrent que 13 WECs disposés en quinconce, orientés face à la direction dominante des vagues (nord-est), permettent la plus grande réduction de la hauteur des vagues, abaissant la hauteur significative des vagues (Hs) de 23 à 25 % dans des conditions normales et jusqu'à 36,26 % lors des tempêtes. En termes de défense côtière, un agencement linéaire s'est avéré le plus efficace, offrant une protection des limites de 47,88 % pendant les tempêtes. L'analyse de la gestion des sédiments a révélé qu'une configuration linéaire de 13 dispositifs, orientée vers le nord-est, entraînait l'accumulation sédimentaire la plus importante (0,1231 m sur un an), tandis qu'une configuration en quinconce de 11 dispositifs orientés sud-est présentait une accumulation minimale (0,0358 m), soulignant ainsi le rôle stratégique du placement des WECs dans la réduction de la sédimentation aux abords des ports.

Le Chapitre 5 examine le dispositif Wave Dragon en tant que convertisseur d'énergie des vagues flottant par débordement, en évaluant sa production énergétique et sa résistance structurelle sous différentes conditions de vagues à l'aide de la modélisation Flow3D. En s'appuyant sur des données de vagues en temps réel enregistrées sur une année par une bouée,

la performance du Wave Dragon a été analysée selon quatre scénarios de hauteur de vagues (1,5, 2,5, 3,5 et 4,5 mètres). Les résultats montrent une augmentation significative de la production d'énergie avec la hauteur des vagues, atteignant respectivement 16,03, 25,52, 31,45 et 56,5 MWh par mois. De plus, une hauteur de vague plus élevée entraîne une augmentation de la pression exercée sur le WEC, avec des simulations Flow3D indiquant que la charge de pression passe de $2,97 \times 10^5$ N à 1,5 m à $1,95 \times 10^6$ N à 4,5 m, soit une augmentation d'environ 6,5 fois. Ces résultats mettent en évidence l'évolutivité de la production énergétique et les contraintes structurelles auxquelles les WECs sont soumis dans des conditions de forte houle. En résumé, les études présentées dans les Chapitres 3, 4 et 5 démontrent la viabilité des WECs pour la production d'énergie durable et la protection côtière. Grâce à une modélisation approfondie et à une analyse de scénarios variés, cette thèse confirme que les WECs constituent une solution prometteuse pour une production d'énergie durable et la préservation environnementale dans les environnements marins.

Mots clés: Jets submergés horizontaux multiples (MHSJ), Convertisseurs d'énergie des vagues (WEC), Érosion côtière, Énergie renouvelable, Modélisation numérique, Dépôt de sédiments

A MULTI-APPROACH STUDY OF WAVE ENERGY CONVERTERS' EFFECTS ON COASTAL EROSION AND HYDRODYNAMICS

Mehrdad MORADI

ABSTRACT

Excessive flow energy can lead to erosion, necessitating structures designed to dissipate this energy and prevent degradation. This was the primary focus of this research; however, due to the depletion of fossil fuels and the pressing need for sustainable energy solutions, the direction shifted toward mitigating erosion while simultaneously generating electricity rather than merely dissipating energy. Renewable sources such as marine energy have garnered increasing interest. Wave energy, in particular, offers a predictable and environmentally friendly alternative with dual benefits: power generation and coastal protection. This thesis first investigates the hydrodynamics of Multi Horizontal Submerged Jets (MHSJ), their submergence level's impact on energy dissipation, and the resulting bed and side shear stress that contributes to erosion, as presented in Chapter 2. The results indicate that increasing jet submergence increases the Reynolds shear stress and vorticity magnitudes. Furthermore, it was found that greater submergence leads to a 2.2% reduction in maximum bed (floor) shear stress and a 7.2% decrease in side-wall shear stress.

Subsequently, it explores the potential of Wave Energy Converters (WECs) through three distinct studies, detailed in Chapters 3, 4, and 5, addressing both the technical and environmental impacts of wave energy on coastal zones in the Mediterranean and Caspian Seas as well as the energy output of the Wave Dragon WEC. In Chapter 3, the study focuses on the Palm Beach-Azur coastline near Algiers in the Mediterranean Sea, aiming to harness wave energy and reduce coastal erosion. Using historical data and numerical modeling, WECs were assessed for their impact on wave height reduction and sediment deposition. Results show a decrease in wave height by 0.3 meters and an increase in sediment deposition by 0.8 meters with WECs installed, demonstrating that WECs can mitigate coastal erosion while supporting sediment accumulation. This dual functionality of WECs in energy production and coastal

protection illustrates their potential environmental and economic advantages in coastal management.

Chapter 4 expands on this by exploring WEC deployment at Astara Port in the Caspian Sea. Using the MIKE21 software, the study evaluates various configurations of WECs, considering factors such as device number, placement, structural arrangement, and orientation relative to wave direction. The configurations examined include two device counts (11 and 13), three placement options (north, front, and south of the port), linear and staggered arrangements, and two orientations (facing northeast and southeast). Findings show that 13 staggered WECs facing the dominant wave direction (northeast) achieve the highest wave height reduction, lowering significant wave height (Hs) by 23–25% under typical conditions and up to 36.26% during storm events. A linear arrangement proved most effective in coastal defense, providing 47.88% boundary protection during storms. Sediment management analysis revealed that a 13-device, linear configuration facing northeast induced the highest sediment accumulation at 0.1231 m over one year, while a staggered 11-device southeast configuration showed minimal sediment buildup at 0.0358 m, underscoring the role of strategic WEC placement in reducing sedimentation near harbor entrances.

Chapter 5 investigates the Wave Dragon as a floating overtopping WEC device for its energy output and structural resilience under various wave conditions using Flow3D modeling. Based on year-long real-time wave data from a buoy, the Wave Dragon's performance was analyzed across four-wave height scenarios (1.5, 2.5, 3.5, and 4.5 meters). Results demonstrate a significant increase in energy output with wave height, yielding 16.03, 25.52, 31.45, and 56.5 MWh per month, respectively. Additionally, increased wave height resulted in higher pressure on the WEC, with Flow3D simulations indicating that pressure load rose from 2.97×10^5 N at 1.5m to 1.95×10^6 N at 4.5m, approximately a 6.5-fold increase. These findings highlight the scalability of energy output and the structural demands on WECs in high-wave conditions.

These studies, presented in Chapters 3, 4, and 5, underscore the viability of WECs in sustainable energy production and coastal defense. Through comprehensive modeling and scenario analysis, this thesis confirms WECs as a promising sustainable energy and environmental preservation solution in marine contexts.

Keywords: Multi-Horizontal Submerged Jets (MHSJ), Wave Energy Converters (WEC), Coastal Erosion, Renewable Energy, Numerical Modeling, Sediment Deposition

TABLE OF CONTENTS

LIST OF TABLES

Page

LIST OF FIGURES

Page

LIST OF ABREVIATIONS

ACM	Acoustic Current Meter
ADCP	Acoustic Doppler Current Profiler
CFD	Computational Fluid Dynamics
MHSJ	Multi-horizontal Submerged Jets
NRMSE	Normalized Root Mean Square Error
RANS	Reynolds-Averaged Navier–Stokes
RMSE	Reynolds-Averaged Navier–Stokes
SWAN	Simulating Waves Near-shore (Third-generation wave model)
SW	Shallow Water Model
VOF	Volume of Fluid
WEC	Wave Energy Converter
WD	Wave Dragon

LIST OF SYMBOLS

C	Chezy coefficient ($m^{0.5}\ s^{-1}$)
Fku	Streamwise flux of turbulent kinetic energy ($m^3\ s^{-3}$)
F_{kv}	Vertical flux of turbulent kinetic energy ($m^3\ s^{-3}$)
g	Acceleration due to gravity ($m\ s^{-2}$)
H	Hole size
h	Width of the jet holes (m)
H_t	Tail-water depth (m)
I(t)	Detection function
i	Quadrant number (1, 2, 3, 4)
K(TKE)	Turbulent kinetic energy ($m^2\ s^{-1}$)
Q	Quantity of flow ($m^3\ s^{-1}$)
Q_1	Outward interaction events
Q_2	Ejection events
Q_3	Inward interaction events
Q_4	Sweep events
R	Hydraulic radius (m)
S	Channel slope
$S_f\ (Q_i, H)$	Contribution of shear stress for i'th quadrant within the hole size H
U_j	Jet flow velocity
u′, v′, w′	Fluctuating components of velocity in x, y and z directions ($m\ s^{-1}$)
u'_{rms}, v'_{rms}, w'_{rms}	Root mean square of instantaneous turbulent velocity fluctuations ($m\ s^{-1}$)

$u'v'$	Time-averaged Reynolds shear stress ($m^2\ s^{-2}$)
X, Y, Z	Cartesian axis directions
$<u'v'>Q_i$, H	Contribution of i'th quadrant in total Reynolds shear stress ($m^2\ s^{-2}$)
γ	Specific gravity of water ($kg\ m^{-3}$)
ΔE	Elevation difference between the head tank and downstream water level
η	Energy dissipation percentage
τ	Shear stress ($kg\ m^{-2}$)
τ_0	Average shear stress ($kg\ m^{-2}$)
ρ	Density of water ($kg\ m^{-3}$)
$N(\omega, \theta)$	Wave action density spectrum ($m^2\ s$)
ω	Angular wave frequency ($rad\ s^{-1}$)
θ	Wave direction (degrees or radians)
c_x, c_y	Wave propagation speed in the x and y directions ($m\ s^{-1}$)
c_ω	Propagation speed in the frequency domain (s^{-1})
c_θ	Propagation speed in the directional domain (degrees/s or rad/s)
S	Source and sink terms ($m^2\ s^{-3}$)
S_{nl4}	Nonlinear quadruplet wave-wave interaction term ($m^2\ s^{-3}$)
S_{nl3}	Nonlinear triad wave-wave interaction term ($m^2\ s^{-3}$)
S_{in}	Wind input term ($m^2\ s^{-3}$)
S_{wc}	Whitecapping dissipation ($m^2\ s^{-3}$)
S_{bot}	Bottom friction dissipation ($m^2\ s^{-3}$)
S_{brk}	Depth-induced wave breaking dissipation ($m^2\ s^{-3}$)
J_x, J_y	Wave energy flow components in x and y directions ($W\ m^{-1}$)

$E(\sigma, \theta)$	Directional spectral energy density (m^2 s)
σ	Wave frequency (Hz or s^{-1})
J	Total wave power (W m^{-1})
d	Water depth (m)
L_o	Offshore wavelength (m)
K_t	Wave transmission coefficient
K_s	Shoaling coefficient
$A(\omega, \theta)$	Wave power spectrum density
$\Delta x, \Delta y$	Distance between computational nodes (m)
Q_b	Friction due to wave breaking (dimensionless)
k	Wave number (1 m^{-1})
α	Energy dissipation coefficient (dimensionless)
γ_1, γ_2	Constant coefficients (dimensionless)
λ	Wavelength (m)
H_s	Significant wave height (m)
ΔH_s	Change in significant wave height (m)
T	Wave period (S)
μ	Dynamic viscosity (kg m^{-1} s^{-1})
ν	Kinematic viscosity (m^2 s^{-1})
P	Pressure (Pa)
u, v, w	Velocity components in the x, y, and z directions (m s^{-1})
ε	Turbulent dissipation rate (m^2 s^{-3})
η	Efficiency factor

INTRODUCTION

Context and Motivation

Beach protection often requires a regional solution. Ships make considerable world trade through ports constructed on the shores. These waterways require consolidation, maintenance, and protection. Waves are the most dynamic and important phenomena in the coastal strip and the most significant factor in determining beach geometric position and transition. They also significantly impact the ports' design and coastal protection structures (Harman et al., 2015).

A wave is an oscillation that travels without transferring matter. It carries energy from one place to another. Sea waves near shores often get their energy from the local winds that blow near the shore and from severe storms that happened in distant locations in previous days. The stored energy is dissipated through friction and turbulence and has an intensity that depends on the waves' nature and the water's depth (Golitsyn, 2010).

A considerable amount of wave energy is dissipated when approaching the shore, leading to the formation of coasts and the movement of seabed sediments towards the shore, the sea, or along the coast. Sediment transport can cause severe damage to coastal structures, change coastal topography, and affect environmental processes. Moreover, scouring and erosion can seriously damage the foundations of buildings, roads, highways, underground pipelines, coastal embankments, and other coastal structures (Putnam & Johson, 1949).

Building coastal protective structures primarily aims to save the coast by controlling the allowable wave height transmitted along the shore. There is no global standard with guidelines for defining the maximum acceptable height for high-risk waves. The degree of wave protection and engineering design depends on the project, site specifications, environmental and economic conditions, materials in the area, risk margin, and structure application type (Vaidya et al., 2015).

When waves hit a coastal structure, part of the incident wave energy is reflected, some energy is dissipated through the breakwater, and the residual effect is transferred behind the breakwater. Breakwaters are classified into two categories based on their degree of protection, Fully Protective Breakwaters (rock mass, caisson, vertical composite, etc.) and Partially Protective Breakwaters (porous, slotted, pile, etc.). One of the main objectives of coastal engineering is to design ports that reduce the incoming wave energy to the protected area. Vertical penetrating walls, often called wave plates, are a good option for maintaining water circulation inside the port. Permeable breakwaters do not disrupt current or wave activity or entirely stop sediment transport. These characteristics make permeable breakwaters more environmentally compatible and better at maintaining regional balance over the long term than rock mass breakwaters (Baird & Hall, 1985).

Wave Energy Converter (WEC) devices are perfect examples of permeable breakwater structures. WECs can serve a dual role in extracting marine energy by converting it into electrical energy and as a defense tool against marine erosion. Therefore, it can be noted that WECs justify their efficiency in energy production and economic and environmental profitability due to coastal protection (Falnes, 2007).

Among the renewable energies experiencing considerable development, marine energies need more attention. The ocean covers 71% of the Earth's surface and is an under-utilized blue energy source. The expected increase in the number and intensity of storms due to climate change, current erosion, flooding along coastal areas, and a push for corporate environmental responsibility along coastal regions pave the way for future increased utilization of marine energy projects. To avoid negative impacts, WECs should be climate-proof (i.e., characterized by low sensitivity to sea level rise and strong waves), environmentally friendly, and with low visual impact on the horizon (i.e., submerged or low-crested). Various types of WECs have different mechanisms and technologies for converting mechanical energy into electricity. These technologies have been reviewed by many authors (Drew et al., 2016; Falcão, 2010; McCormick, 2007; Thorpe, T.W., 1999).

Another vital feature of WECs is their influence on the flow hydrodynamics near coastlines. Numerous numerical and experimental studies have been conducted to assess the hydrodynamic impacts of coastal protection structures on near-shore flow characteristics. Recent research has studied three arrays of configurations with 12 WECs on the western coasts of Ireland to measure the influence of these structures on near-shore wave climate and generated power. They noted a decrease of less than 1% in wave height and wave power between 1 and 3 km from the coast. They also reported a wave height decrease of 0.1% and a wave power decline of 0.2% at 100 to 300 meters from the coastline (Atan et al., 2019).

A sensitivity analysis of SWAN models on WEC arrangement and features revealed 30% and 15% wave height reductions in two tested scenarios involving wave energy converter structures (Chang et al., 2016). In another study, field data from wave measurement devices were used to validate a proposed SWAN model, revealing that the influence of the WEC on the wave field and flow structure was most pronounced 40 m downstream of the wave energy unit, where a maximum wave height reduction of 20% was observed (Contardo et al., 2018).

Flow regime alterations imposed by a wave farm located at the southwestern coasts of England were investigated using SWAN and ROMS models by Greaves & Iglesias, 2017. They studied WECs' effects on wave radiation stresses, bed shear stresses, bottom frictions, and sediment transport. The results confirmed that the wave farm influences gradients of bottom shear stress, which leads to adjusting current velocity and wave heights (by around 5 and 10 cm). The observed flow interactions and bed stress were reported as the main factors affecting sediment transport patterns and, consequently, morphological changes.

Apart from the impacts of WECs on the flow field and, consequently, the morphology of a region, it is essential to examine the region's potential in terms of wave energy. This can be considered as the first step of the project implementation. Numerous studies have focused on the marine power potential of a region calculated from wave characteristics such as wave height and wave period (Gonçalves et al., 2014; Guillou & Chapalain, 2015; Iglesias & Carballo, 2009a; Mendes et al., 2012).

A study on the wave potential in the Caribbean Sea validated a 30-year wave hindcast of the region using altimetry (Globwave) and buoy (DIMAR) data. The findings indicated that the Caribbean Low-Level Jet region, characterized by easterly wind speeds of 13 m/s, offers the best potential for wave energy extraction, with values ranging from 8 to 14 kW/m (Appendini et al., 2015). Another high-resolution wave model was used to estimate the available wave power potential in Puerto Rico and the US Virgin Islands, revealing a potential of 10 to 12 kW/m. These findings suggest that the sites are theoretically suitable for wave energy harvest projects (Garcia & Canals, 2015). The extractable wave energy along the Atlantic coast of Morocco was studied using a 44-year data series at 23 points and a statistical analysis of significant wave heights. The study identified the central area of the Atlantic Moroccan coast, characterized by the largest significant wave heights, as the optimal region for wave energy harvest, with an annual average wave power exceeding 25 kW/m (Sierra et al., 2016).

To fully capitalize on the potential benefits offered by Wave Energy Converters (WECs), it is imperative to strategically deploy them in regions vulnerable to coastal erosion. Approximately 20% of the global coastline comprises sandy beaches, with nearly 70% experiencing ongoing erosion, 20% maintaining stability, and 10% displaying signs of sediment accumulation. These coastal regions, endowed with strategic significance and as prominent tourist destinations, hold substantial economic value and represent an invaluable natural landscape heritage. This study addresses the erosion and sedimentation challenges confronting the Palm Beach Azur and the Astara port, situated along the Algerian coasts and the Caspian Sea. Notably, our approach adopts a comprehensive perspective, and the insights gained from our investigation hold the potential for widespread applicability across diverse ports and coastlines dealing with erosion and sediment accumulation issues.

The main contribution of this project lies in addressing the dual problem of protecting the shorelines while producing renewable energy. Our primary goal is to comprehensively evaluate shoreline dynamics before and after the installation of protective structures while also assessing their impact on hydrodynamics within the area and modifying the port's design to

overcome existing port closure challenges. Additionally, we analyzed the WECs' potential for energy generation for different waves in the Caspian Sea. Notably, the significance of this research extends beyond the Astara Port and Palm Beach Azur. The methodologies and insights garnered can serve as a valuable template for addressing erosion and port blockage issues in regions worldwide, making it a valuable contribution to the broader field of coastal management and sustainable energy generation.

Objectives

The primary objective of this thesis is to evaluate the dual functionality of WECs for both renewable energy production and coastal erosion mitigation. While WECs are traditionally studied for their energy output, their influence on wave dynamics and sediment transport offers a promising opportunity for integrated coastal zone management. As the first step of this research, submerged jet-induced dissipation systems were studied, broadening the scope of technologies that could help protect vulnerable rivers downstream of hydropower stations while enabling energy recovery.

To achieve this overarching goal, the study pursues the following specific objectives:

Wave Energy Converter (WEC)-Focused Objectives:

- Investigate the hydrodynamic and morphodynamic impacts of WEC deployment under various wave climates and bathymetric conditions, emphasizing their capacity to attenuate wave energy and mitigate coastal erosion.
- Determine optimal WEC array configurations (e.g., layout, number, orientation) that maximize wave energy extraction while minimizing unwanted effects on sediment transport and shoreline dynamics.
- Develop and validate a coupled multi-scale modeling framework combining MIKE21 for large-scale wave transformation and FLOW-3D for high-resolution hydrodynamics near WECs.

- Based on their performance, provide case-specific recommendations for WEC deployment at two pilot sites, Palm Beach-Azur (Algeria) and Astara Port (Iran).

Complementary Objective – Submerged Jet Energy Dissipators:

- Conduct a targeted analysis of submerged jet energy dissipators, focusing on their influence on energy dissipation, bed and wall shear stress reduction, and river stability downstream of hydropower stations.

Although both WECs and jet dissipation devices were considered in the early stages of this research, the decision was ultimately made to pursue a deeper investigation into WECs for several reasons. First, WECs offer a unique dual benefit: dissipating wave energy and generating renewable electricity, aligning more directly with energy transition goals. Second, their passive nature and modularity make them more adaptable for integration into different coastal contexts. In contrast, while effective in river protection downstream of hydropower stations, submerged jet dissipation systems do not generate energy and only dissipate it through submerged hydraulic jumps and heat. As such, the focus of the thesis shifted toward evaluating, modeling, and optimizing WEC configurations that balance energy production with shoreline protection.

Original Contributions

This thesis makes the following original contributions to the field of coastal protection and renewable energy integration:

- Jet-induced dissipation modeling: The study proposes and evaluates a novel active energy dissipation technique using submerged turbulent jets to reduce erosion downstream. It investigates how hydrodynamic behavior, turbulence generation, and jet submergence impact shear stress values.

- Wave Energy Converters (WECs) for erosion control: It explores using WEC arrays as passive coastal protection structures, focusing on their hydrodynamic and morphodynamic effects in reducing wave impact and sediment displacement in different coastal settings using two different models, including SWAN and MIKE21.
- Multi-scale modeling framework: The research develops an integrated simulation approach combining MIKE21 for large-scale wave transformation and FLOW-3D for high-resolution near-field modeling. This approach enables a detailed assessment of device–wave interactions and the amount of energy produced by different waves.
- Site-specific design recommendations: By applying the proposed methods to Palm Beach-Azur (Algeria) and Astara Port (Iran), the study delivers context-sensitive insights and practical guidance for future deployments in erosion-prone or energy-deficient coastal zones.

Thesis Structure

Chapter 1 outlines the methodological framework that guides the entire research. It introduces the multi-scale modeling approach developed to evaluate the hydrodynamic, morphodynamic, and energy-related impacts of coastal energy dissipation systems. The first chapter presents the rationale for selecting a combined modeling strategy integrating large-scale wave transformation (via MIKE21 and SWAN) with high-resolution hydrodynamic and turbulence modeling (via FLOW-3D). It then describes how this framework is applied across different spatial and temporal scales, enabling the assessment of device performance, wave attenuation, and sediment dynamics under realistic and idealized conditions. This foundational chapter provides the technical basis for the simulations and analysis presented in the following chapters.

Chapter 2 focuses on the hydrodynamics of flow downstream of submerged jets and river erosion mitigation, which was initially the primary focus of this research. However, as the study progressed, the thesis shifted toward investigating wave energy devices and their role in coastal erosion protection and energy generation rather than river erosion control and energy

dissipation. This chapter analyzes a stilling basin with multiple horizontal submerged jets emerging from two layers as an energy dissipation structure for hydropower stations. Laboratory velocity measurements were conducted to analyze the three-dimensional flow structure of submerged jets and evaluate the effects of downstream submergence on the flow field. The findings revealed that greater jet submergence increased Reynolds shear stress and vorticity magnitudes. Additionally, increasing submergence resulted in a 2.2% decrease in maximum bed (floor) shear stress and a 7.2% reduction in side-wall shear stress.

The second article, described in Chapter 3, proposes using Wave Energy Converters (WECs) to mitigate coastal erosion along the Palm Beach-Azur coastline near Algiers. It demonstrates their effectiveness in reducing wave height and promoting sediment deposition.

In the third article described in Chapter 4, the impact of different configurations of WECs at Astara Port in the Caspian Sea is studied by evaluating the effects of number, placement, arrangement, and orientation of WECs on wave height reduction and sediment management.

The fourth article analyzes the Wave Dragon’s energy output and structural resilience, as detailed in Chapter 5. FLOW-3D modeling examines performance under different wave conditions and quantifies the relationship between wave height, energy generation, and the forces exerted on the device.

Finally, we present this thesis's conclusions, emphasizing the original contributions, the limitations of our work, and recommendations for further studies.

CHAPITRE 1

METHODOLOGY

1.1 Introduction

This research addresses the growing challenge of erosion, a phenomenon increasingly intensified by the impacts of climate change. Accelerated sea level rise, intensifying storm surges, and fluctuating flow regimes are amplifying the degradation of riverbanks and coastlines, posing significant risks to infrastructure, ecosystems, and communities. In response, this thesis examines erosion mitigation through a dual-phase approach that encompasses both riverine and coastal environments. The first phase of this thesis focuses on riverine erosion mitigation through experimental investigation of stilling basins equipped with Multi-Horizontal Submerged Jets (MHSJ). Specifically, the study examines how submergence levels affect flow behavior, energy dissipation, and shear stress distribution—factors crucial in minimizing flow energy and downstream erosion. The methodology and technical specifications of this laboratory experimental study on submerged jet stilling basins are comprehensively detailed in Chapter 2.

The second phase addresses coastal erosion by evaluating the performance of Wave Energy Converters (WECs). These devices, developed for renewable energy production, are examined for their dual role in sustainable development: not only do they harness wave energy for electricity generation, but they also serve as coastal protection systems by mitigating wave energy along vulnerable shorelines. To conduct this investigation, numerical modeling was adopted as the primary methodological tool. Studying oceanic motion through equation-based solutions is inherently complex due to the vast and dynamic nature of marine environments. Direct observation and measurement of physical and chemical parameters are often constrained by scale and variability, while laboratory models are costly and struggle to replicate real-world water dynamics. As a result, numerical modeling has become the preferred approach, offering a means to solve governing equations and analyze hydrodynamic phenomena (Newmann, 2018).

This study utilized the SWAN (Simulating WAves Near-shore) model to simulate wave propagation, transformation, and sediment deposition in Palm Beach, Algeria. However, the MIKE 21 modeling system was selected for the subsequent study due to SWAN's limitations, as it offers fully integrated capabilities for both wave and hydrodynamic simulations. The two-dimensional hydrodynamic model MIKE21 and its subsets were used to model wave and flow patterns, incorporating wind speed, wind direction, wave height, wave period, and bed topography. The data was sourced from previous measurements by relevant organizations and experimental studies conducted near the Astar port. Furthermore, FLOW-3D, a computational fluid dynamics (CFD) model, was applied to analyze localized hydrodynamic behaviors, particularly around the wave dragon energy converter. By integrating these models, this research comprehensively assessed hydrodynamic conditions, energy generation, coastal protection, and wave energy potential in the study areas.

1.2 Research Method

As a spectral wave model, SWAN accounts for wind-wave interactions, refraction, and wave breaking. However, unlike integrated modeling systems like MIKE21, SWAN is limited to wave modeling and does not inherently simulate hydrodynamic processes such as currents or water level variations. To overcome this limitation, SWAN is typically coupled with Delft3D for comprehensive hydrodynamic analysis. This modular structure, while effective, introduces additional complexity in model setup and calibration compared to more integrated platforms.

The initial phase of the MIKE21 simulations involves developing a comprehensive global model of the Caspian Sea, calibrated using experimental data. This model provides a detailed representation of wave dynamics across the region. Its outputs, generated using a coarser mesh, are then used as boundary conditions for the more detailed local model. The local model was developed to assess the impact of Wave Energy Converters (WECs) on flow patterns, decreased transmitted wave heights, bed level changes, and coastal erosion near the Astara port. Simulations were conducted with WECs placed to the north, in front of, and south of the

port to determine optimal locations. Additionally, alternative port layouts were tested to evaluate their effectiveness in reducing erosion and sedimentation near the port.

To conduct a more detailed assessment of the impact of energy converters on flow characteristics, we utilized the FLOW-3D software. This approach enabled us to delve deeper into understanding the intricate interplay between energy converters and flow dynamics at a more refined level.

1.3 MIKE 21 and SWAN Models

While SWAN is limited to wave modeling and does not solve hydrodynamic equations, hydrodynamic simulations in MIKE21 employ the Hydrodynamic (HD) module, which solves the depth-averaged shallow water equations to compute water levels and current velocities. Both MIKE21 and SWAN utilize the Spectral Wave (SW) module for wave modeling, which solves the spectral wave action balance equation to simulate the growth, transformation, and decay of wind-generated waves. Below, we present the governing equations used in the SW (Spectral Wave) module for both SWAN and MIKE21 (DHI MIKE. Spectral Waves FM, Spectral Wave Module User Guide, 2017).

1.3.1 Spectral Wave (SW) module of MIKE21 and SWAN

In hydrodynamic studies of offshore projects, the primary annual wave characteristics, such as significant wave height (Hs), peak wave period (Tp), and wavelength (L), are typically derived from statistical analyses of deep-water wave data, including buoy measurements. However, for the design of offshore structures and the analysis of coastal sedimentation, it is crucial to estimate near-shore wave parameters, as waves transform due to shoaling, refraction, diffraction, breaking, and bottom friction. To accurately model these processes, the wave module solves the spectral wave action balance equation, which accounts for source terms (e.g., wind input, nonlinear wave-wave interactions) and sink terms (e.g., white capping dissipation, bottom friction). The spectral formulation is used to represent the stochastic nature of sea waves, describing how wave energy is distributed across

frequencies and directions (DHI MIKE. Spectral Waves FM, Spectral Wave Module User Guide, 2017).

The two-dimensional form of the energy transfer equation is as follows:

$$\frac{\partial E}{\partial t}+\frac{\cos\Theta}{C}\frac{\partial(E.C.C_g)}{\partial x}+\frac{C_g}{C}+\frac{\sin\Theta}{C}\frac{\partial(E.C.C_g)}{\partial y}+\frac{C_g}{C}\left(\sin\Theta\frac{\partial C}{\partial x}-\cos\Theta\frac{\partial C}{\partial y}\right)\frac{\partial E}{\partial\Theta}=S \quad (1.1)$$

Whose variables are defined as follows:

X, Y: Cartesian coordinates in a two-dimensional space

E (t,x,y,f,θ): Two-dimensional energy spectrum of frequency-directional wave

t: time

θ: Wave direction angle

C_g: Group wave velocity

C: Wave propagation velocity

S: Sink and source

1.3.2 MIKE21 Modeling Process for Astara Port

The modeling process involved setting up and validating a two-dimensional hydrodynamic model to analyze wave and flow patterns around Astara Port in the Caspian Sea. The following steps were undertaken:

1. **Data Collection**

- Coastal geography and seabed topography were gathered.
- Wind speed and direction data were obtained from ECMWF.
- Wave characteristics, including height, direction, and current velocity and direction, were gathered from previous experimental studies conducted in 2013 (ADCP data) to validate the simulation results.

2. **Global Model Setup**

- Defined as the boundaries of the Caspian Sea.

- An unstructured mesh was applied to deep-water areas.
- Rectangular grids were used in the southern coastal regions for higher accuracy of results.
- The global model was calibrated using the experimental data.

3. Local Model Configuration

- Model boundaries were defined based on the project requirements, specifically near Astara Port.
- Boundary conditions for the local model were extracted from the calibrated global model.

4. Validation & Refinement

- MIKE21 outputs were validated against experimental measurements at 10m and 25m depths.
- Flow velocity, flow direction, wave height, and wave direction were compared with experimental data.

5. Port Redesign and Sediment Management Strategy

- A new port layout was proposed to redirect high-velocity flows away from the port entrance.
- The redesign was intended to mitigate sediment accumulation and reduce the frequency of port closure due to sedimentation.

6. Integration of Wave Energy Converters (WECs)

- WECs were imported into the local model to assess their impact on wave attenuation and coastal protection.
- Multiple WEC scenarios were tested by varying the number, orientation, and arrangement of devices.
- Configurations included linear and staggered layouts, each evaluated under different wave conditions over the course of one year.

- The influence of each setup on wave transformation, sediment transport, and shoreline stability was studied to identify optimal solutions for both energy generation and erosion control.

1.4 FLOW-3D Model

Due to the limitations of MIKE21 in modeling dynamic structures and its primary suitability for large-scale coastal simulations, the study transitioned to using the 3D CFD tool FLOW-3D to capture detailed wave–structure interactions and accurately compute power output by resolving the flow passing through individual turbines. The governing equations in this model are the Navier-Stokes equations, with FLOW-3D offering five turbulence models. (Flow Science, Inc., FLOW-3D User Manual). FLOW-3D has been used to investigate the power generation of individual WEC units and to understand the hydrodynamics of flow near them, as well as the impacts of waves on the structure, including the pressure and shear forces exerted on each wave energy device.

Another reason for employing CFD analysis is that most previous studies have modeled the Wave Dragon wave energy converter as a static object. However, this study modeled it dynamically with a mooring system attaching the device to the seabed. Modeling in a dynamic environment introduced challenges in accurately calculating the exact flow passing through each turbine. However, this issue was addressed using dynamic history probes, which enabled the calculation of instantaneous flow velocity at each point. The trapezoidal method was then employed to determine the flow quantity for each turbine, enabling the estimation of the generated power for each unit.

Four wave heights, 1.5m, 2.5m, 3.5m, and 4.5m, were replicated to model the waves in the MIKE21 simulation near Astara port. The wave types were then identified using the wave theory diagram, and the simulated waves were verified against theoretical wave conditions. A comprehensive discussion of governing equations of FLOW-3D, wave modeling techniques,

validation methods, and the influence of wave height on power generation and forces exerted on WEC devices is provided in Chapter 5.

1.5 Experimental Data and Research Area

For this study, two geographical sites, Astara, Iran, and Palm Beach Azur, Algeria, were selected due to practical feasibility. Both locations are coastal areas that have been experiencing severe erosion and sedimentation, posing significant risks to infrastructure, tourism, and navigation. In addition to their vulnerability, these sites are characterized by moderate to high wave heights, making them ideal locations for evaluating the dual role of WECs in energy production and shoreline protection. Furthermore, these sites were prioritized due to the availability of reliable field data and environmental parameters, as provided through previous studies, which enabled accurate model calibration and validation. Although each site has distinct physical characteristics, the main challenges they illustrate are coastal retreat due to high-energy waves, sediment transport, and sediment accumulation near ports, which are common across many coastal environments. Consequently, the methodological framework and findings developed in this research can be generalized and applied to similar erosion-prone coastal regions worldwide.

1.5.1 Astara Port, Caspian Sea

Due to its geographic location, depth, and various atmospheric systems, strong winds and storms form on the Caspian Sea, creating high waves. In most cases, the average temperature of the sea is higher than on the coast, and only in the second half of spring and summer is the opposite. The water temperature of the Caspian Sea's northern, central, and southern parts varies in different seasons. Latitude and different water depths are the main reasons for this temperature difference. The maximum temperature in the warmest month of the year is 30 to 39 degrees Celsius, and the minimum temperature in the coldest month of the year is 1 degree Celsius. The average rainfall in the southern Caspian Sea is 1901 mm yearly (Rodionov, 1994).

Wind Waves

Multiple factors, including coastal geography, variations in land and sea temperatures, barometric pressure fluctuations, and seasonal changes, shape the direction and velocity of the winds over the Caspian Sea. Throughout winter, powerful cold winds blow southward from Russia, often affecting the Sea's conditions. During this season, anticyclonic winds from southern Siberia influence the sea, resulting in lower air pressure in the southern area. In contrast, summers witness consistent low-pressure winds across both the sea and the adjacent land. These prevailing winds predominantly move from the sea towards the coast, maintaining relatively uniform air temperatures across the sea. Consequently, this atmospheric interplay generates wave patterns with a prevailing northwest direction, particularly influencing the southern reaches of the sea (Lama et al., 2022).

Water Currents

These streams that exist in the Caspian Sea are divided into two general categories:

- Irregular currents: These currents rely on wind speed, duration, and direction. Irregular sea currents are less predictable and can vary widely regarding direction, speed, and intensity.

- Regular currents: These currents are typically caused by factors such as the Earth's rotation (Coriolis effect), temperature and salinity differences, and prevailing wind patterns. They are relatively stable over time and follow specific paths or routes. Other factors, such as the effect of river water flow, different concentrations of sea water, coast morphology, ridges, and roughness of the sea, can also affect these regular currents.

Field Data Measurement in Astara Port

In the designated study area, acquiring precise and pertinent data is critical. To this end, flow, wind, and bathymetry data are obtained from sources such as the Ports and Maritime Organization. To set up the model effectively, coastal geography and seabed topography are

essential data. Additionally, comprehensive statistics on wind speed, wind direction, flow velocity, and flow direction specific to the region are vital, as they significantly influence wave patterns and the overall hydrodynamics. Furthermore, records of annual wave characteristics, including parameters like wave height, period, and direction, are indispensable for a comprehensive understanding of wave behavior and its interactions with the coastline. In addition to the mentioned data needed to establish the model, calibrating the numerical model results also requires experimental data. Simulation studies near the Astara Port have involved several measurements in the South Caspian Sea. On the coast of Astara port, flow features were measured in 2013 at depths of 10 and 25 meters using Acoustic Doppler Current Profilers. The data from this measurement accurately records waves and current information in deep water (ISWM, Iranian Sea Wave Modeling, 2008).

Astara Climate

Astara, located on the west coast of the Caspian Sea, has a temperate and humid climate. Humid winds blow from the northwest in winter, the east in spring, and the west in summer and autumn. In the cold season, low-pressure systems cause warm southern and southwestern winds. Table 1.1 illustrates more climatic details about the Astara region.

Table 1.1 Astara climate parameters

Parameter	Value	Parameter	Value
Mean Annual rainfall	1380 mm	Mean Temperature	17.3° C
Maximum Annual rainfall	1780 mm	Average Maximum Temperature	26.1° C
Annual Rainfall Range	700-2000 mm	Average Minimum Temperature	6.2° C
Annual Rainy Days	120 days	Average Annual Temperature	16° C
Relative Humidity	75-85%	Annual Glacial Days	11 days

Astara Port

At the Astara port, the breakwater serves several essential purposes, including facilitating ship docking, acting as an international transportation hub, and serving as a vital trading point. Like many ports worldwide, Astara Port faces sedimentation issues that can lead to temporary closures, requiring regular dredging to maintain navigability and operational efficiency. The exact location of the port is presented in Table 1.2:

Table 1.2 Location of Astara Port

Latitude	Longitude
38° 26' N	48° 52' E

1.5.2 Palm Beach-Azur

Palm Beach-Azur is a coastal region located along the Mediterranean Sea near Algiers, the capital of Algeria. This region is significant for its potential in marine energy exploration and coastal protection. The Mediterranean is fully enclosed and bordered by numerous countries, which creates a unique, semi-enclosed sea system with complex hydrodynamic and atmospheric conditions. The geographical positioning of Palm Beach-Azur along the Algerian coastline offers significant advantages for wave energy utilization, due to favorable wave patterns and a strategic location for minimizing coastal erosion (Algeria - Summary | Climate Change Knowledge Portal, n.d.).

Climate of Palm Beach-Azur

The climate along the Algerian coast, particularly in the Palm Beach-Azur region, is Mediterranean, characterized by hot, dry summers and mild, wet winters. Rainfall is primarily concentrated in winter, while summers are typically dry. This seasonal variation in rainfall significantly impacts wave heights and coastal sediment dynamics, with stronger wave action occurring during the winter. Both local geographic features and broader atmospheric conditions shape wind patterns along the Algerian coast. During winter, strong winds are often

channeled from the north and northwest across the Mediterranean, generating higher waves that impact the shoreline of Palm Beach-Azur.

In contrast, summer winds are generally lighter from the northeast or east. This seasonal wind variation creates distinct wave patterns, with higher and more intense waves during winter, significantly affecting coastal dynamics and sediment transport. These wave conditions make Palm Beach-Azur a viable site for wave energy production, which could harness these seasonal wave patterns for sustainable energy production (Algeria - Summary | Climate Change Knowledge Portal, n.d.).

Coastal Currents and Sediment Transport

Wind patterns, water temperature, and the coastline shape influence coastal currents along the Mediterranean Algerian coast. Currents in the Palm Beach-Azur area can be divided into:

- Irregular Currents: Driven by variable wind conditions, these currents fluctuate in speed, direction, and intensity, especially during storm events in the winter months. They contribute to periodic changes in coastal sediment distribution and play a role in beach erosion and sediment transport along the shore.

- Regular Currents: These are influenced by the Coriolis effect, differences in water temperature, and salinity gradients. Regular currents are more stable and follow predictable paths along the coast, promoting a consistent pattern of sediment transport and distribution. However, localized factors such as coastal topography and variations in water depth can create unique current patterns that impact the coastal morphology of Palm Beach-Azur.

Algiers Port Region and Coastal Development

Located near Algiers, Palm Beach-Azur is part of a region with a growing interest in renewable energy and coastal management solutions. The Algerian coastline, including this region, experiences significant wave action that impacts coastal infrastructure and natural habitats.

WECs offer the dual benefits of renewable energy generation and coastal management. In the wave-exposed Palm Beach–Azur area, they hold promise for both sustainable energy production and shoreline stabilization (Algeria - Summary | Climate Change Knowledge Portal, n.d.).

CHAPITRE 2

EXPERIMENTAL ANALYSIS OF MULTI-HORIZONTAL SUBMERGED JETS ENERGY DISSIPATER

M. Moradi [a], M. Sajjadi [b], R. Balachandar [c], A. Arman [d] and A. Ilinca [e]

[a, e] Department of Mathematics, Computer Science and Engineering,
Université Du Québec À Rimouski, 300 All. des Ursulines,
Rimouski, Quebec, Canada, G5L 3A1
[b] Department of Water Science and Engineering,
Chmaran University of Ahvaz, Ahvaz 6135783151, Iran
[c] Department of Civil and Environmental Engineering,
University of Windsor, Windsor, Ontario, Canada, N9B 3P4
[d] Department of Water Engineering, Razi University, Kermanshah 6715685438, Iran

Paper published in the *ISH Journal OF Hydraulic Engineering* [1], February 2021

Abstract

The use of a stilling basin with multiple horizontal submerged jets emerging from two layers has been suggested for use as an energy dissipation structure in hydropower stations. In this study, laboratory velocity measurement is performed to analyze the three-dimensional flow structure of submerged jets and to evaluate the effect of the downstream submergence on the flow field. The results indicate that Reynolds shear stress and vorticity magnitudes increase with increasing jet submergence. Further, it was found that submergence increase leads to a decrease of 2.2% in maximum bed (floor) shear stress and 7.2% in sidewalls shear stress. The Reynolds shear stress quadrant decomposition is also performed for all (H = 0) and high magnitude (H = 2) bursting events, which indicate that the turbulence events of outward and inward interactions made dominant contributions to the total Reynolds stress. Turbulent kinetic energy is also analyzed to obtain a better characterization of the flow field.

Keywords: Flow structure; 3D velocity measurement; hydraulic jump; multi-horizontal submerged jets

---

[1] Moradi, M., Sajjadi, M., Balachandar, R., Arman, A. and Ilinca, A., 2021. Experimental analysis of multi-horizontal submerged jets energy dissipater. ISH Journal of Hydraulic Engineering, 28(3), pp.281-291.

2.1 Introduction

Forced hydraulic jumps formed in stilling basins below hydraulic structures are used to dissipate the surplus energy of supercritical flows and to promote air entrainment. Several studies have been conducted on hydraulic jumps to evaluate the air-water flow characteristics and the energy dissipation rate (Rajaratnam 1962; Chanson et al., 2003; Chanson 2013; Witt et al., 2015; Jesudhas et al., 2018). Recent studies have also revealed the intricate relationship between turbulence and air entrainment in hydraulic jumps (Murzyn & Chanson, 2009; Chachereau & Chanson, 2011; Zhang et al., 2013; Wang & Chanson, 2015; Jesudhas et al., 2020). A considerable number of experimental studies have been carried out to understand the influence of turbulent jets on energy dissipation and the hydraulic jump flow structure (Rajaratnam 1965; Rajaratnam 1976; Qingchao & Drewes, 1994; Liu et al., 2004; Castillo et al., 2012).

Turbulence generation, air entrainment, and consequently energy dissipation are of importance in hydraulic engineering. In certain types of modern energy dissipaters, water jets are employed (Chanson 2015). A common example is the ski-jump stilling basin which is used in hydroelectric power stations with high water head and large flow discharge. In certain scenarios, the bed velocity in this type of stilling basin can exceed 40 m/s (Zhang et al., 2014). To avoid this, a stilling basin with multiple horizontal submerged jets (MHSJ) has been suggested (Deng et al., 2008; (J. G. Chen et al., 2010)). The supercritical jets penetrate the tail-water and dissipate energy via the formation of a submerged hydraulic jump. It not only has a lower bed velocity and smaller negative pressure close to the bed but also has a developed flow pattern with a high energy dissipation rate. Furthermore, the use of multiple horizontal submerged jets disperses a very small amount of water in the air, unlike a ski-jump stilling basin (Ervine and Falvey 1987).

Deng et al., 2008, performed an experimental study to evaluate the characteristics of a stilling basin with multiple horizontal jets and analyzed the flow pattern by combining experimental and numerical data. o and Zhang 2010, studied the scale-effects in the two-phase flow of air-

water in a multiple horizontal submerged jet (henceforth referred to as MHSJ) stilling basin. This study revealed that the scale-effects are minimal on the time-averaged flow characteristics. Chen et al. 2013a were able to determine the velocity distribution of the flow and examine the effect of the jet's distance from the stilling basin floor. Also, they showed that the flow structure downstream of the model is a combination of a classical jet and a hydraulic jump. Chen et al., 2013b used a PIV method to characterize the velocity and vorticity structure of submerged hydraulic jump in the MHSJ stilling basin. The results showed a 60% decrease in the bed velocity compared with the outlet jet velocity. It was also concluded that vertical vortices would be formed at the slab of the stilling basin without reaching it, and horizontal vortices solely affect the endpoint of the vertical vortices.

Some previous studies have shown that a RANS-based standard k-ε model is useful for detecting vortex distribution and energy dissipation; however, the model cannot accurately simulate the flow features (WANG et al., 2009; Wu & Ai, 2010; Zhang et al., 2011; Bayón et al., 2019). The RNG k-ε turbulence model was proposed for accurately capturing the vortices. It has been shown that the vortices have little effect on the stability of side walls and the stilling basin floor (Zhang et al., 2014). Several numerical studies have been conducted to study the velocity distribution in the MHSJ stilling basin. The studies showed that there is no vertical destructive vortex structure in the stilling basin, the present vortices are separated from the stilling basin floor and do not remain static (Deng et al., 2008; Zhang et al., 2014).

Zhang et al., 2017 have presented the methodology to estimate the correlation between the discharge of the submerged jets and near-field vibrations. In another investigation, a mathematical model based on vortex sound theory and turbulent model has been developed by (Lian et al., 2016), who found a high correlation of vorticity fluctuation in strong shear layers and on-site low-frequency noise. Given the importance of flood discharge energy dissipation in water distribution systems and the lack of experimental studies on the performance of the MHSJ energy dissipater, further evaluation of this type of energy dissipater is required. Moreover, most of the studies conducted were on the stability of the stilling basin, the feasibility of its application and the geometrical dimensions of jets (Deng et al., 2008;

Chen et al., 2013a), while the 3D flow structure and internal turbulence nature of the developed zone of the submerged hydraulic jump in MHSJ stilling basin need to be resolved. Thus, the objectives of the present study include:

- To provide an experimental evaluation of the effect of jet submergence on the roller region and its shear layer zone.
- Investigating distributions of time-averaged velocity, sidewalls and bed shear stress, and vorticity distribution at three levels of submergence.
- Evaluation of the effect of jet submergence on the turbulent characteristics and quadrant decomposition of Reynolds shear stress.
- Analysis of the contribution of fluctuating components of velocity to the total energy and the flux of turbulent kinetic energy.

2.2 Experimental Setup

The experiments were conducted in the Hydraulics Laboratory of the Department of Hydraulic Structures at the Shahid Chamran University of Ahvaz, Ahvaz, Iran. The rectangular flume used in this study was 10 m long, 0.8 m wide, and 0.8 m high with a bed slope of 0.005 in the flow direction. The flume sidewall is made of 10 mm thick glass. The flow discharge was measured using an ultrasonic (Easy-Flow) digital flow meter and controlled by a calibrated rectangular weir at the downstream end of the system. The flow discharge of 0.150 m^3/s was held constant, while the water level of the head tank was varied from 1.1 to 1.25 m. The water head of the tank was controlled by a piezometer located at the bottom. A gate was installed at the downstream end of the flume to regulate the submergence and tail-water depth. Figure 2.1 shows the plan and profile of the experimental setup, its accessories, and a detailed scheme of the model and its dimensions. The jet slots are located as shown in Figure 2.1. The three-dimensional components of the velocity were measured using an electromagnet flow meter (ACM3-RS model). As suggested by Dugué et al., 2015, to reduce the effect of air entrainment

and bubble existence on the velocity data measurement, the data recording started from a distance of 200 mm from the jet inlet. The accuracy of the measurement is ±2% or 5 mm/s. A moving carriage with a positioning accuracy of 0.1 mm in the Z direction and 1 mm in the X and Y directions was designed to position the velocity meter. The velocity data were recorded for 4500 points at three submergence levels, while the frequency of the instrument was set at 34 Hz. The flow field of the stilling basin was squarely meshed with a size of 40 mm in the streamwise (Y-Z) cross-section (see Figure 2.2).

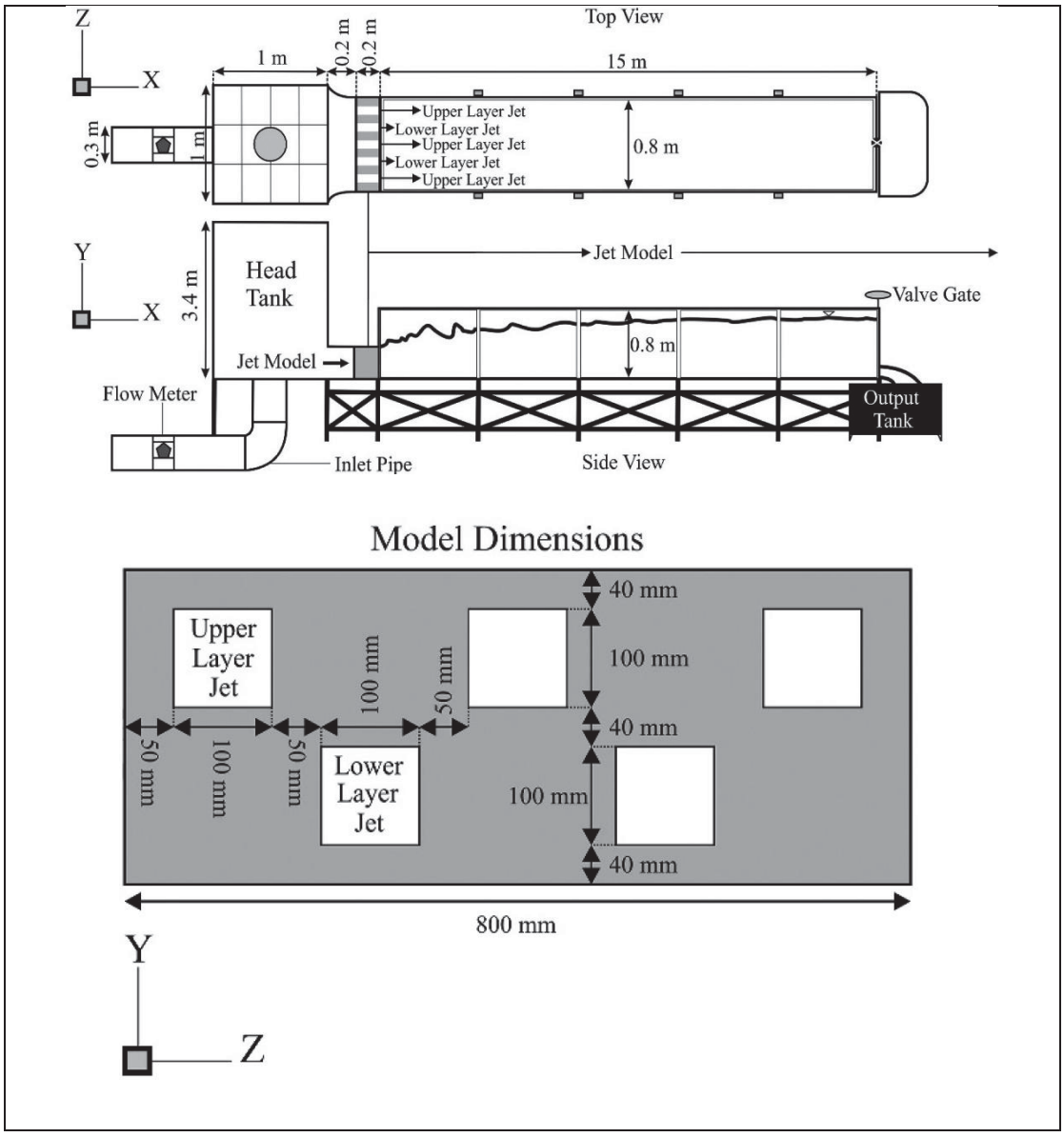

Figure 2.1 Plan and longitudinal view of the experimental setup and layout of staggered jet holes in the MHSJ model

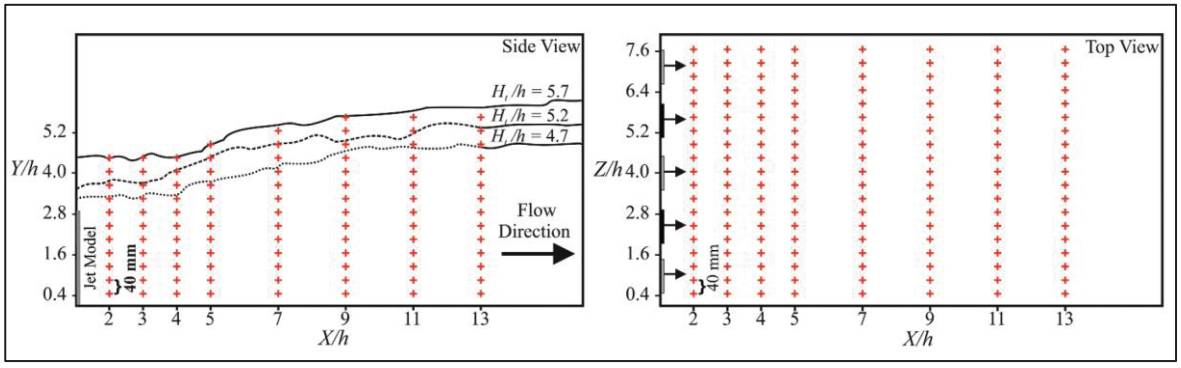

Figure 2.2 Velocity measurement locations

Prior to processing the velocity data, they were filtered to omit the outliers. The frequency model was used for filtering the velocity data. Using the lowpass Butterworth filter technique, the signals were broken down into base signals, and then high-frequency noises were filtered out to achieve accurate signals. Three submergence depths were investigated in this study (i.e., $H_t/h = 4.7$, 5.2, and 5.7). Here, H_t is the tail-water depth, and h is the width of the jet holes (100 mm). Using this dimensionless value, the general conclusions derived from this investigation can be extrapolated to other ratios of submergence level and jet width.

2.3 Discussion and results

2.3.1 General flow pattern

The general flow features and roller structure are presented using time-averaged flow streamlines (Figure 2.3). Superimposed in these plots are the distribution of streamwise velocity where U_x and U_j are streamwise and jet velocity respectively. These longitudinal profiles are shown in Figure 2.3 for the three submergence levels and four vertical planes in the Z direction, in front of the upper (Z/h = 1.2 and 4) and lower (Z/h = 2 and 5.2) layer jets. The circulatory flow which forms frequently in the stilling basin, initiates from the point where the streamwise velocity equals zero. It can be concluded that by increasing the tail-water depth,

apart from lowering the atomization and vibration of structure Zhang et al., 2017, the flow pattern will be much more developed with larger vertical rollers.

Thus, it can also be said that higher submergence requires a longer basin slab due to the developed roller region in the flow direction. The experimental observations are also tabulated in

Table 2.1, in which the dimension and core location of the rollers are presented. This illustrates that in the upper layer jet profiles, the core location of rollers is farther from the structure, while in lower layer jets, it is closer to the structure, resulting in a more extensive roller region and a higher amount of eddy-flow in the section of the upper layer jets. As suggested from

Table 2.1 and Figure 2.3, the values of roller length and core location, in front of upper, and lower layer jets are more similar in the highest submergence level ($H_t/h = 5.7$), compared with the lowest one ($H_t/h = 4.7$). This suggests that the appeared roller in the higher submergences mainly preserves its features and geometry in the width of the channel, while in the lower submergences it is more reliant on the jet arrangement.

In Figure 2.3, with an increase in tailwater, the negative velocity region (blue colour, outer roller region) significantly increases. The overall influence of an increase in submergence on the velocity distribution of the upper layer jets was to decentralize the zone of very high velocity and spread it over a larger area. The right and left end upper layer jets are adjacent to stilling basin side-walls. Therefore, this decentralization of high-velocity zones derived from tailwater increase leads to the lower amount of side-wall shear stress, since the shear stress has a direct relationship with the velocity. To some extent, at lower submergence, the high-velocity zones with high side-wall shear stress are more confined which could be destructive (see Figure 2.4a, to be discussed in the following section).

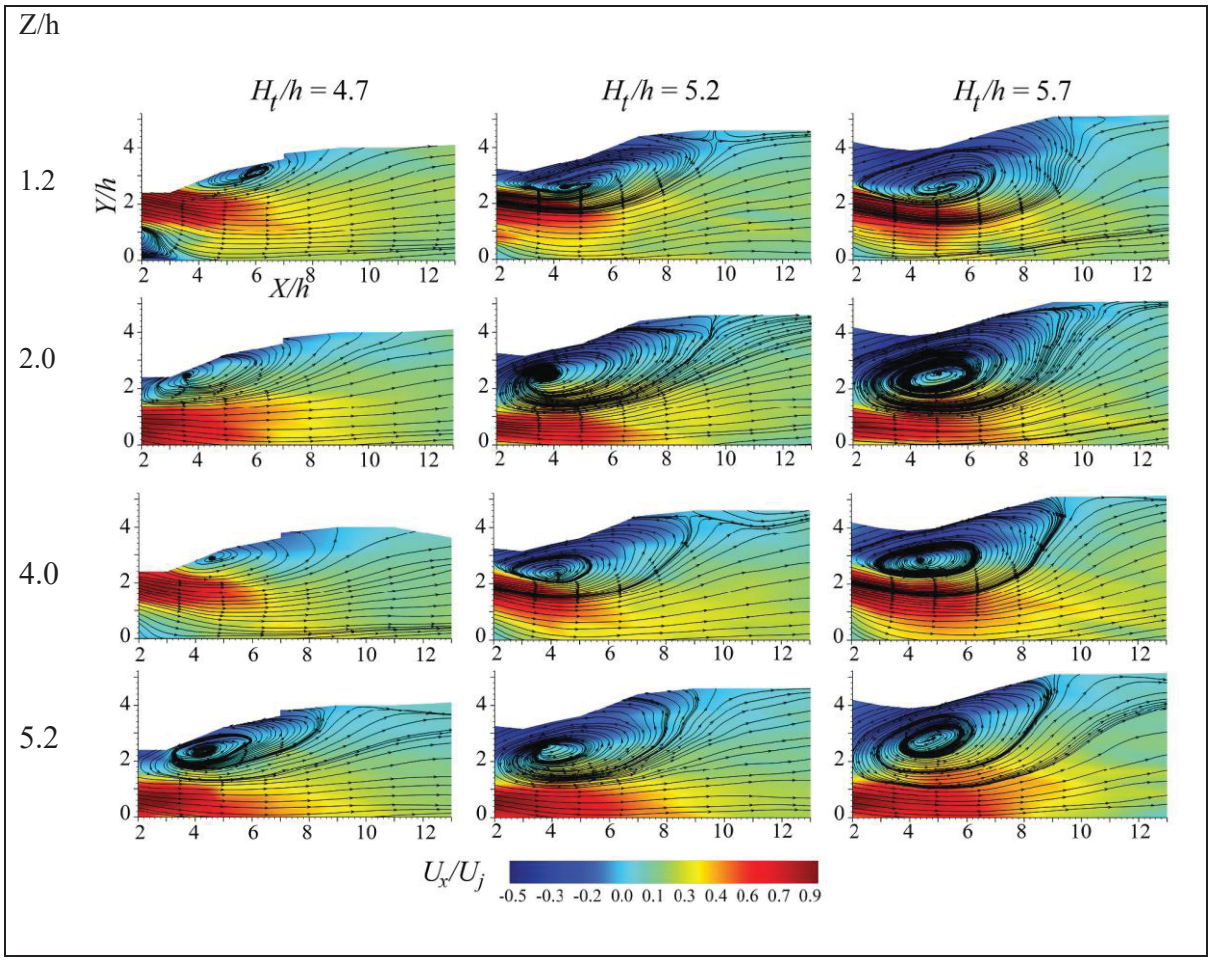

Figure 2.3 Mean flow characteristics in various vertical planes for upper (Z/h = 1.2 and 4) and lower (Z/h = 2 and 5.2) layer jets at three submergence levels

Table 2.1 Dimensions and core locations of roller zones appeared

Roller profile(*X*-*Y*)	$H_t/h = 4.7$		$H_t/h = 5.2$		$H_t/h = 5.7$	
	Roller core location	Roller range	Roller core location	Roller range	Roller core location	Roller range
Z/h = 1.2 (Upper Layer Jets)	X/h = 6.05 Y/h = 3.10	X_r = 1.30 Y_r = 0.40	X/h = 4.39 Y/h = 2.59	X_r = 7.58 Y_r = 1.98	X/h = 5. 26 Y/h = 2.63	X_r = 7.40 Y_r = 2.84
Z/h = 2 (Lower Layer Jets)	X/h = 4.18 Y/h = 2.59	X_r = 5.80 Y_r = 1.30	X/h = 3.64 Y/h = 2.39	X_r = 7.45 Y_r = 2.43	X/h = 5.00 Y/h = 2.54	X_r = 8.40 Y_r = 3.00
Z/h = 4 (Upper Layer Jets)	X/h = 4.60 Y/h = 2.90	X_r = 1.60 Y_r = 0.41	X/h = 4.22 Y/h = 2.38	X_r = 6.78 Y_r = 2.17	X/h = 4.42 Y/h = 2.83	X_r = 7.40 Y_r = 2.63
Z/h = 5.2 (Lower Layer Jets)	X/h = 4.32 Y/h = 2.35	X_r = 5.51 Y_r = 1.38	X/h = 3.72 Y/h = 2.52	X_r = 7.24 Y_r = 2.30	X/h = 4.84 Y/h = 2.82	X_r = 6.96 Y_r = 2.56

2.3.2 Sidewalls and bed shear stress

Shear stress is a variable that technically influences the erosion probability of hydraulic structures. Here, the distribution of streamwise shear stress is presented for the inner and outer side walls of the channel for the same three submergence levels (see Figure 2.4a). The applied shear stress relation is ($\tau_x = \frac{\rho g}{C^2} u\sqrt{u^2 + v^2}$), where ρ is water density, g is the acceleration of gravity, C is the Chezy coefficient, and u and v are time-averaged streamwise and vertical components of velocity. Moreover, shear stress values were divided into $\tau_0=\gamma RS$, where τ_0 is the total bed shear stress, γ is the specific gravity of water, R is the hydraulic radius, and S is the bed slope. The total percentage of regions with a shear stress value of $\tau_x/\tau_0 \geq 7$, at inner and outer sidewalls for each of H_t /h = 4.7, 5.2 and 5.7 submergences are 18.43%, 11.49% and 11.28% respectively. This results in a reduction of 7.15% in side-wall shear stress at higher submergences. This shows that higher amounts of tail-water have less confined wall shear stress and less probability of side-wall erosion. In addition to the side-wall shear stress caused by upper layer jets, the shear stress due to the secondary flow (τ_z) also exists which is small. Generally, stilling basin sidewalls are not in danger of severe erosion by means of jet flows as shown by Zhang et al., 2014.

The bed (floor) shear stress distribution is shown in Figure 2.4a. As observed from the analysis of bed shear stress at the cross-section Y/h = 0.4, the area of dispersion regions with $\tau_x/\tau_0 \geq 14$, for H_t/h = 4.7, 5.2 and 5.7 submergences were 11.2%, 15.68% and 16.99% respectively. However, in Figure 2.4b the area of maximum shear stress (absolute red, $\tau_x/\tau_0 \geq 22$) seems equal in all three plots, there is a 2.2% decrease for the highest submergence level. The percentage of maximum bed shear stress ($\tau_x/\tau_0 \geq 55$) of H_t/h = 4.7, 5.2 and 5.7 submergence levels, was 4.83%, 3.28% and 2.63% respectively. The plots show that at higher submergences, the jets tend to impact the stilling basin floor over a larger area but with a lower shear stress value.

(a)

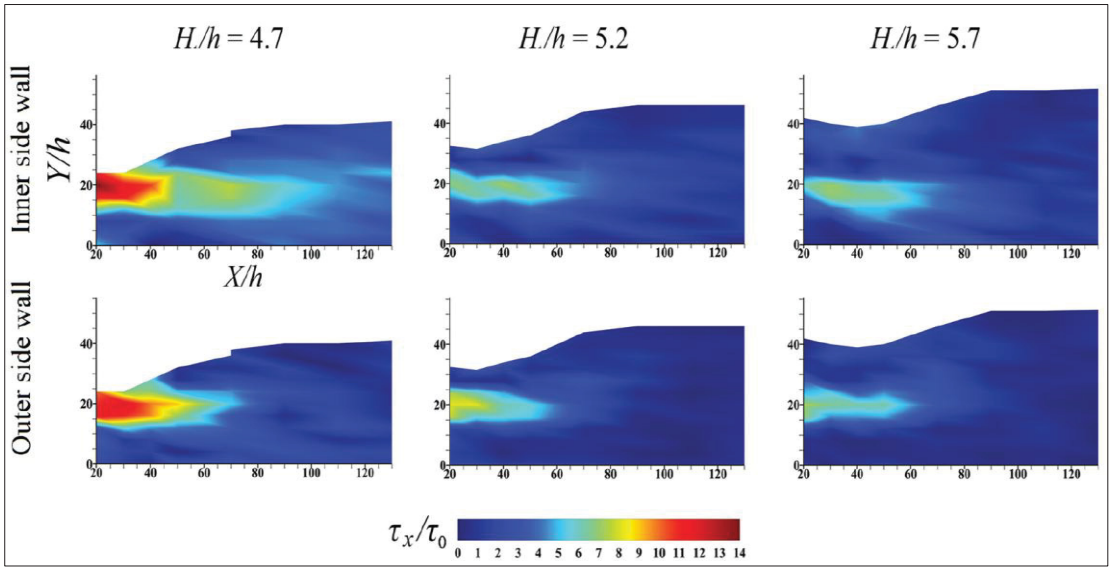

(b)

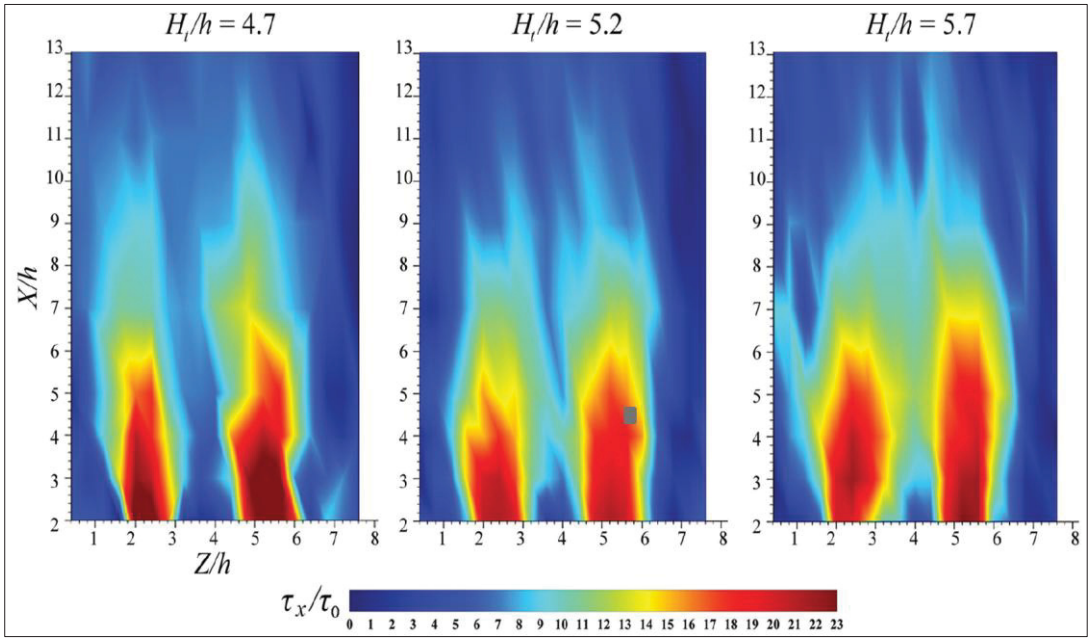

Figure 2.4 Distribution of (a) side-wall and (b) bed (floor) shear stress at Y/h = 0.4

2.3.3 3D nature of the flow field

Horizontal (X-Z) and streamwise (Y-Z) planes of streamwise velocity distribution are arranged for $H_t/h = 5.7$ in Figure 2.5a and Figure 2.5b, respectively. The penetration length of inlet jets and the roller structure are easy to track here. It is clearly shown in Figure 2.5a that the velocity of the upper, and lower layer jets decay gradually along the streamwise direction, similar to that noticed in a classical hydraulic jump (Jesudhas et al. 2018). Figure 2.5b shows that the high-velocity individual jets are merged and evolved into a single slow-flowing jet farther from the jet origin (X = 0.65 m). This velocity reduction is representative of energy dissipation and significant shear stress between the flow layers immediately downstream of the orifices along a fully turbulent zone.

Moreover, it can also be seen that lower layer wall-jets travel a farther distance (about 7.8%) in the streamwise direction compared with the upper layer jets. This can be attributed to the interaction and the strong shear region between the upper layer jets and the roller which is depicted in Figure 2.5c. The vector field, superimposed with contours of streamwise velocity, is shown in Figure 2.5c. The zones of shear stress between upper layer jets and the roller could be clearly seen. This difference in the velocity distribution of upper, and lower layer jets might also be due to the strong interaction between upper, and lower layer jets themselves, as also observed by Chen et al. 2013a.

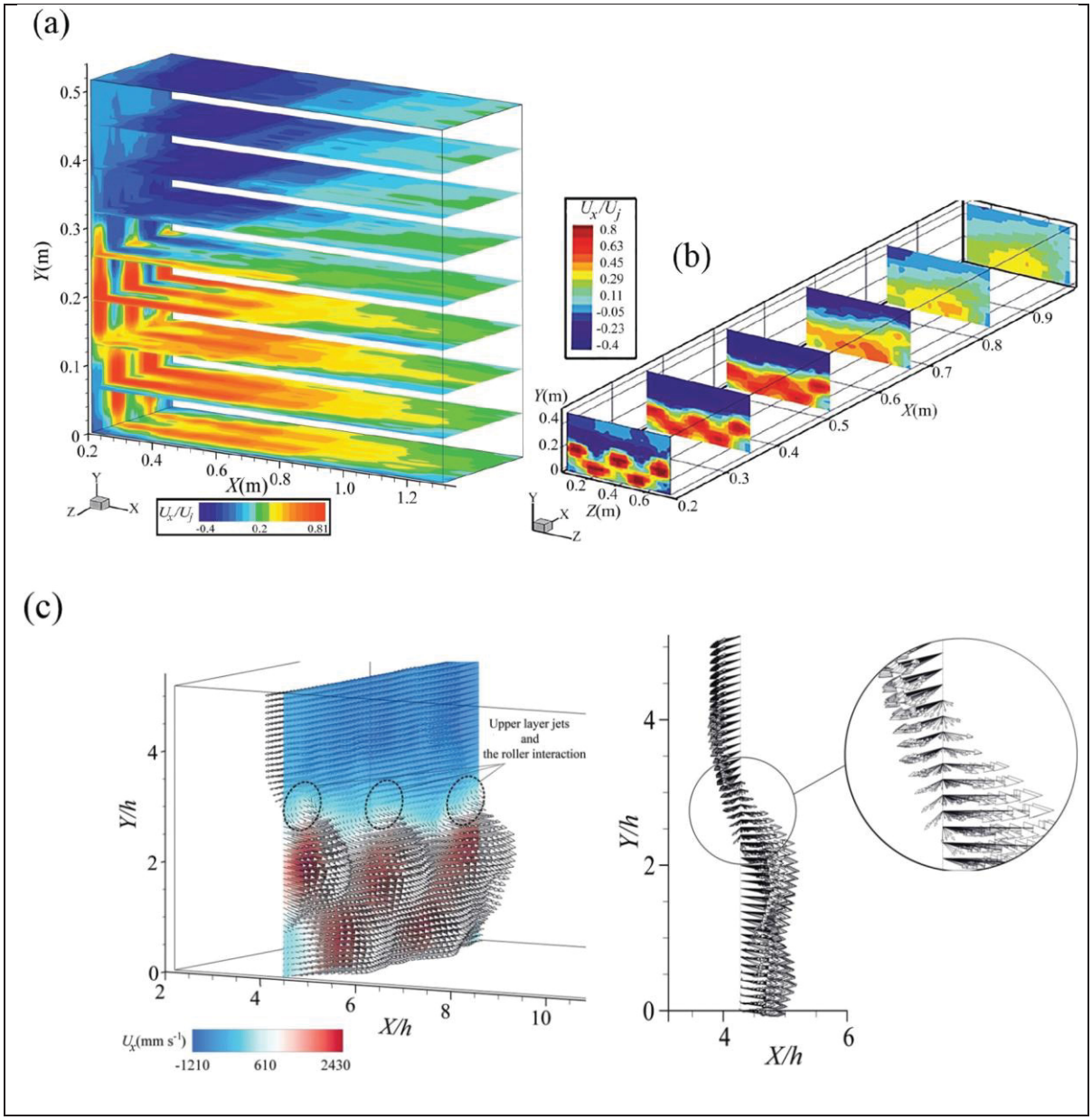

Figure 2.5 Streamwise velocity contours in (a) X-Z planes, (b) Y-Z planes, and (c) interaction of upper layer jets and the roller

2.3.4 Reynolds shear stress and vorticity distribution

Figure 2.6a depicts the normalized shear stress ($\overline{u'v'}/U_j^2$) distribution (u′ and v′ are streamwise and vertical instantaneous fluctuating components of velocity and U_j is jet velocity) superimposed with the velocity vectors in vertical planes (Z/ h = 2.4 and 4). The size of arrows

represents the velocity magnitude, so that the upper and lower wall-jets are distinctive in all plots. The figures show roller zones with strong positive Reynolds shear stress in all planes and submergence levels. These zones contain a high energy dissipation rate and accordingly high turbulent kinetic energy production due to the interaction between the wall-jets and the inner layer of the roller. This interaction produces maximum shear stress in the inflection point, the point where the flow transitions from the wall-jet flow to the roller flow (Jesudhas et al. 2018). It is inferred from Figure 2.6a that in higher submergences, the zone of Reynolds shear stress is stronger and more extended in vertical and horizontal directions for both upper, and lower layer jets suggesting that the roller region is more developed in higher submergences (see Figure 2.3).

In Figure 2.6b the vorticity distribution superimposed with the mean velocity vectors in the vicinity of submerged wall-jets and in vertical planes of lower (Z/ h = 2.4) and upper (Z/h = 4) layer jets. The vorticity values were calculated using the equation below, where ω is vorticity magnitude:

$$\vec{\omega} = \nabla \times \vec{V} = \left(\frac{\partial}{\partial x}, \frac{\partial}{\partial y}, \frac{\partial}{\partial z}\right) \times (u, v, w) = \left(\frac{\partial w}{\partial y} - \frac{\partial v}{\partial z}, \frac{\partial u}{\partial z} - \frac{\partial w}{\partial x}, \frac{\partial v}{\partial x} - \frac{\partial u}{\partial y}\right) \quad (2.1)$$

$$\vec{\omega} = (\omega_x, \omega_y, \omega_z)$$

$$\omega = \sqrt{\omega_x^2, \omega_y^2, \omega_z^2}$$

It is obvious from Figure 2.6b that due to the roller flow, vorticity values are higher in front of upper layer jets compared with lower layer jets, hence, the maximum vorticity takes place in upper layer jets, where high-velocity wall-jets interact with the roller ($2 < X/h < 4$ and $2 < Y/h < 3$). The shear stress and vorticity distributions in lower layer jets were generally similar to those of upper layer jets, however, the vorticity values were weaker and maximum shear stress regions were stronger and closer to the basin floor in the lower layer jets.

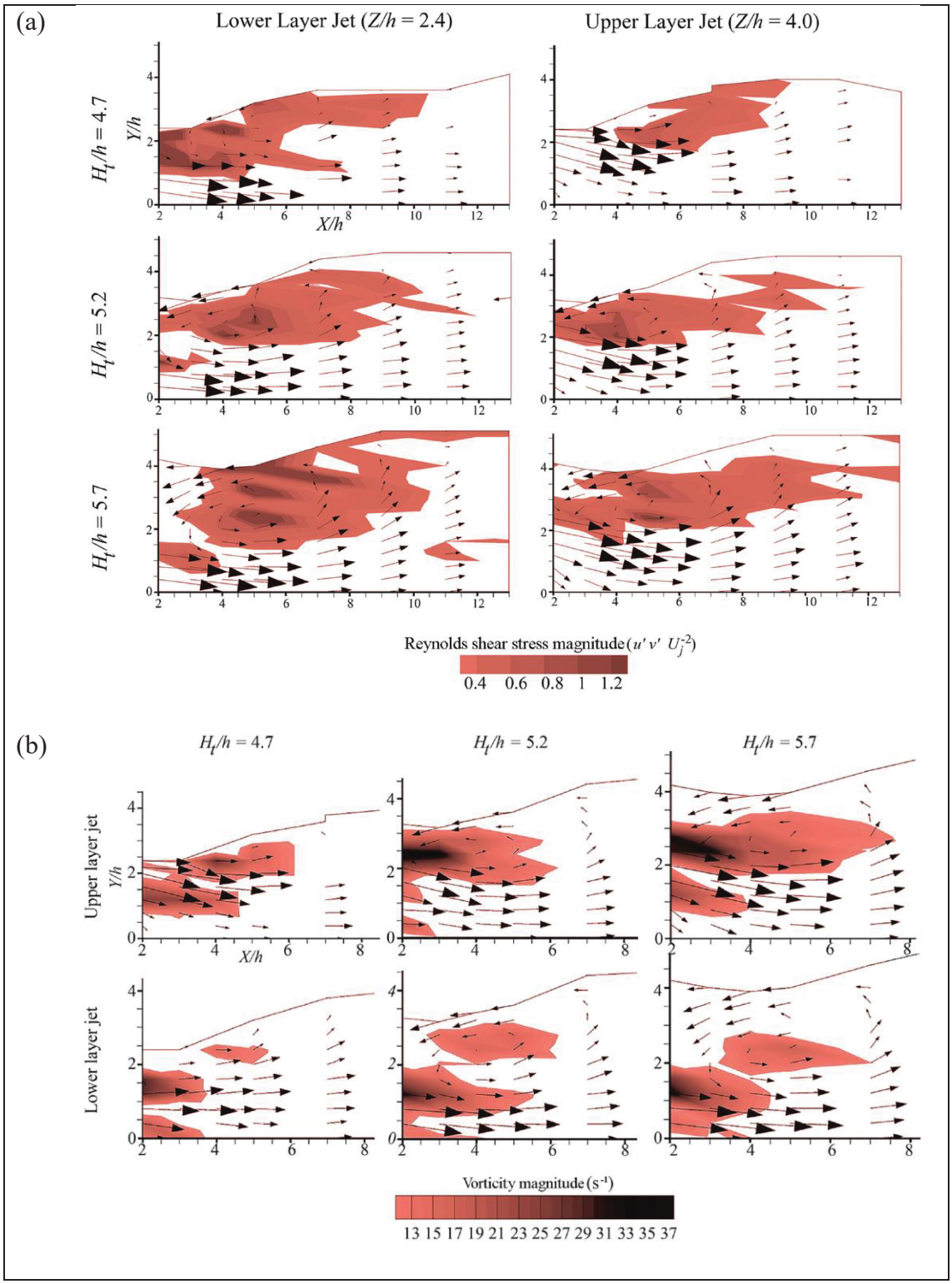

Figure 2.6 Velocity vectors with distributions of (a) Reynolds shear stress magnitude and (b) mean vorticity magnitude

2.3.5 Quadrant analysis

In this paper the contribution of turbulence events of the flow is specified by conditional decomposition of u′ and v′ into four (i = 1 to 4) quadrants. The turbulence events are defined as Q_1(+u′, +v′), Q_2(−u′, +v′), Q_3(-u′, −v′), and Q_4 (+u′, −v′), namely outward interaction, ejection, inward interaction and sweep, respectively. (Wallace et al., 1972), investigated the contribution of different turbulence events in the total Reynolds shear stress ($-\overline{u'v'}$) by defining a detection function I(t):

$$I(t) = \begin{cases} 1 & \text{if } \left|u'v'\right| \geq H\, u'_{rms} v'_{rms} \\ 0 & \text{otherwise} \end{cases} \tag{2.2}$$

Here H is the hyperbolic hole size and determines the hole border ($H = |uv|/u^{v}_{rms}\,rms$). By increasing H, the contribution of each quadrant (number of points outside of the hole) in total turbulence reduces and only extreme (intense) events remain. The contribution of the ith quadrant to $-\overline{u'v'}$ is:

$$< u'\, v' >_{Q_{i.H}} = \lim_{t\to\infty} \frac{1}{T} \int_0^T u'(t)v'(t)I(t)dt \tag{2.3}$$

Finally, the contribution of each quadrant in total Reynolds shear stress, which are outside of the hole normalized with ($\overline{u'v'}$) and computed as:

$$S^{f}_{Qi.H} = < u'\, v' >_{Q_{i.H}} / \overline{u'v'} \tag{2.4}$$

The quadrant decomposition of u′ and v′ in the central plane of the channel in two vertical locations of Y/h = 2 (upper layer wall-jets) and Y/h = 3.2 (the roller region) for the same three submergence levels is shown in Figure 2.7. In the region of the wall-jets (Y/h = 2), Q_1 and Q_3 are dominant events representing outward and inward interaction turbulence events in this region for all three submergence levels. In the shear layer zone of the roller (Y/h = 3.2), all the turbulence events co-exist, but in general the Q_1 event was stronger with a higher probability of occurrence.

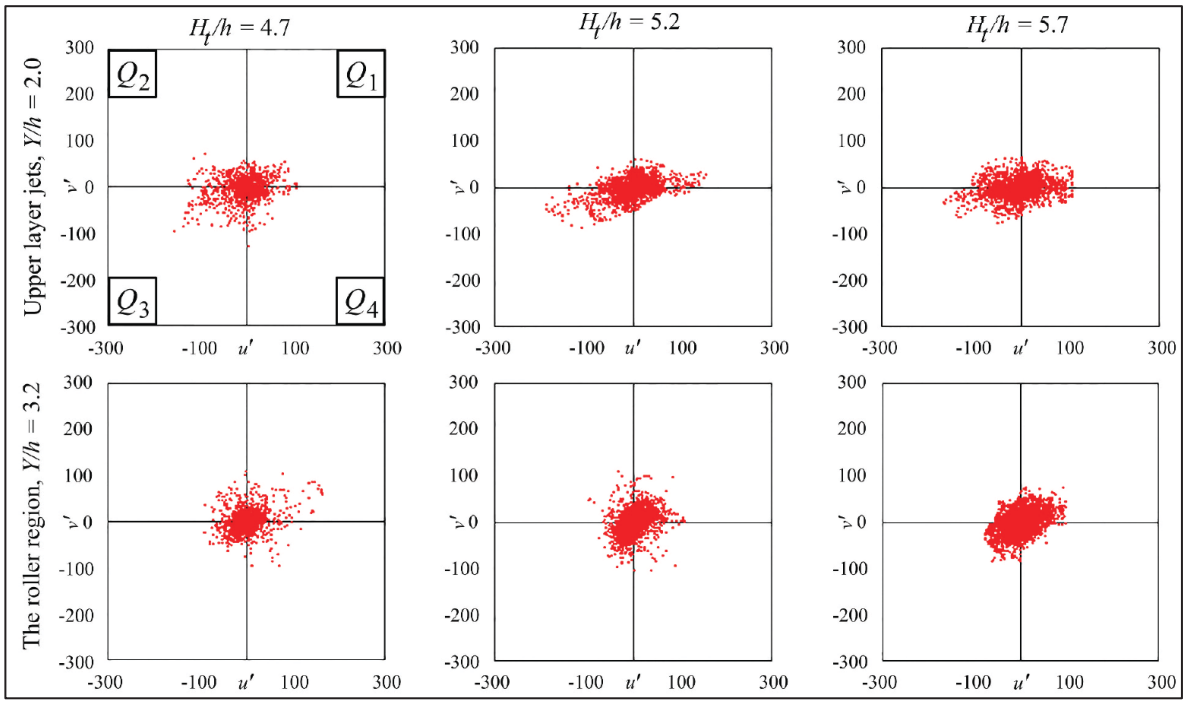

Figure 2.7 Quadrant distribution of fluctuating components of velocity in the central plane of the channel (Z/h = 4)

2.3.6 Quadrant Reynolds shear fractions

The contribution of the different turbulence events to the total Reynolds shear stress is determined for two hole sizes (H = 0 and H = 2). Where, H = 2 represents the stronger events. Figure 2.8 shows the effect of submergence level on the quadrant shear fractions, which suggests a better understanding of the relationship between turbulence events and the flow structure. This analysis was performed for vertical planes in the upper (Z/h = 1.2 and 4) and lower (Z/h = 2.4 and 5.6) layer jets. Also, to minimize the effect of air entrainment on the data quality, the streamwise location of X/h = 5 was selected with a distance of 500 mm distance from the jet origin.

From Figure 2.8, it could be inferred that with submergence rise, the contribution of the roller zone (2.5 < Y/h < 4) in the total shear decreases and most of the Reynolds shear stress are attributed to the zone of the upper (1.8 < Y/ h < 2.8) and lower (0.4 < Y/h < 1.4) layer jets, this

could be an interesting result which manifests lower surface fluctuations along with the formation of developed rollers in higher submergences which was observed in the Reynolds shear stress distribution and circulatory flow plots as well. The shear stress quadrant contribution for bigger hole sizes (H = 2) was approximately the same as H = 0, however, in H = 2 the turbulence variables are filtered and only the intense events appeared. Generally, the higher dominance of inward and outward interactions was observed in the total Reynolds shear stress quantities, especially in the zones of wall-jets and the roller.

The dominance of outward and inward interaction turbulence events is attributed to the high rate of energy dissipation in the zone of interaction of output jets and the roller. Although there are other turbulence events at shear zones, they are not extreme and they disappear in the figures of strong events (H = 2).

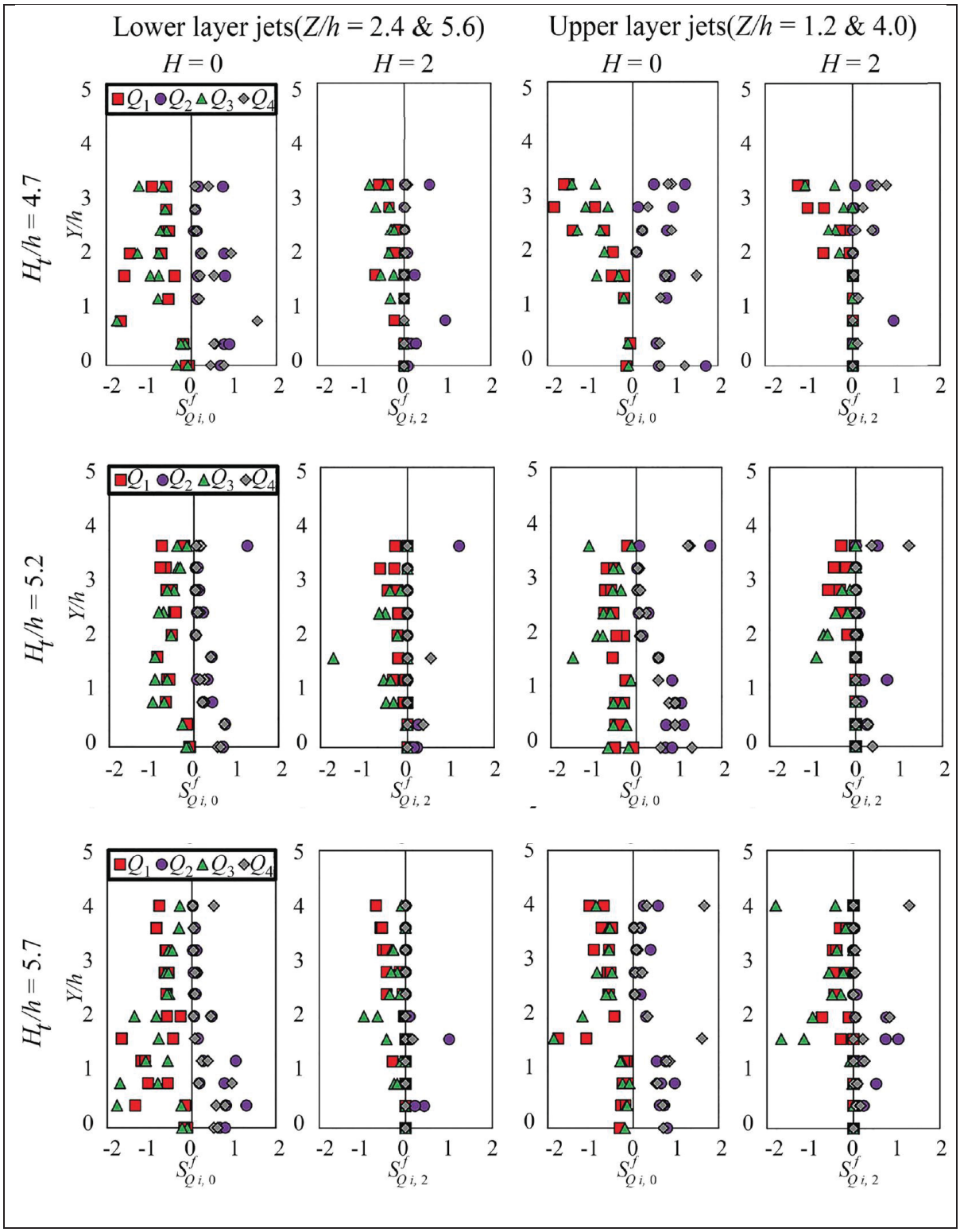

Figure 2.8 Contribution of different quadrants to the total Reynolds shear stress (locations of profiles are shown on top of subplots)

2.3.7 Spatial patterns of time-averaged turbulence characteristics and flux of turbulent kinetic energy

To achieve a better understanding of the turbulence intensity in X, Y and Z directions, the spatial contribution of velocity fluctuating components to the total turbulent kinetic energy was investigated in the centerline plane of the hydraulic jump, for the same three submergence levels. As it is shown in Figure 2.9a the streamwise fluctuating component (u′) is dominant in all three submergence levels and all streamwise locations. It also reveals that (u′) produces approximately 50% of the total TKE at all submergence levels. This contribution of streamwise velocity in the total TKE has an upward trend until X/ h = 5 after which it begins to decrease. The contribution of the fluctuating components (v′) and (w′) in y and z directions, respectively to TKE has a slight descending pattern until X/ h = 5. This suggests a redistribution of TKE from the streamwise to the other two directions and could also be attributed to the formation of secondary currents in the channel.

Turbulent kinetic energy originates from the surplus of energy dissipation, this reveals in the vicinity of the bed, side walls and surface and brings about a dynamic conveyance of energy between these regions (Balachandar & Bhuiyan, 2007). The Flux of turbulent kinetic energy is a variable which defines the trend of energy transportation and its direction. The turbulence flux in the centerline of the flume (Z/h = 4) and streamwise direction points (X/h = 3–5) is computed using $F_{ku} = 0.5(u^3 + uv^2 + uw^2)$ and $F_{kv} = 0.5(v^3 + u^2v + vw^2)$ where F_{ku} and F_{kv} are turbulence fluxes in streamwise and vertical directions. Figure 2.9b and Figure 2.9c depict the vertical distribution of turbulent fluxes, normalized with U_j^3 at H_t/h = 5.7 submergence level.

The vertical distribution of F_{ku} and F_{kv} started from low positive values and reached to zero and its negative peak in front of high-velocity wall-jets (Y/h = 2) due to the significance of kinetic energy in this region. As regard to the negative flux values in front of upper layer jets, the dominance of inward interactions could be concluded in this region and the turbulent flux of energy travels upstream and downward in streamwise and vertical directions. The zero values of turbulence flux represent the zone of maximum Reynolds shear stress

(zone of interaction between upper-layer wall-jets and an inner layer of the roller). The maximum positive peak of the values could be observed in the center of the circulatory flow, where the velocity components are approximately zero, outward interaction events with downstream and upward travel of turbulent energy flux are observed in this zone. This has also been observed in the quadrant analysis, and compromises well with the findings of Dey et al., 2010 about the turbulent characteristics of submerged wall-jets.

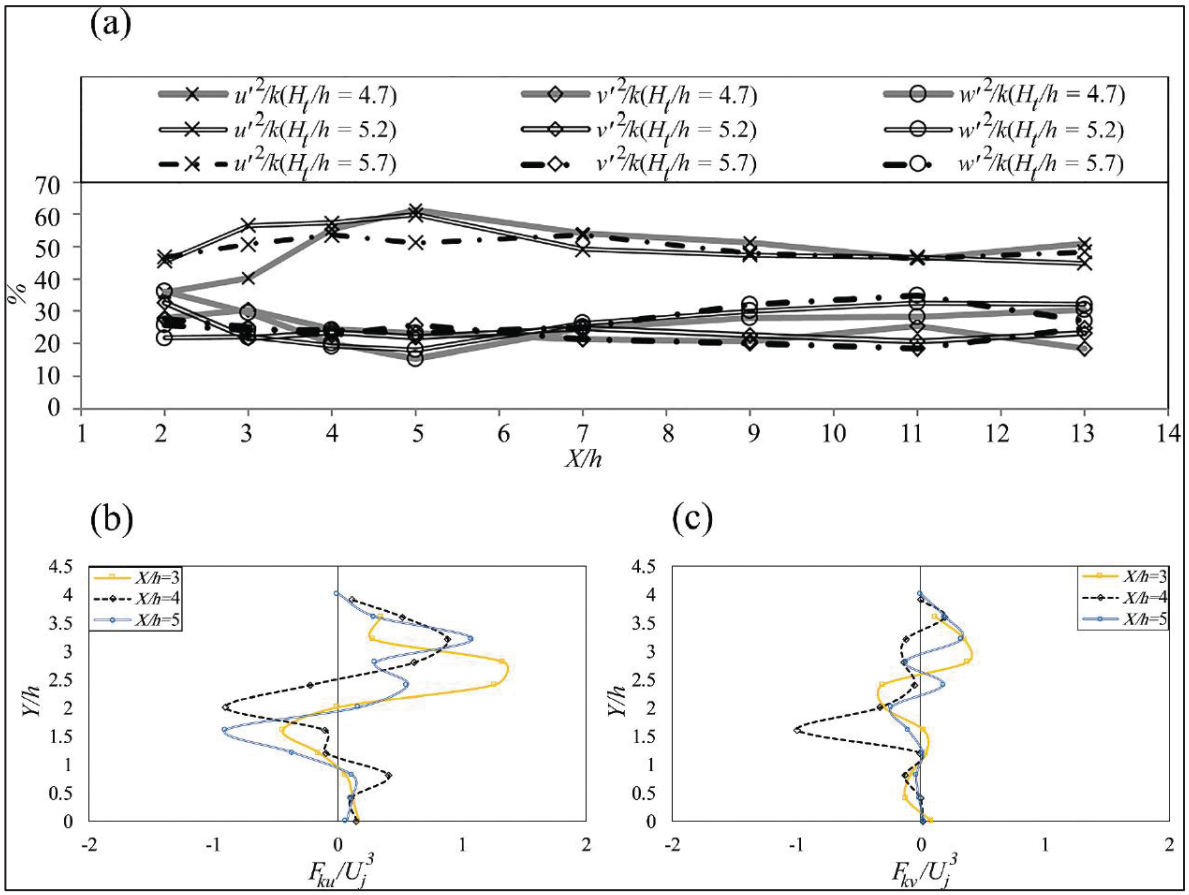

Figure 2.9 Turbulent kinetic energy: (a) average contribution of velocity fluctuation components to turbulent kinetic energy, flux of turbulent kinetic energy in (b) streamwise and (c) vertical directions

2.3.8 Conclusions

In this study, we conducted a comprehensive experimental study on hydrodynamics of the flow, turbulence and Reynolds shear stress quadrant analysis, and vorticity and vortex structure

in the MHSJ stilling basin. Most studies on stilling basin with submerged horizontal jets have dealt with the flow pattern, geometric characteristics of the structure and the distance between the jets and their height from the stilling basin bed. However, this study investigated the impact of downstream submergence amount on the flow features, and the following results were obtained:

- Strong roller structures have been noticed downstream of the jets. It was shown that an increase in submergence results in the formation of more developed and extended roller regions. The core location of these rollers was farther from the jet origin, that is, in front of the upper layer orifices as compared with the lower layer orifices.

- An increase in the submergence level causes a redistribution in the zones with higher velocity. This results in a slight fall in the side-walls shear stress (a decrease of 7.15%) and a decrease of 2.2% in bed shear stress. Thus, the optimal ratio of tail water level to jet width in this study equals 5.7.

- The lower-layer jets penetrate farther into the flow, about 7.8% more compared with the upper layer jets. This can be attributed to the strong interaction and shear layer between upper layer jets and the roller, which dissipates more energy.

- Detailed insight into the turbulence characteristics of the hydraulic jump in MHSJ stilling basins is provided using quadrant analysis of velocity fluctuations and Reynolds shear stress. Outward and inward interactions occur more frequently and are stronger in magnitude, providing the highest contribution in the total Reynolds shear stress.

- The dominant turbulence events are Q_1 and Q_3 which always give negative shear stress and contribute to energy dissipation. This is attributed to the horizontal arrangement and the multiple number of the jets in MHSJ which increase the shear region and consequently energy elimination in this type of stilling basin.

CHAPITRE 3

MODELING OF A WAVE ENERGY CONVERTER IMPACT ON COASTAL EROSION, A CASE STUDY FOR PALM BEACH-AZUR, ALGERIA

M. Moradi [a], N. Chertouk [b] and A. Ilinca [c]

[a, b, c] Wind Energy Research Laboratory (WERL), Université du Québec à Rimouski, 300 All. des Ursulines, Rimouski, Quebec, Canada, G5L 3A1

Paper published in *Sustainability*[2], December 2022

Abstract

Facing the exhaustion of fossil energy and in the context of sustainable development, strong incentives are pushing for the development of renewable energies. Nuclear energy and fossil fuels like petroleum, coal, and natural gas provide most of the energy produced today. As a result, greenhouse gases are released, and climate change becomes irreversible. Furthermore, radioactive waste disposal causes severe radiation pollution in nuclear power. Alternatives such as marine energy are more sustainable and predictable. It has none of the detrimental effects of fossil and nuclear energy and is significant in terms of environmental sustainability by defending the coastline from erosion. Here, we study the Palm Beach-Azur region near Algiers on the Mediterranean Sea. The study aims to use wave energy converters (WEC) to generate clean energy and reduce coastline erosion. The results of this study show that in the presence of wave energy converters, the wave height decreased by 0.3 m, and sediment deposition increased by 0.8 m. Thus, sand deposit predictions demonstrate that the presence of WEC decreases marine erosion and contributes to an accumulation of sediments on the coast. Moreover, this confirms that WECs can serve a dual role of extracting marine energy by converting it into electrical energy and as a defense against marine erosion. Therefore, WECs

---

[2] Moradi, M.; Chertouk, N.; Ilinca, A. Modelling of a Wave Energy Converter Impact on Coastal Erosion, a Case Study for Palm Beach-Azur, Algeria. Sustainability 2022, 14, 16595. https://doi.org/10.3390/su142416595

justify their efficiency both in energy production and economic and environmental profitability due to coastal protection.

Keywords: wave energy converters; erosion; SWAN (Simulating Waves Nearshore) model; wave height; energy dissipation

3.1 Introduction

Among the renewable energies experiencing considerable development, marine energies need more attention. The ocean, which covers 71% of Earth's surface, is an underutilized energy source. The expected increase in the number and intensity of storms due to climate change, flooding along coastal areas, and the push for corporate environmental responsibility along coastal regions are opening the way for significant marine energy development. Wave Energy Converters (WEC) should be climate-proof (resistant to sea level rise and strong waves), environmentally friendly, and of low visual impact (submerged or low crested) to avoid negative impacts. Various WECs have different mechanisms and technologies for converting mechanical energy into electricity. These technologies have been reviewed by many authors (Drew et al., 2016; Falnes, 2007; McCormick, 2007; Thorpe, 1999).

Another vital feature of WECs is their influence on the hydrodynamics near coastlines. Various numerical and experimental studies have been conducted to assess the hydrodynamic impacts of coastal protection structures on nearshore flow characteristics. Atan et al., 2019 have studied three arrays of configurations with 12 WECs on the western coasts of Ireland to measure the influence of these structures on nearshore wave climate and captured power. They found that wave height decreased by less than 1% between 1 km and 3 km from the coast and by 0.1% between 100–300 m from the coast. They also reported that wave power decreased by less than 1% between 1–3 km from the coast and by 0.2% between 100–300 m from the coastline.

Chang et al., 2016 performed a sensitivity analysis of the SWAN model for WEC arrangements and features. They concluded that wave height decreased by 30% and 15% were observed

because of two tested scenarios for wave energy converter structures. Flow regime alterations imposed by a wave farm located on the southwestern coasts of England were investigated using SWAN and ROMS (Regional Ocean Modeling System) models by Greaves & Iglesias, 2017. They studied WECs effects on wave radiation stresses, bed shear stresses, bottom frictions, and sediment movement. The results confirmed that the wave farm influences gradients of bottom shear stress, which leads to adjusting current velocity, and wave heights (by around 5 to 10 cm). It has been reported that flow interactions and bed stress are the main factors affecting sediment transport patterns and subsequent morphological changes. Contardo et al., 2018 validated their proposed SWAN model using measured field data from a series of wave measurement devices. Their model showed that WEC impacts on the wave field and flow structure are more significant at 40 m downstream of the unit, with a maximum drop of 20% of the wave height.

Apart from the impacts of WECs on the flow field and, consequently, the morphology of a region, it is also necessary to examine the region's potential in terms of wave energy. It can be considered as the first step of the project's implementation. Numerous studies have focused on the marine power potential of a region calculated from wave characteristics such as wave height and wave period (Gonçalves et al., 2014; Guillou & Chapalain, 2015; Iglesias & Carballo, 2009b; Mendes et al., 2012). The wave parameters are determined using in situ wave measurements, satellite data, and numerical wave models.

Appendini et al., 2015 investigated the wave potential in the Caribbean Sea. To this end, they validated a 30-year wave hindcast of the region using altimetry (Globwave) and buoy (DIMAR) data. Based on their study, the Caribbean Low-Level Jet with easterly winds of 13 m/s has the highest potential for wave energy extraction with 8 to 14 kW/m. Garcia & Canals, 2015 assessed wave power potential in Puerto Rico and US Virgin Islands. They used a high-resolution wave model to estimate available wave power in the region. They reported 10 to 12 kW/m as the available potential of wave power, which reveals that these sites are theoretically appropriate for wave energy harvest projects.

The extractable wave energy of the Atlantic coast of Morocco was studied by Sierra et al., 2016. Using 44-year data series at 23 points and statistical analysis of significant wave heights, they categorized the domain of study in terms of the amount of recoverable energy. As a result, the central area of the Atlantic Moroccan coast, with the most considerable wave heights, was known as the optimal area for wave energy harvesting. This area had an annual average wave power higher than 25 kW/m.

The WECs use sensors which could pose several problems due to the possibility of simple disturbances causing errors. Future research should consider using interval observers instead of sensors. Based on the recent research Khan et al., 2020, 2021 , interval observers can be used for control of linear and non-linear systems, and anti-disturbance controller design, in a wide range of applications such as Wave Energy Converters. To maximize the benefits of WECs, installing them in regions susceptible to coastal erosion is imperative. Beaches form about 20% of the planet's coastline. Of these, nearly 70% are undergoing a phase of erosion, 20% are stable, and 10% show signs of accumulation.

Moreover, Choupin et al., 2021 investigated the most significant factors affecting wave energy harvesting. As they noted, local geographical specifications such as touristic features are critical in recognizing the suitable location for WEC installation. Algeria has a coastline of 1622 km, which welcomes millions of people. The beaches are a major tourist attraction, providing a primary economic interest and a natural landscape heritage of incomparable value. Since Algeria has a robust tourism industry, and considering its power demand and population density, these inputs justify the installation of WECs near its coasts. Unfortunately, this coastline is marked by degradation due to intensive erosion.

In this study, we focused on the area of Palm Beach-Azur, which constitutes a tourist site for summer visitors. High competition for using this natural environment has led to coastline degradation. Marked by long-term intensive erosion, this study evaluates the shoreline's behavior and the coastline's dynamics following the installation of WECs. In addition, it determines the effect of this equipment on hydrodynamics of flow.

3.2 Materials and Methods

3.2.1 SWAN Mathematical Model

In this study, SWAN has been used to calculate wave height reduction and energy dissipation due to the design of the wave farm. SWAN is a third-generation wave model developed by Booij et al., 1999 that estimates wave characteristics (significant wave height, peak period, average direction, and the spectrum of directional waves) in coastal areas, lakes, and estuaries. The required inputs are wind data, the bathymetry of the region, and flow input information. The model solves the equilibrium equation of the action of the spectral waves without prior assumptions on the shape of the wave spectrum. A two-dimensional wave action density spectrum, N (ω, θ), describes the wave field, where the angular wave frequency is ω, and θ is the direction of the wave. The wave action density spectrum is used instead of the energy density spectrum. The action density is conserved in the presence of currents, but the energy density is not. Therefore, the wave energy spectrum can be calculated from the wave action spectrum. The wave action equilibrium equation is discretized using A time-based method of finite difference, geographic space (x, y), and spectral space (ω, θ). The equilibrium equation of the action of the spectral waves is:

$$\frac{\partial N}{\partial t} + \frac{\partial (c_x N)}{\partial x} + \frac{\partial (c_y N)}{\partial y} + \frac{\partial (c_\omega N)}{\partial \omega} + \frac{\partial (c_\theta N)}{\partial \theta} = \frac{S}{\omega} \tag{3.1}$$

The first term indicates the local change rate in wave action density on the left-hand side of the equation. The second and third terms refer to the action of waves over a geographical space, with their propagation speed and direction, respectively. The fourth term quantifies the relative frequency shift due to variations in depths and currents, with a propagation speed of c_x and c_y in the X and Y directions. Finally, the fifth term represents the refractive effects induced by depth variations or currents, with propagation speed C_θ in the direction θ. The explanations of propagation velocity above stem from linear wave theory.

Considering the right side of the equation, S refers to the source and sink terms in the physical processes that produce, dissipate, or redistribute wave energy:

$$S = S_{nl4} + S_{nl3} + S_{in} + S_{wc} + S_{bot} + S_{brk} \quad (3.2)$$

Here, S_{nl4} presents to the redistribution of energy by nonlinear quadruplet wave-wave interactions, S_{nl3} refers to the redistribution of the nonlinear triad of wave energy, Sin is the transfer of wind energy to waves and the dissipation of wave energy that occurs as a result of white capping, S_{bot} is the term for background friction energy elimination, and S_{brk} is the random wave energy dissipation due to depth-induced fracture.

The wave energy flow, also called wave power, is calculated on its X and Y components with the following two expressions:

$$J_x = \iint_0^{2\pi} \rho g c_x E(\sigma, \theta) d\sigma d\theta \quad (3.3)$$

$$J_y = \iint_0^{2\pi} \rho g c_y E(\sigma, \theta) d\sigma d\theta \quad (3.4)$$

Where E (σ, θ) is the directional spectral density, which specifies how energy is distributed over frequencies (σ) and directions (θ). The magnitude of the wave power is then calculated as follows:

$$J = (J_x^2 + J_y^2)^{\frac{1}{2}} \quad (3.5)$$

SWAN model documentation describes the set of equations governing the spectral distribution of wind waves, the transmission of wave energy, the source and sinks, the effect of the ambient current on the waves, the modelling of obstacles and structures, and the configuration induced by the waves (SWAN User Manual, 2022).

3.2.2 Wave Refraction Calculation

As waves approach the coast, their propagation is influenced by the bathymetry once they reach a certain depth, calculated using the linear theory ($d = \frac{1}{2} L_0$) where d is the water depth

and L_0 is the offshore swell wavelength. This process, known as wave refraction, causes wave ridges to align with the isobaths. Consequently, energy becomes concentrated on headlands and spread out in bays or gulfs. The study of refraction aims to analyze the characteristics of swell, including its direction and height, as it moves from the open sea toward the coastline.

The wave refraction phenomenon is accounted for by calculating the refraction coefficients (K_r) at several points on a coastline for the dominant swell sectors and a given swell period. Thus, we opt to calculate the Shoaling Coefficient K_s.

$$K_s = \frac{H_s \text{ (Certain location)}}{H_s \text{ (Deep water)}} \tag{3.6}$$

The values of Ks calculated up to the coast reflect the following:

- The energy attenuation when $K_s < 1$ (wave divergence);
- The conservation of energy when $K_s = 1$ (rectilinear wave propagation);
- The concentration of energy when $K_s > 1$ (convergence of waves).

The calculations of the refraction of the swell between the open sea and the coast are carried out by the digital SWAN model.

3.2.3 Application of the model

The software models the propagation of the swell by considering these phenomena:

- Refraction on the bottoms and around the structures
- Friction on the bottom
- Surge

The best practice for effectively applying the model is refining the grid according to the area of interest. Meshing is very important to reduce computation time and improve accuracy. In this study, the calculations were performed first on a coarse grid for a larger region, and then the results were used as boundary conditions for a finer grid.

Meshing must be performed using Cartesian or Spherical coordinates. Additionally, SWAN can also simulate unstructured grids called irregular grids and consist of triangles or tetrahedra in an irregular pattern. This is relevant for complex bottom topographies in shallow areas and irregular shorelines. Therefore, since the calculations are performed on a grid, SWAN is a Eulerian model that considers the refractive propagation over different bathymetries and current fields. This model solves the discrete equilibrium equation. SWAN represents the directional and non-directional spectrum at any point of the computing grids through spectral and time-dependent parameters of the waves, such as wave height, maximum or average period, wave direction, and energy transport.

The application of SWAN in this study is carried out using two computational grids, a coarse offshore-to-shore grid and a high-resolution grid in the local region of interest. The resolution of the nested grid allows the precise definition of the WEC position in the array and the precise simulation of their operation. This is a prerequisite for a detailed assessment of the effects of the wave farm, as mentioned by Carballo & Iglesias, 2013.

3.2.4 Bathymetry Data

The bathymetry used for the refraction study is taken from the GEBCO website (GEBCO, n.d.). The bathymetry was extracted as a table using the SURFER software. To improve accuracy, for the coastal zone between -22m up to 0m, the data extracted from the GEBCO website was replaced by data obtained during the in-situ bathymetry measurement (2016). Figure 3.1 represents the bathymetric data of the Palm-Beach Azur zone in the SURFER software.

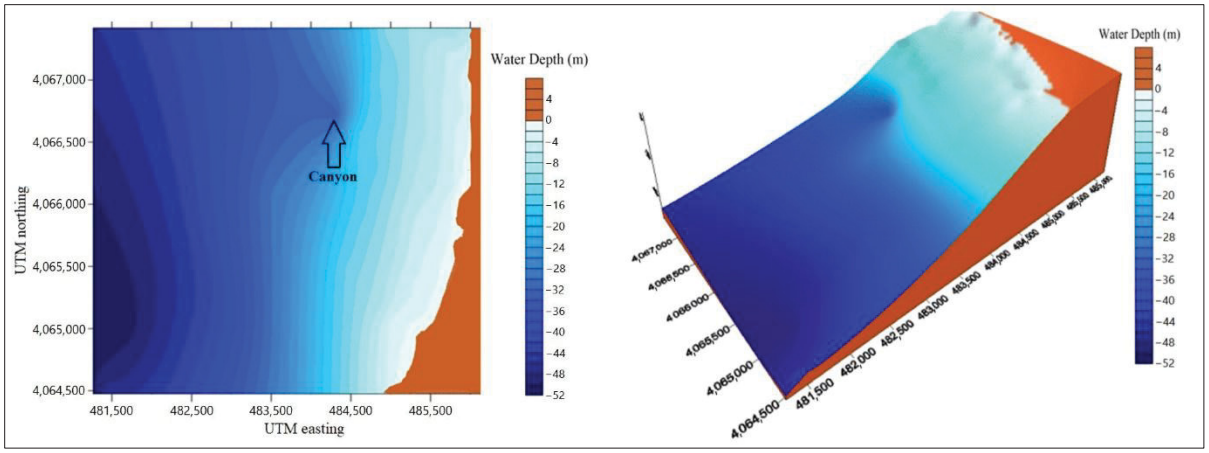

Figure 3.1 The bathymetric map of Palm Beach-Azur

As shown in Figure 3.1, the contour lines are regular and parallel to the coast coming towards the coast and more spaced going towards the open sea, with the presence of a pit, which means a fall to the depth of 23m on the Northeast side. The general average slope of the bottom is of the order of 1%.

Two bathymetric grids were prepared, a large grid that covers deep water depths up to −100m and a small grid of −50m. In this study, the −50m grid is of interest. The −100m grid is only used to determine the characteristics of the swell in the −50m grid. Once the bathymetry map was projected by SURFER software, the bathymetry was extracted for all the grid points. The depths were recorded as (.dat) files. Then, they were incorporated into MATLAB and imported into the SWAN model.

3.2.5 Offshore Swell Data

The offshore swell data used for the refraction calculation is from the Summary of Synoptic Meteorological Observations (SSMO, n.d.), consisting of ships' observations from 1963 to 1970. Statistical processing of these data provided the frequencies of swells' appearance by direction and period. The periods were chosen according to the probability of distribution of exceeding a swell of a given amplitude. Swells of high amplitude have a relatively low

probability of occurrence. Table 3.1 relates the swell conditions used in the context of this study.

Table 3.1 The characteristics of the decadal swells used in the SWAN model

Offshore swell direction	Peak period (S)	Significant height offshore (m)
N 340°	8	6.8
N 30°	9	7
N 280°	10	8

3.2.6 WEC Type and Integration Data

We used the same method as (Carballo & Iglesias, 2013) to determine the effects of WECs installation on the erosion of the Palm Beach-Azur. The WEC we use is the Wave Cat illustrated in Figure 3.2 (Fernandez et al., 2012) . It is a floating WEC whose operating principle is oblique overtopping. It should be deployed at sea (in 50-100 m of water) and produces a limited impact on the shoreline. It is composed of two convergent hulls with a single point mooring to a Catenary Anchor Leg Mooring (CALM) buoy which allows the device to orient itself passively with the direction of wave propagation. The Wave Cat's bows are kept afloat, and incoming waves propagate through the space between the hulls. When the wave crests overtake the inner sides of the hull, the overflowing water is collected in tanks at a level above the external sea level. Then, the water is discharged to the sea and drives turbine generator units. The device acts as a single-shell body by reducing the angle to 0° and effectively closing.

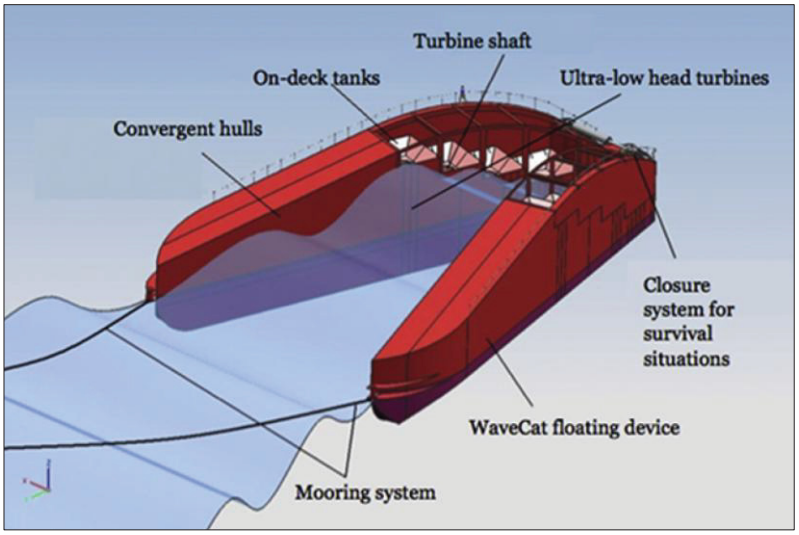

Figure 3.2 Schematic of the WaveCat energy converter
Taken from Fernandez et al. (2012, p. 60)

To study the impact on beach erosion, we are introducing 13 Wave Cat Overtopping converters arranged in 2 parallel rows, the first row having 7 WECs and the back row containing 6 WECs (Figure 3.3). The WECs are installed at a depth of 20m, and the distance between them is 2.2 times the distance D. The distance D represents the distance between the two most extended arcs of a single Wave Cat which equals 45m.

The WEC and wave field interaction is modelled using the transmission coefficients of the waves obtained during laboratory tests carried out at the Porto laboratory by Fernandez et al., 2012. The transmission coefficients are calculated as the ratio between the wave heights measured downwind and in front of the WEC under different wave conditions. The results showed that the wave transmission coefficient exhibited very low variability (K_t=0.76). Therefore, constant value is used in the medium and long-term analysis. Furthermore, the limited range of wave conditions prevented the development of a frequency-dependent model.

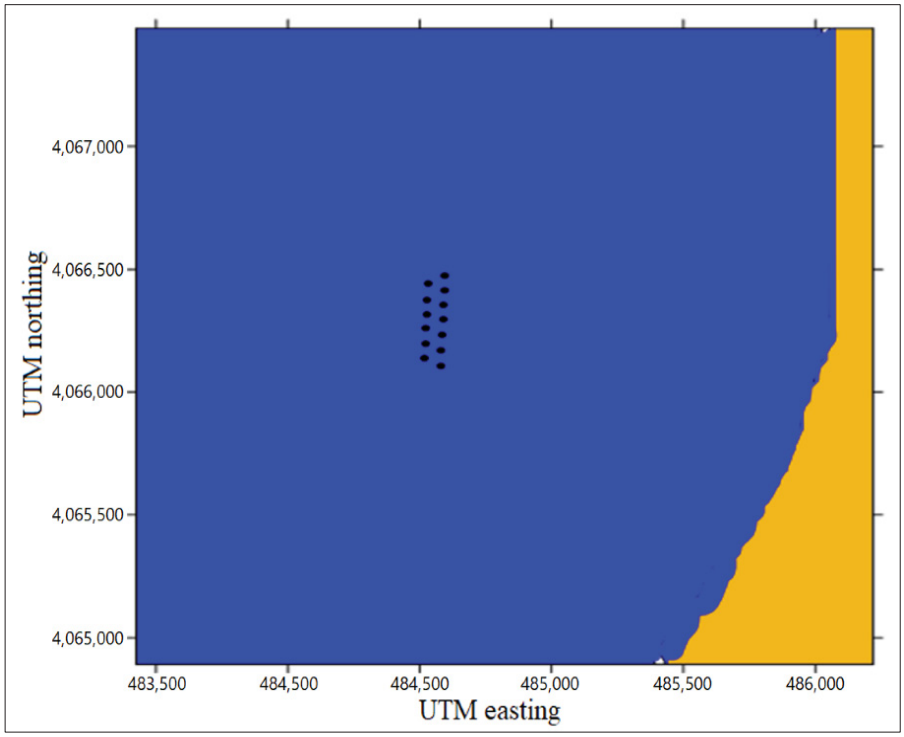

Figure 3.3 WEC location configuration in the study area

3.3 Zone of Study

3.3.1 Geographical Location

The Bay of Bou Ismail, formerly Castiglione, is one of the most prominent bays on the Algerian coast. It is located in the central part of the Algerian coast, 50 km west of Algiers, in the Tipaza region. It is between 2°25’ in the west and 2°55’ in the east. The Palm Beach-Azur area is in the eastern sector of the bay of Bou-Ismaïl in the municipality of Zéralda, about 27km west of Algiers, extending over 2000 m. It is delimited to the west by the Mediterranean Sea, east by the municipality of Zéralda, north by the presidential port, and south by the transverse ground and the breakwaters of the tourist complex of Zéralda (Figure 3.4). This area is important because of its proximity to the capital city and its opening to the Mediterranean Sea. As a result, it is an object of interest and a point of attraction for tourists. Therefore, its protection from coastal erosion is very important.

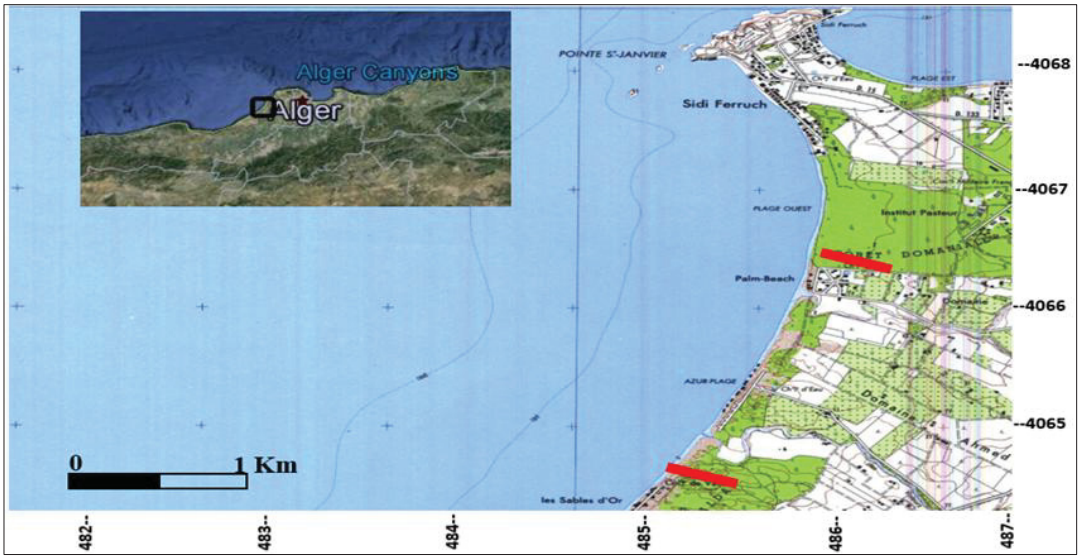

Figure 3.4 Geographical location of the Palm Beach-Azur area
Adapted from Belkacem (2010, p. 41)

3.3.2 Sedimentology of The Zone of Study

The bay of Bou Ismail is characterized by a diverse sedimentological texture based on nine facies: fine sands, fine silty sands, sandy silts, gravelly sands, silted gravies, coarse sands, fine gravels, pure, and rocky. As illustrated in Figure 3.5, the coastal zone of Palm Beach-Azur is dominated by fine and coarse sand from 0 to 20m. Below this depth, sandy and pure silt dominates the zone until 100m deep, where the silted gravel appears.

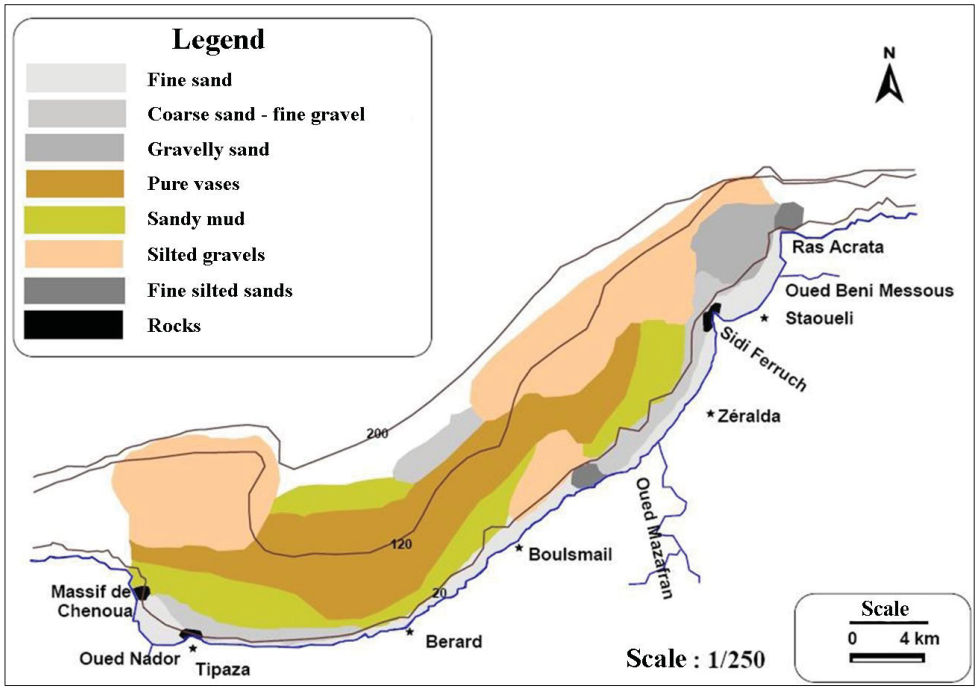

Figure 3.5 Sedimentology of the Bay of Bou-Ismail
Adapted from Houma F. (2009, p.32)

3.3.3 Climate and Wind Data

Wind generates waves and currents, and their impacts increase with their speeds. When the action of the winds is continuous, they generate swells. In the bay of Bou-Ismail, the distribution of the winds is ideally linked to the annual swell regime. The data collected by the SSMO (Summary of Synoptic Meteorological Observations) off the coast of Algeria confirms the existence of two distinct periods:

I. A winter period (October-March), with prevailing winds from the west, with a frequency ranging from 60 to 80%

II. During summer (April-September), the prevailing winds are from the east and the northeast, with 45 to 75% frequencies for the northeast direction.

Figure 3.6 depicts the annual distribution of wind in the study zone. Winds from the West (W) direction have an average maximum speed (average extreme winds) of 19.5 m/s.

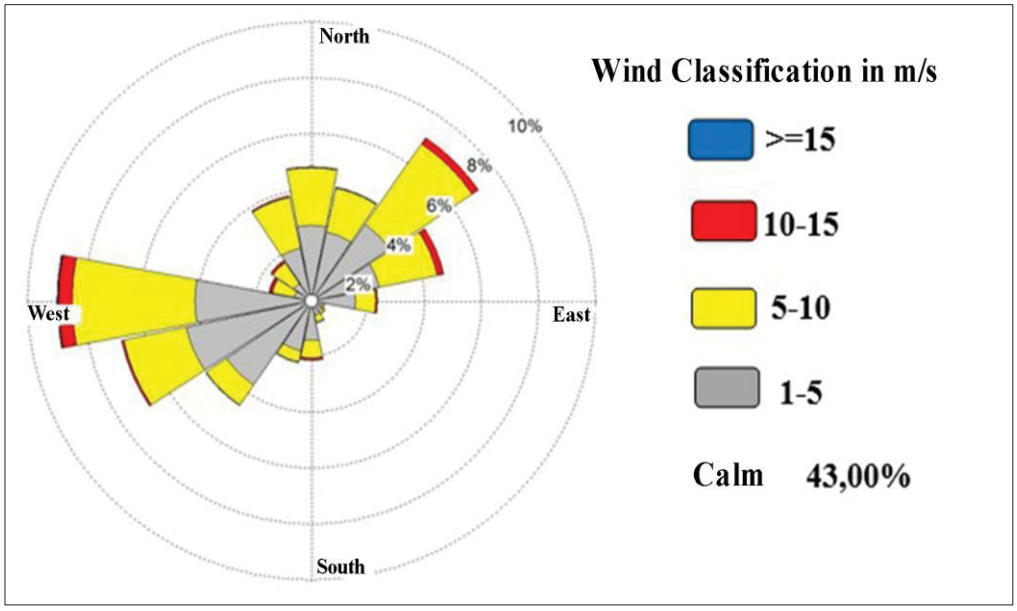

Figure 3.6 Annual wind distribution in percent

3.3.4 The Sea Swells

The swell characteristics determine the sedimentary displacement in the breaking zone, the volume and the direction of the sediment transit and its incidence on the coast. These characteristics condition the dimensioning of the coastal protection structure and its implantation. The primary data source is the SSMO data in the Algiers region, conducted by the U.S Naval weather service Command (SSMO, n.d.). The monthly wave frequencies analysis shows that:

The highest appearance frequencies are related to those swells from the west, east, and northeast. The weakest ones are recorded for swells in the north and north-west directions. The frequencies of observations over the year of the Easterly and westerly swells are roughly identical. However, a slight predominance of the eastern sector exists. Storm swells mainly come from the western sector.

From Figure 3.7, we conclude that the swells distribution is generally consistent with the wind regime:

- In winter: Western swells dominate with the majority of amplitudes of 1 and 3 m and can reach up to 4 m.
- In summer: The most dominant swells come from the northeast sector with smaller amplitudes, and the swells from the west are pretty significant.

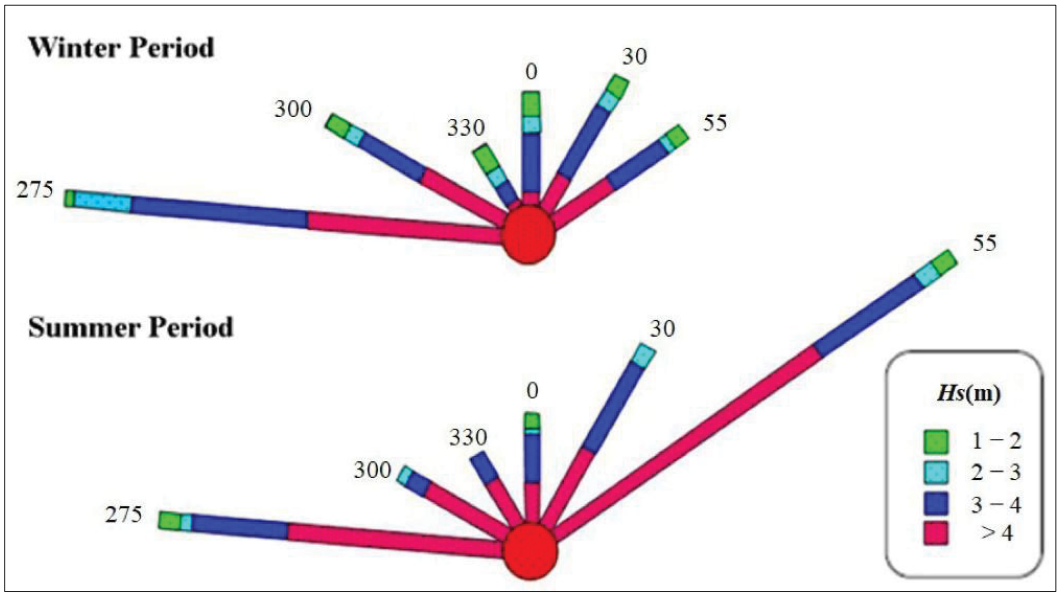

Figure 3.7 Swell direction summary roses off the sector (275°-55°)
Adapted from Zemenzer, S. (2024, p.26)

3.4 Results

3.4.1 Wave modeling

Several tests illustrate the wave propagation, but we chose to present the most significant case, with a wave height H_s = 8m, period T = 10s, and direction of 280° N, without integrating wave energy converters in the grid (Case 1). The SWAN model allowed us to obtain results shown in Figure 3.8. It shows the propagation of the sea swell towards the coast on the large grid, coming from depths of more than 100 m. The wave depth contours are regular and parallel to the coast. Therefore, the wave direction is perpendicular to the coast.

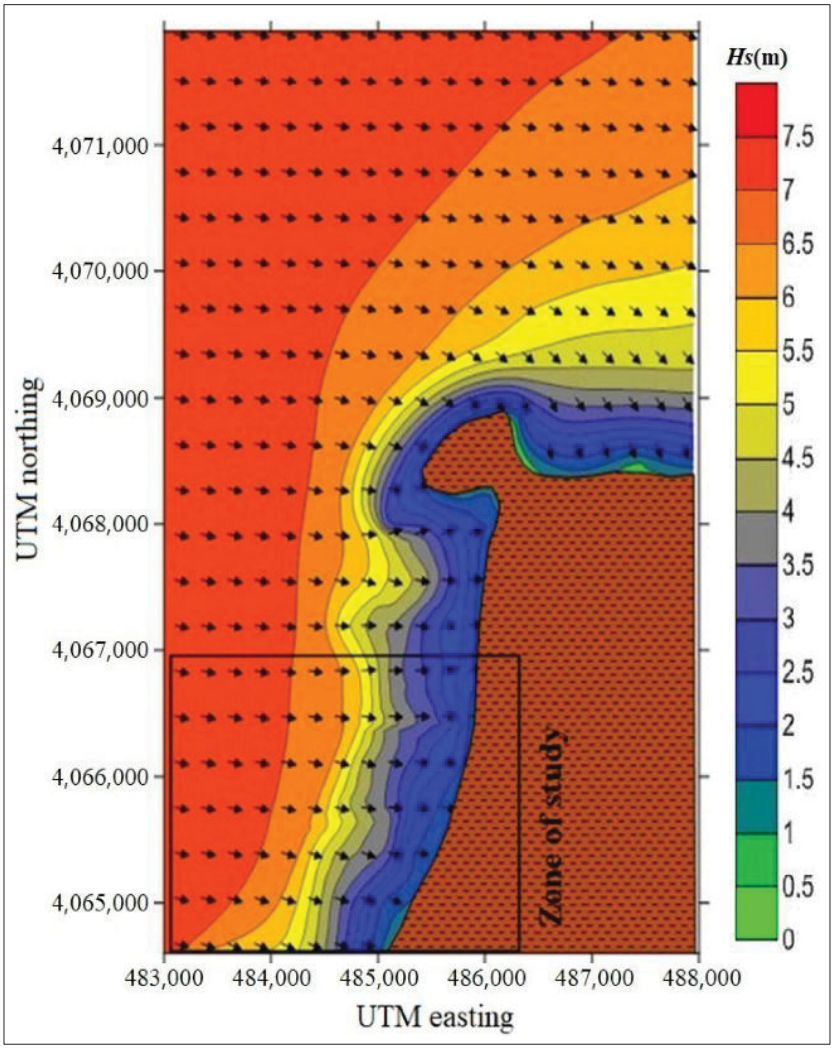

Figure 3.8 Wave refraction for a direction of 280° N and a wave period of 10s

Figure 3.9 shows the small grid for depths of 50 m. The computation uses the swells calculated from the large grid as boundary and initial conditions. West-trending swells are the most energetic in the area, so they are presented here. Their propagation is perpendicular to the Palm Beach-Azur shoreline because of the region's morphology perpendicular to that direction. This study found that the swell conditions within 50m were as follows: wave direction = 280°N, significant wave height (H_s) = 5m, and wave period (T) = 7 seconds. The results are presented on the following maps:

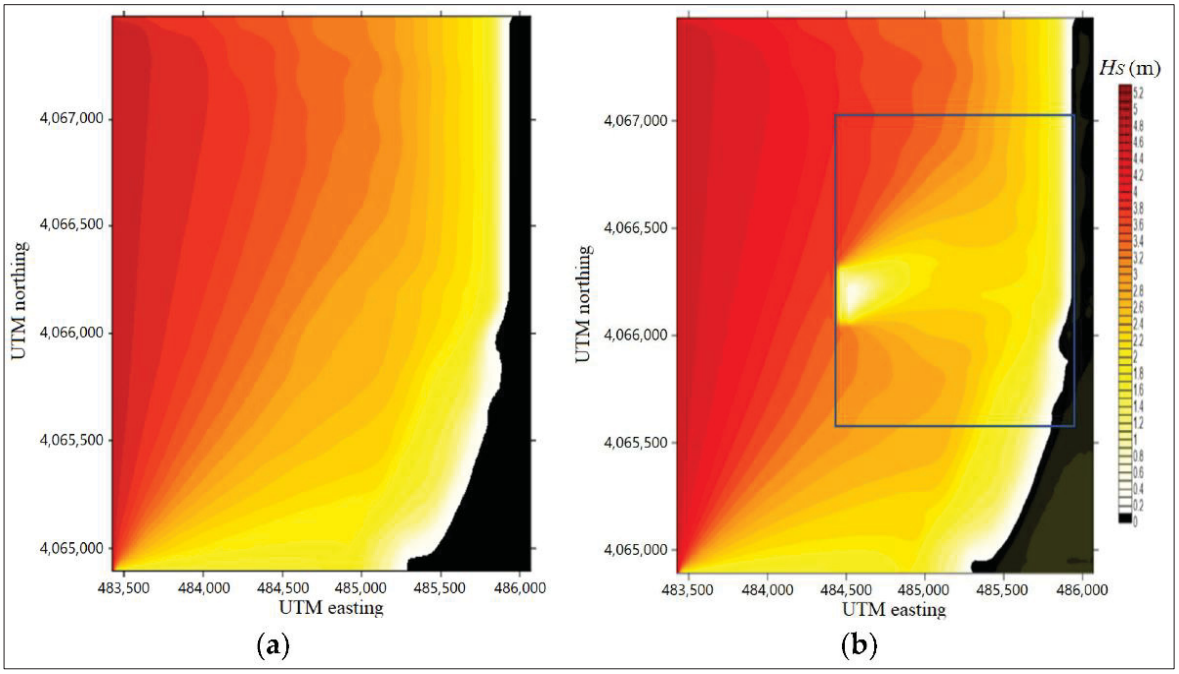

Figure 3.9 Contours of H_s obtained using the SWAN model for a direction of 280° N, H_s=5m and T=7s: (a) after the integration of the WECs; (b) before the integration of the WECs

In Figure 3.9 b, without WECs, we have regular isolines of H_s. The wave height decreases in the presence of WECs (Figure 3.9 a), mainly at the WECs level, and continues up to the coast. At the WECs' level, the H_s was 1.1 m instead of 3.6 m, and it continues to decrease along its path until it arrives at the coast with zero depth. With the de-crease in H_s, we can see that WECs can dissipate energy, demonstrating their potential for energy production and coastline protection.

An area was selected to calculate the ΔH_s and precisely observe the impacts of WECs on wave height. This zone is depicted in Figure 3.9 b. In this area, the significant wave height (H_s) and the ΔH_s between the two cases were calculated and presented in Table 3.2. As we notice from the wave height data analysis, there is a decrease in the mean value of H_s by ΔH_s = 0.3 m. That represents a 30% decrease in the height of the significant waves in the area. The Shoaling Coefficient also confirms this. After installing WECs, the wave field will diverge more due to the change in the Shoaling Coefficient (K_s). K_s at 10 m depth, on average, equals 0.512 without WEC and 0.452 with WEC, where these swells reach the coastline without changing direction.

As they approach the coast, the swells only lose a fraction of their enormous energy. The energy dissipation is pivoting the orthogonal in a northwest to west direction. We measure an average angle of 280.08 and 282.41, respectively, after and before WEC installation.

Table 3.2 The mean ΔH_s and the Shoaling Coefficient for two cases of the presence of WEC (First Case) and the absence of WEC (Second Case)

Parameters	First case	Second case
Average of H_s (m)	2.56	2.26
Average ΔH_s (m)	0.3	
Average ΔH_s (%)	30%	
Shoaling Coefficient K_s	0.512	0.452

3.4.2 Sedimentation pattern near Wave Energy Converters

The profiles closest to the WEC integration zone plotted in Figure 3.10 illustrate the in-fluence of the WEC on the bathymetric profile. We superimposed the maps of the two cases (with and without WECs) to draw the sedimentation profile from the WECs' location towards the shore.

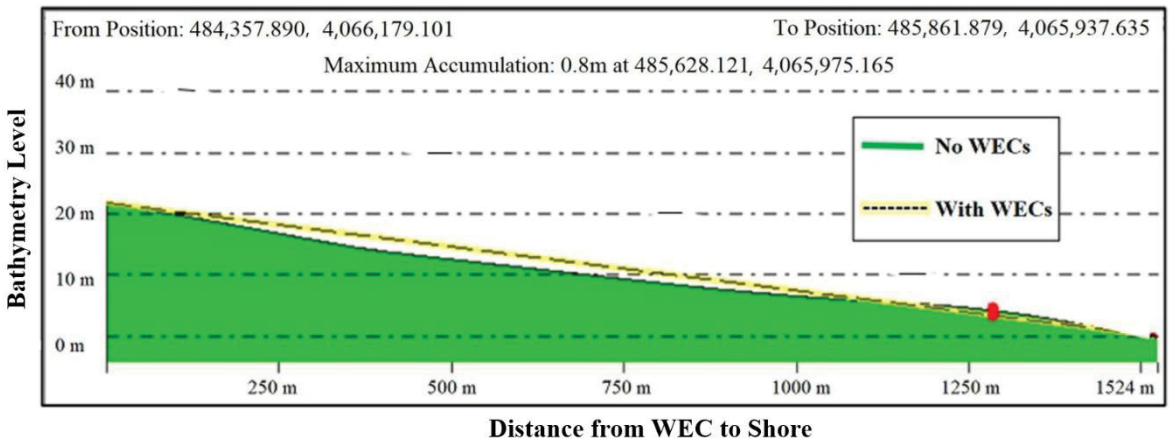

Figure 3.10 Sedimentation profiles of the two cases: Case 1 in the absence of the WEC and Case 2 in the presence of the WEC

As seen in Figure 3.10, there is a distinctive difference between the two bathymetric profiles, as displayed by Case 1 (without the integration of WECs) being below Case 2

(with the integration of WECs). There is an accumulation after the installation of the WEC, with a maximum accumulation of 0.8 m. This bathymetric change is the result of the decrease in significant wave height (H_s) and energy dissipation near WECs. Therefore, we can deduce that the installation of the WEC can serve a dual role, the extraction of marine energy to convert it into electrical energy and the protection of coasts against marine erosion according to the results of sediment deposition of 0.8 m.

3.5 Conclusions

Waves have the potential to provide a sustainable source of energy that can be transformed through energy converters into electrical energy in shallow or deep water. Erosion is a natural phenomenon mainly linked to meteorological and hydrodynamic effects. In addition, the human influence on the shore accelerates and worsens erosion patterns in coastal regions.
Palm Beach-Azur, the subject of this study, is located in the eastern part of the Bay of Bou Ismail. It is one of the most significant beaches on the Algerian coast. This study aimed to determine the impact of Wave Cat Wave Energy Converters (WECs) on wave hydrodynamics and marine erosion.

In this study, the presence of WECs correlated to a decrease in the shoaling coefficient, confirming that the WECs captured wave energy as wave heights declined. Moreover, it has been seen that the WECs changed the bathymetric profile so that an accumulation of sediment appeared. Therefore, we conclude that WECs can be used to protect shorelines from marine erosion while transforming wave energy into electrical power.

As observed, WECs can play a dual role in power generation and coastline protection, yet their economic feasibility still poses an issue. However, the high installation cost of WECs can be justified when considering they eliminate the need for the construction of erosion protection structures.

CHAPITRE 4

IMPACT OF WAVE ENERGY CONVERTERS AND PORT LAYOUT ON COASTAL DYNAMICS: CASE STUDY OF ASTARA PORT

M. Moradi [a] and A. Ilinca [b]

[a, b] Department of Mechanical Engineering, École de Technologie Supérieure, 1100 Notre-Dame West, Montréal, Quebec, Canada, H3C 1K3

Paper published in *Energies*[3], May 2024

Abstract

In the face of depleting fossil energy and the imperative of sustainable development, there is a compelling drive towards advancing renewable energies. In this context, sustainable and predictable alternatives, like marine energy, gain prominence. Marine energy presents a cleaner option devoid of the adverse effects associated with fossil fuels, playing a crucial role in environmental sustainability by safeguarding coastlines against erosion. This study focuses on Astara Port in the Caspian Sea, exploring the utilization of wave energy converters (WECs). The originality of this study's research lies in exploring WECs' dual role in energy generation and coastal protection. Using MIKE21 software simulations, the impact of number, location, arrangement, and orientation of WECs across various scenarios was investigated, including two WEC number scenarios (11 and 13), three structural placement scenarios (north, front, and south of the port), two structural arrangement scenarios (linear and staggered), two port layout scenarios (original layout and modified layout), and two orientation scenarios for the structures (facing north-east, which is the dominant wave direction, and facing southeast). The results show a remarkable decrease in the significant wave height behind WECs, notably with 13 staggered devices facing dominant waves (from northeast), reducing the significant wave height H_s by 23–25%. This setup also shows the highest wave height reduction, notably

---

[3] Moradi, M.; Ilinca, A. Impact of Wave Energy Converters and Port Layout on Coastal Dynamics: Case Study of Astara Port. *Energies*, 2024, 17, x. https://doi.org/10.3390/xxxxx

36.26% during a storm event. However, linear WEC setup offers more extensive coastline protection, covering 47.88% of the model boundary during storms. Furthermore, the 11 staggered WECs facing southeast (SE) arrangement had the lowest sediment accumulation at 0.0358 m over one year, showing effective sedimentation mitigation potential. Conversely, the 13 linear WECs facing northeast (NE) had the highest accumulation at 0.1231 m. Finally, the proposed port design redirects high-velocity flow away from the port entrance and removes rotatory flow, reducing sediment accumulation near the harbor entrance.

Keywords: wave energy converter (WEC); renewable energy; MIKE21 model; wave height

4.1 Introduction

In pursuing Sustainable Energy Development, a pivotal consideration lies in substituting fossil fuels with a myriad of renewable energy sources. This imperative has led to an escalating demand for the augmentation of renewable energy production. Within the spectrum of renewable energy generation methodologies, wave energy production emerges as an up-and-coming option due to the high density of water, the predictability of waves, and the minimal environmental footprint. Despite its immense potential, wave energy is still in its infancy, necessitating further in-depth research and substantial investment to establish it as a dependable and recognized source of energy production in the scientific and technological domain (Falcão, 2010).

Numerical and experimental studies have delved into this energy source, revealing its potential for sustainable and reliable energy production and its role in safeguarding coasts and ports from erosion, sedimentation, and storms (Clemente et al., 2021; Guiberteau et al., 2012, 2015; Pastor & Liu, 2016).

Wave energy converters (WECs) are key players in emission reduction efforts. They generate clean electricity from renewable ocean waves, helping to reduce our dependence on fossil fuels and their associated emissions. WECs offer a low carbon footprint and minimal environmental

impact compared to traditional power plants, preserving marine ecosystems while diversifying our energy mix. In a recent study, Choupin et al. (Choupin et al., 2021) analyzed wave energy converters' role in reducing emissions. They introduced a process for optimal converter location pairs, considering various factors. The study in Southeast Australia highlighted spatial variations in nearshore pairs and introduced an Index to rank areas based on their energy demand.

Given the hefty costs tied to wave energy converter (WEC) development, numerical simulation is vital for refining design precision and deployment strategies, leading to cost-effective modeling of renewable wave energy. Smith et al. (Smith et al., 2012) employed numerical wave models and adapted SWAN codes to evaluate the influence of offshore wave farms on the nearby wave climate. Their findings demonstrate the correlation between the extent of the impact and the response characteristics of the devices, as well as the spectral sea state under consideration. In another study, the SWAN coastal model was used to investigate the impact of WEC arrays on surrounding wave conditions. The results showed that WEC arrays could create wakes up to 200 m behind, reducing estimated power performance by 2.3% to 6.0% (Luczko et al., 2018).

Physical modeling of WECs through scaled prototypes in controlled environments offers insights into real-world performance and helps optimize design for increased efficiency and reliability. Through physical model tests, Ruol et al. (Ruol et al., 2011) explored the efficiency and transmission characteristics of the DEXA wave energy converter, investigating its potential dual applications. They proposed deploying a DEXA array in Marina di Ravenna to evaluate its impact on longshore sediment transport, possibly re-versing the net transport direction. The study concluded that a WEC farm reduces coastal wave energy, significantly affecting sediment transport. Nader et al. (Nader et al., 2017) introduced a new experimental method for studying WEC arrays, overcoming cost and complexity barriers. They aimed to understand array performance and develop accurate modeling techniques. Initial results showed promising insights into array hydrodynamics, suggesting potential design improvements.

The distance between a wave farm and the coast significantly influences energy production and environmental effects. Optimal placement of WECs involves considering factors such as wave resource availability, transmission losses, and ecological and environmental effects. Abanades et al. (Abanades et al., 2015) examined the influence of the distance between a wave farm and the coast. Their study, conducted in Perranporth (UK), revealed that the closest farm offers the most significant protection, resulting in up to a 20% reduction in erosion. However, this proximity entails a minor trade-off, leading to a slightly smaller wave resource by approximately 10%.

The Wave Dragon is a Wave Energy Converter (WEC) designed to harness energy through overtopping. It captures energy primarily by directing waves onto a ramp and into a reservoir and a set of Kaplan turbines; some studies have investigated the mechanism of this type of WEC in detail (Ahmad et al., 2024; Eskilsson et al., 2015; Frigaard et al., 2004; Jafari et al., 2018; Moradi, Chertouk, et al., 2022; Peter et al., 2006, 2007). Robertson (Robertson, 2010), in a study, compared the Wave Dragon Over-Topping Device and the Pelamis for deployment along the coasts of Vancouver Island and the Queen Charlotte Islands. Results showed that both devices have promising capacity factors: Pelamis achieved 51% on Vancouver Island and 59% on Queen Charlottes, while Wave Dragon reached 21% and 30%, respectively. This suggests significant opportunities for efficient renewable wave energy generation in these regions. In another study, Iglesias et al. (Iglesias & Carballo, 2014) investigated how the distance of a wave farm from the coast affects near-shore wave conditions. They used case studies with varying distances (2 km, 4 km, and 6 km) and wave conditions. The study results showed that increasing the distance from the coast doesn’t consistently reduce the Maximum absolute Nearshore Impact, and the distance influences where the maximum impact occurs along the coast. Extensive laboratory testing on a scale model of a Wave Dragon energy converter was conducted from 1998 to 2001 at Aalborg University (Kofoed et al., 2000), leading to the creation of a 57 × 27 m prototype in Nissum Bredning, Denmark, which became the world’s first offshore wave energy converter in May 2003. Kofoed et al. (Kofoed et al., 2006) concluded that the turbines face three main challenges: operating at low head values (0.4 to 4.0 m), dealing with frequent regulation due to wave overtopping variations and limited

storage, and operating in a harsh environment with minimal maintenance on an unmanned offshore platform.

Nørgaard et al. (Nørgaard et al., 2013) conducted experimental investigations using a 1:51.8 scale physical model of the 260 × 150 m, 24 kW/m model Wave Dragon device. Their study also examined the influence of the Wave Dragon's mooring system and reflector joints on wave height reduction and transmission.

Given the significance of waves, their influence on coastal areas, and their considerable energy generation potential, this study utilizes numerical modeling to examine the impact of Wave Dragon devices on nearshore wave and flow characteristics. The innovation of this study stems from exploring the dual role of WECs in energy generation and coastal protection, comparing linear and staggered arrangements, analyzing orientation effects, and proposing a novel port design for sedimentation management to move it away from the port entrance. Various scenarios are being investigated to simultaneously achieve coastal protection and maximize energy generation. Reducing wave height can mitigate coastal erosion and facilitate energy dissipation by the WECs, with the dissipated energy being convertible to electricity.

4.2 Materials and Methods

This research used the two-dimensional hydrodynamic model MIKE21 2024 software and its subsets to model the wave and flow patterns in the study area. The model uses wind speed, wind direction, wave height, wave period, and bed topography as meteorological, hydrodynamic, and geographical input data. This investigation delves into examining Astara Port in the Caspian Sea. It underscores the port's significance and the critical need to prevent coastal erosion and sedimentation in its vicinity. Furthermore, the study explores the feasibility of harnessing wave energy for electricity generation. It is worth noting that the methodology employed in this investigation is transferable to similar ports facing comparable challenges. In future studies, using Boussinesq-type equation models and software like MIKE21 could be

beneficial for simulating hydrodynamic conditions and sediment transport in offshore, coastal, and harbor areas (Gao et al., 2020, 2023).

4.2.1 MIKE21 Mathematical Model

For the analysis of marine phenomena, the MIKE21 model is one of the most practical models developed by the Danish Hydraulic Institute (DHI). MIKE21 is a suitable tool for analyzing phenomena such as wave patterns, current, sedimentation, determination of sediment transport rate, wind-generated waves, and specific shallow water (SW) processes such as wave breaking, erosion, and bed effect (DHI MIKE, 2017).

The mathematical equations used in the SW module are the equations of equilibrium density of the wave spectrum, which are solved in the frequency range of the wave's zero-order and first-order energy spectra using the finite difference method and ADI (Alternating Direction Implicit) technique (Holthuijsen et al., 1989).

$$\frac{\partial(c_{gx}m_0)}{\partial x}+\frac{\partial(c_{gy}m_0)}{\partial x}+\frac{\partial(c_g m_0)}{\partial \Theta}=S_0 \tag{4.1}$$

$$\frac{\partial(c_{gx}m_1)}{\partial x}+\frac{\partial(c_{gy}m_1)}{\partial x}+\frac{\partial(c_g m_1)}{\partial \Theta}=S_0 \tag{4.2}$$

Here, m_0 and m_1 are zero and first-order momentums, respectively; C_{gy} and C_{gx} are wave group velocity components; C_o is wave propagation velocity, which indicates changes in wave power in the direction of θ; S1, and S_0 are energy sources, which can be increased by wind, or decreased by energy dissipation due to bed friction and wave break. In the above equations, $m_n(\theta)$ can be calculated using equation below:

$$m_n(\Theta)=\int_0^{\infty}\omega^n A(\omega\Theta)d\omega \tag{4.3}$$

where ω is the frequency, and A is the wave power spectrum density. For hydrographic maps used in the SW module, the ratio of the distance of the computational nodes in the y and x

directions and the maximum angle between the direction of the propagated wave on the x-axis are of great importance. These criteria are as follows:

$$\frac{\Delta x}{\Delta y} \geq 4 \tag{4.4}$$

The maximum angle between the wave propagated direction and the x-axis must not exceed ± 60°. The SW module simulates the wave-breaking phenomenon based on the proposed relations of (Battjes & Janssen, 1978).

$$\frac{dE}{dt} = -\frac{\alpha}{8\pi} Q_b \omega H_m^2 \tag{4.5}$$

$$\frac{1 - Q_b}{\ln Q_b} = -\left(\frac{H_{rms}}{H_m}\right)^2 \tag{4.6}$$

$$H_m = \gamma_1 k^{-1} \tanh\left(\frac{\gamma_2 kd}{\gamma_1}\right) \tag{4.7}$$

where ω is frequency, H_{rms} is the square root of the average squares of wave height, H_m is the maximum allowable wave height, Q_b is friction due to wave breaking, which affects energy dissipation rate, k is wave number, d is water depth, α is the energy dissipation coefficient, γ_1 is a constant coefficient controlling critical wave rise, and γ_2 is a constant coefficient controlling the critical water depth.

Hydrodynamic models can calculate wave refraction, shoaling, wave break, radiation stresses, wave setup, and the velocity of parallel currents on the shore. Wave characteristics, including wave height, wave period, and mean wave direction, are used as a time series. The hydrodynamic model operates by numerically solving the two-dimensional shallow water equations. This includes solving continuity, momentum, temperature, salinity, and density equations. The model uses both Cartesian and spherical coordinates for the horizontal domain. Here, the governing equations of hydrodynamic models are not presented due to document limitations. Additional information is available in (Battjes & Janssen, 1978)

4.2.2 Problem and Solution

Given the common challenges encountered by coastal regions worldwide, including the pressing issue of coastal erosion, it remains crucial to formulate prompt and practical solutions. According to the analysis of the region's wave and wind climate, it was concluded that erosion problems exist in the southern parts of Astara Port. However, the sediment accumulation problem at the port entrance is more severe. This accumulation leads to the closing of the harbor with sand washed away from the northern parts of the port. The main problem is keeping the port from being sealed off by accumulating sand. The sand must be removed from the harbor entrance and transferred into the natural longshore sediment transport system. This is usually done through a dredging operation, which requires much effort and is expensive. Figure 4.1 shows the existing erosion and sedimentation patterns in the southern and northern parts of the port, respectively. This problem exists in most ports around the world, and if a solution can be identified in this region, it would have positive outcomes for addressing similar issues in ports across the globe.

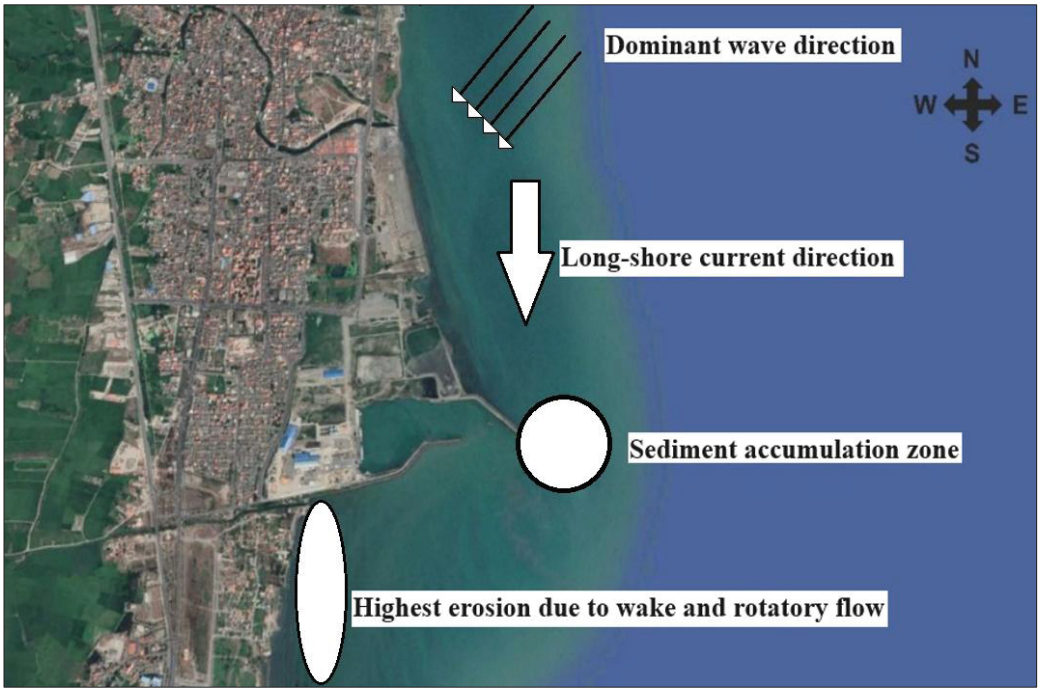

Figure 4.1 Erosion and sedimentation pattern near Astara Port

As mentioned earlier, the erosion in the southern part of the port, as illustrated in Figure 4.1, is problematic and necessitates proactive intervention. It is crucial to address this issue because it can potentially jeopardize the stability of the breakwater structure, which, in turn, is instrumental in maintaining a stable flow pattern near the port. Figure 4.2 shows the transition of the coastline in the southern part of the port over nine years, from 2012 to 2021. In this figure, the white line represents the coastline in 2021, while the yellow line corresponds to the coastline in 2012. It is evident from this comparison that erosion poses a substantial and immediate threat to the properties and stability of the southern areas within the port.

(a) (b)

Figure 4.2 Coastline transition from (a) in 2012 to (b) in 2021

4.2.3 Experimentally Recorded ADCP (Acoustic Doppler Current Profiler) and Bathymetry Data

The calibration of the MIKE21 wave and current model constants require experimental data. These data include the speed and direction of the flow, height, and wave direction at different points. The following section describes the available data used in these studies. Simulation studies of the northern coasts of Iran near Astara Port have involved several measurements in the South Caspian Sea. On the coast of Astara Port, flow features were measured in 2013 at depths of 10 and 25 m (Ports and Maritime Organization (PMO), 2010). This study uses an Acoustic Wave and Current profiler (AWAC) device for current measurement and wave recording (Figure 4.3). Using this device, it is possible to accurately record waves and flow details and calibrate the MIKE21 model.

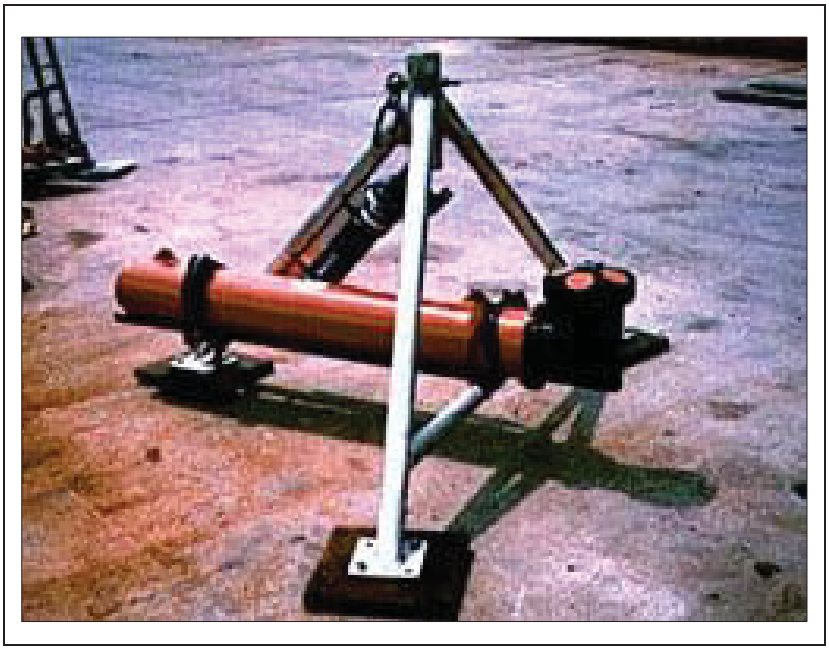

Figure 4.3 Acoustic Doppler profiler used for recording experimental data

4.2.4 Global and Local Models Setup

To set up the model effectively, coastal geography and seabed topography are essential data. Additionally, comprehensive wind speed and direction statistics are vital, as they significantly influence wave patterns, coastal dynamics, and overall hydrodynamics. The wind data was obtained from ECMWF (European Centre for Medi-um-Range Weather Forecasts).

According to these data, the dominant wind direction is from northeast to southwest, the same as the dominant wave direction. To simulate the flow and wave using the global model, an unstructured meshing system was used in the deep-water area, and rectangular grids were used in the southern regions. In the initial stages of configuring the local model, the first step involves furnishing the model with the mesh domain. Given that this study centers around examining Astara Port, the local model is specifically tailored to the vicinity of the port.

Defining the borders of the local model is determined by the project's specific requirements. Once the global model has been calibrated and executed, boundary conditions are extracted from the global model's outputs along the borders of the intended local model.

This extraction process is facilitated using the Data Extraction FM tool within MIKE Zero. Figure 4.4 illustrates the boundaries of the global and local models, their mesh structures, and contours of bathymetric values.

(a)

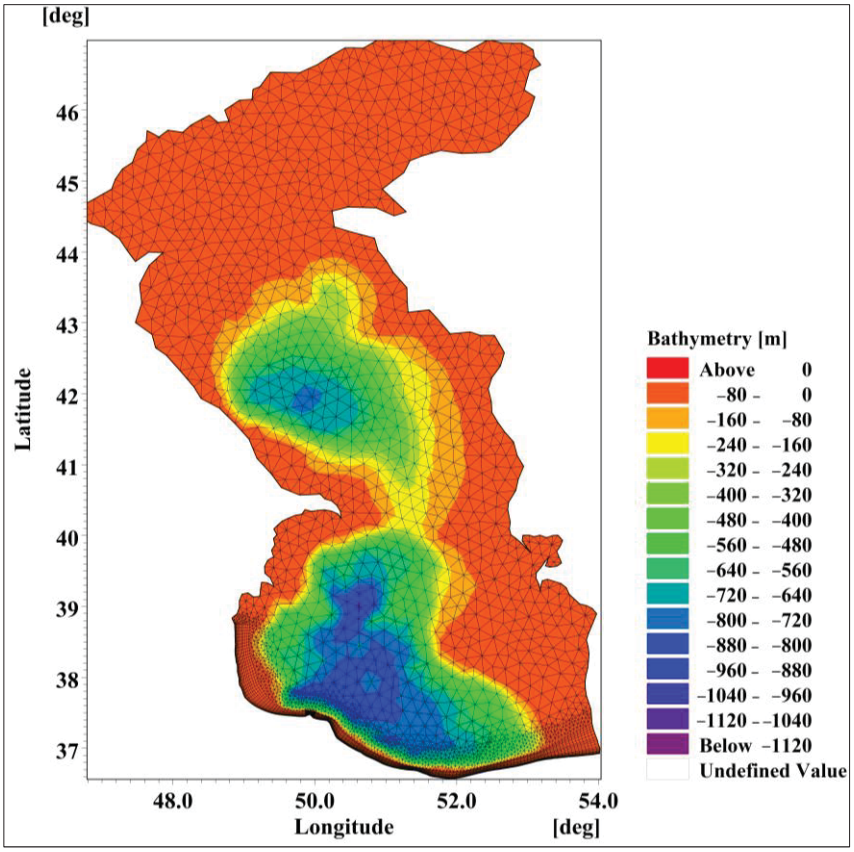

(b)

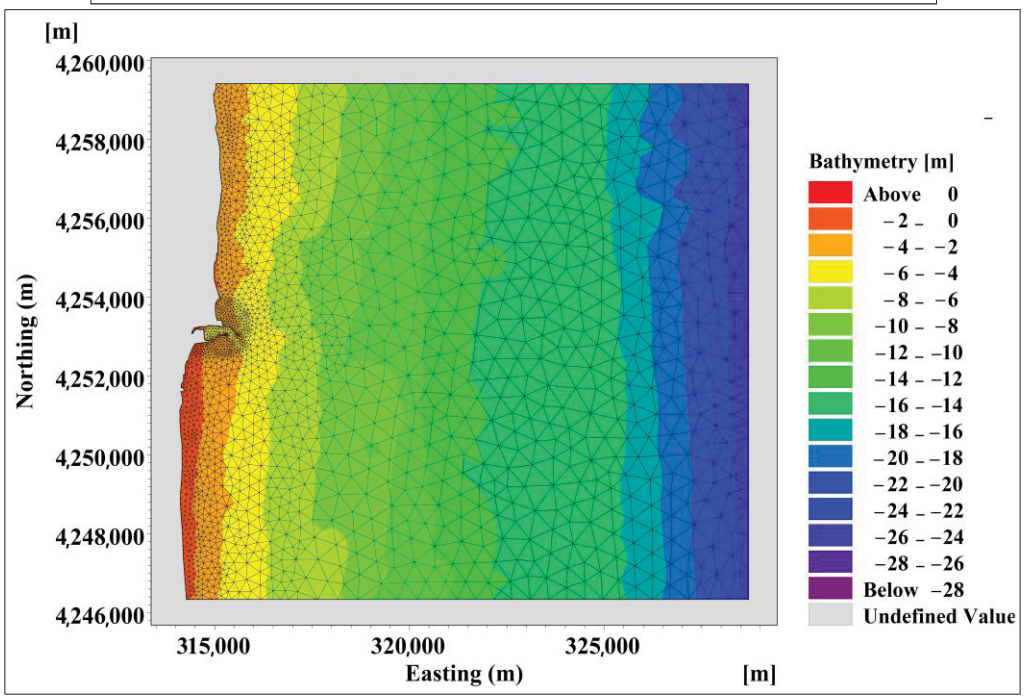

Figure 4.4 Boundaries and mesh grids of the (a) global model and (b) local model

4.2.5 Outputs of the Local Model

The results generated by the MIKE21 local model are validated with experimental data, encompassing variables like flow velocity, flow direction, wave height, and wave direction. It is important to note that the accuracy of the two-dimensional model in predicting flow along the Astara shores is notable due to its ability to calculate the simultaneous influence of both wind and waves. Moreover, the model's simultaneous calculation of both wave and current variables highlights the importance of precise wave feature prediction. As mentioned, ADCP devices were utilized to measure the characteristics of waves and currents at depths of 10 and 25 m near Astara Port. These two points were used to validate the model values (Figure 4.5).

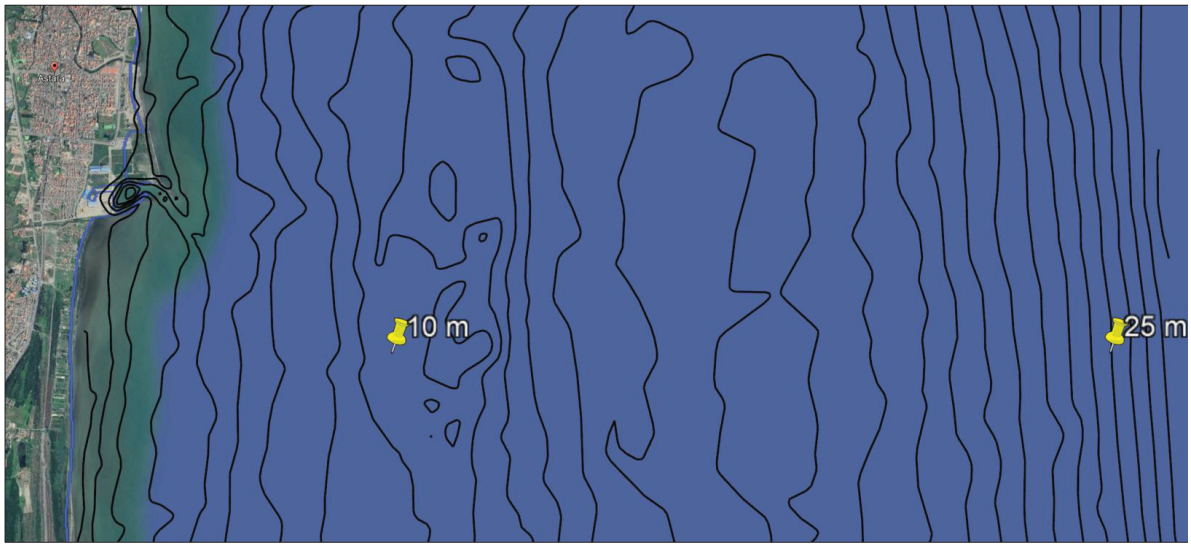

Figure 4.5 The exact location of flow and wave measurements

The local model was established, and the simulations near the port were performed using the global model results. Figure 4.6 shows wave characteristics for one year's modeled and measured data. Figure 4.7 compares measured and modeled depth-averaged current velocity and flow direction in 2013 at the 10 m depth station. As evident in Figure 4.6 and Figure 4.7, current and wave results across the 10 m station suggest that the model's predictions for coastal regions are reasonably accurate, especially for the storm events in the region throughout the year.

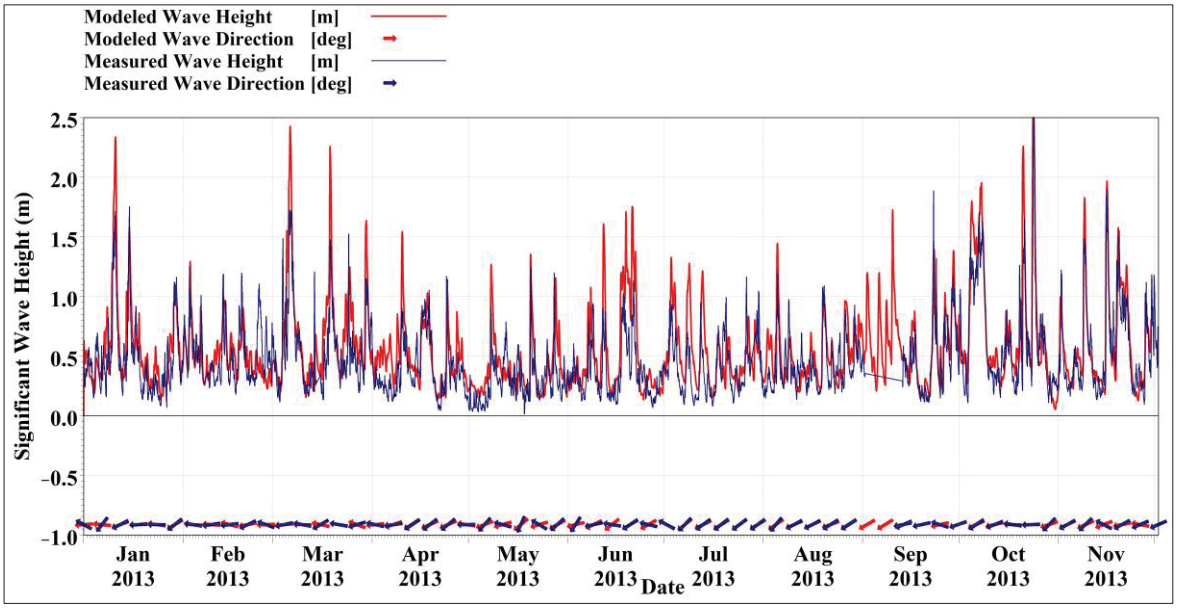

Figure 4.6 Validation of the Spectral Wave (SW) local model using modeled data and measured data at the Astara 10 m station

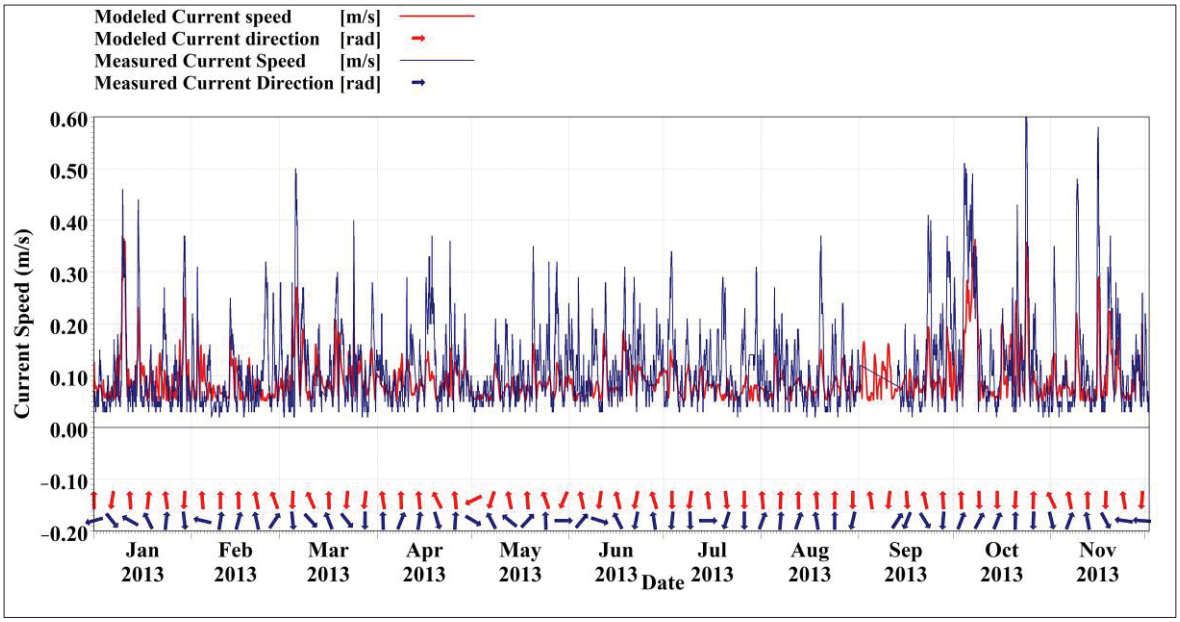

Figure 4.7 Measured and modeled flow direction and velocity at the Astara 10 m station

4.2.6 WEC Type, Placement and Orientation

In the pursuit of achieving outcomes, including erosion control and generating electricity, strategic positioning of WECs was executed. Wave Dragon overtopping devices were used in this study. They are controlled using a mooring system and have six degrees of freedom in the real world. However, due to limitations in the modeling of moving objects within the MIKE21 software and the relatively small movements compared to the scale of the global and local models used in this study, wave energy converters (WECs) are considered static. The device employed in this study is a 76 × 50 m, 12 kW/m model Wave Dragon device that uses wave reflectors to direct waves up a ramp into a reservoir; the stored water then flows through turbines to generate electricity (Figure 4.8).

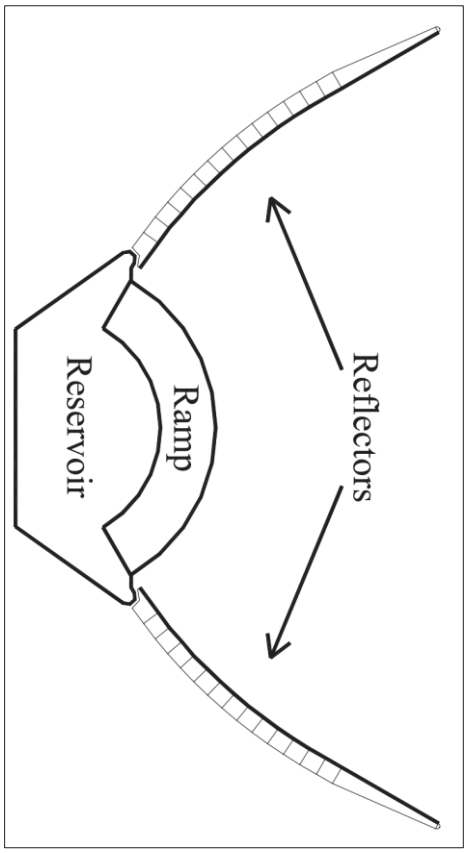

Figure 4.8 The basic layout of the Wave Dragon energy converter
Taken from Soerensen et al. (2003, p. 1)

Testing various scenarios was necessary to maximize wave capture, electricity generation, and energy dissipation to combat coastal erosion. This involved exploring different WEC numbers and arrangements within the wave farm, adjusting the wave farm's location, and modifying the port design. The objective is to optimize energy generation efficiency, protect the coastline, and minimize sedimentation at the port entrance, reducing the need for costly operations like dredging.

In general, the simulations were performed for two WEC number scenarios, 11 and 13; two arrangement scenarios, linear and staggered; two scenarios for the orientation of WECs facing north-east (dominant wave direction) and facing southeast; three wave farm placement scenarios: north, front, and south of the port; and two port layout scenarios: original layout and modified layout (Table 4.1).

Table 4.1 Simulation Scenarios for Wave Energy Converters (WECs)

Simulation Parameters	**Scenarios**
WEC Number	11, 13
Arrangement	Linear, Staggered
WEC Orientation	NE (Northeast) and SE (Southeast)
Wave Farm Placement	North, Front, and South of the port
Port Layout	Original, Modified

For example, 13 Linear NE-Front of the modified port describes a simulation with 13 linearly arranged WECs facing northeast and placed at the front of the modified port layout.

4.3 Results

This section investigates the impact of different scenarios on wave characteristics and sedimentation. To this end, time-averaged point analysis, linear analysis, and aerial data are studied to comprehensively assess how different implementation scenarios affect wave behavior and sedimentation processes.

4.3.1 Time-Averaged Wave Height of Different Points

To assess the influence of structures on significant wave height (H_s), an investigation was conducted at three designated locations in the northern (A), frontal (B), and southern (C) parts of the port. Subsequently, the H_s values were extracted at these specific points over three consecutive months (January to March). Figure 4.9 provides a depiction of the geographical location of these identified locations. Additionally, these points were studied for different scenarios involving the location, orientation, arrangement, and number of WECs. When comparing the no-structure scenario with other scenarios, the analysis reveals a clear reduction in significant wave height around the wave energy converters.

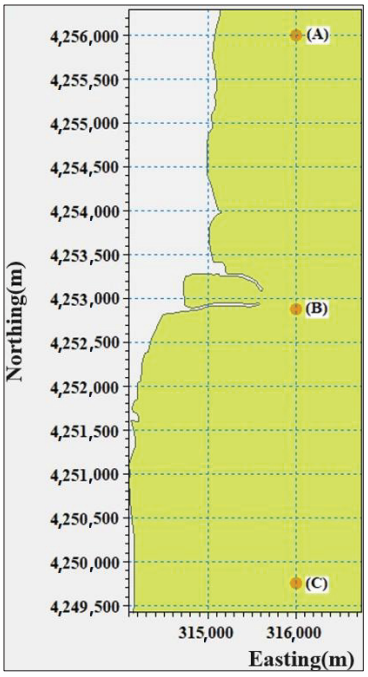

Figure 4.9 Location of the three points studied on the North (A), Front (B), and South (C) of the port

Regarding the impact of WECs across various scenarios, Figure 4.10, Figure 4.11, and Figure 4.12 show that configurations featuring 13 structures oriented towards the northeast with a staggered layout exhibit the most effective reduction in wave height. Following this, scenarios involving 13 structures arranged linearly demonstrate comparatively favorable results. Conversely, configurations comprising 11 staggered structures facing southeast exhibit the least pronounced impact on wave height reduction across all scenarios evaluated.

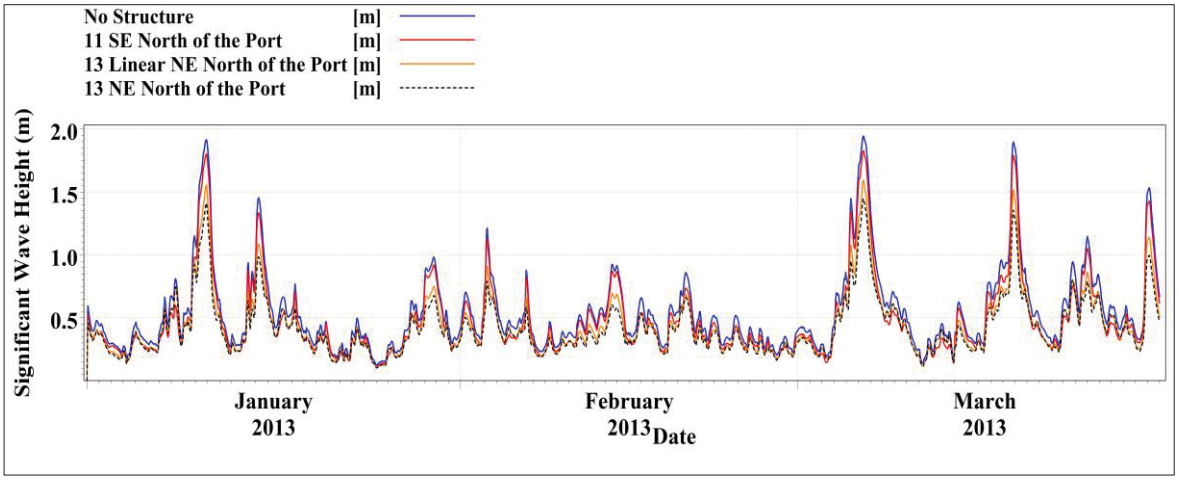

Figure 4.10 Significant wave height (H_s) in point (A) for various scenarios

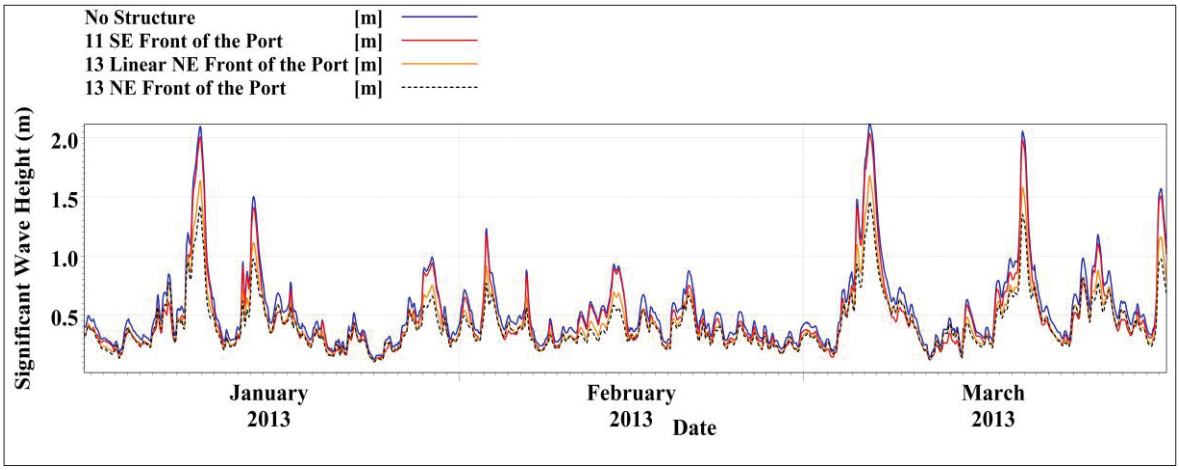

Figure 4.11 Significant wave height (H_s) in point (B) for various scenarios

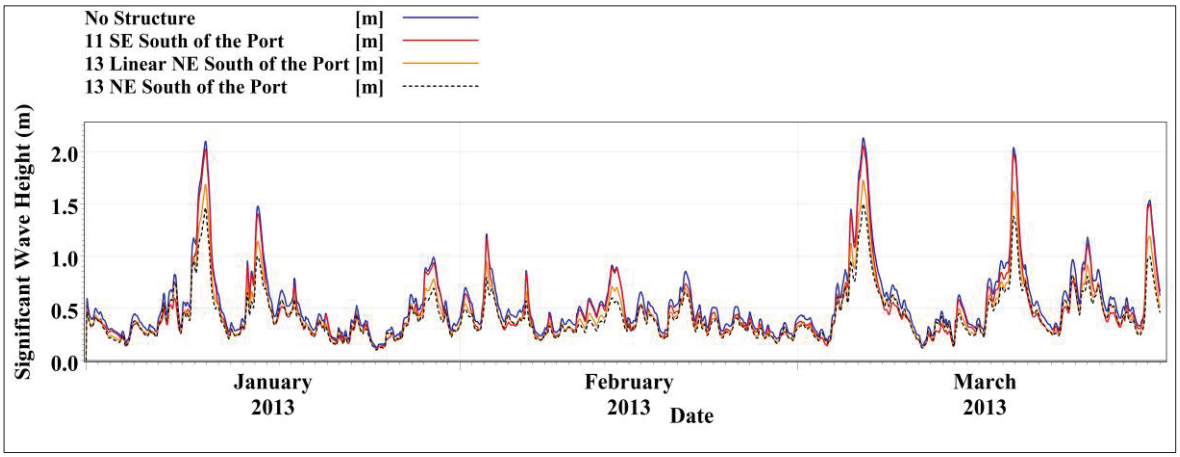

Figure 4.12 Significant wave height (H_s) in point (C) for various scenarios

Following a thorough analysis of the time-averaged results for each of the points above, the data reveal significant decreases in wave height across some scenarios of placements of WECs. Specifically, the simulations involving 13 staggered devices show 23.71%, 25.3%, and 23.57% reductions for points A, B, and C (north, front, and south WEC locations), respectively. For configurations featuring 13 linear wave energy de-vices, the corresponding reductions were 19.31%, 19.91%, and 18.08% for points A, B, and C, respectively. In the case of 11 staggered devices, the reduction values in wave height were 12.29%, 12.46%, and 12.02% for the points on the north, front, and south of the port, respectively. These substantial impacts on the wave height reduction show mitigation of erosion behind the Wave Energy Converters, particularly in the case study involving 13 staggered energy converters facing the dominant wave direction. This configuration resulted in an approximate 23% to 25% decrease in H_s values, indicating notable effectiveness in wave height reduction and erosion control measures.

4.3.2 Line Series to Assess the Impact of WECs on H_s along the Coastline

To further evaluate the impact of WECs along the coastline, the MIKE21 linear data extraction tool was employed. Data was extracted for a line parallel to the coastline at position 316,000, focusing on the modified port configuration during a storm event. The exported data included three WEC location scenarios (north, front, south) and three arrangement scenarios (staggered 13 NE, linear 13 NE, staggered 11 SE). The objective was to determine which scenario led to a more significant wave height (H_s) reduction in a line with identical water depth. The results are depicted in Figure 13 for three cases of devices installed to the (a) north, (b) front, and (c) south of the port. In these diagrams, the x-axis illustrates the distance from the southernmost point on the investigated line along the coast, and the y-axis corresponds to significant wave height values. It is evident from the diagrams that all three structure arrangements had a notable impact on wave height compared to the no-structure case.

(a)

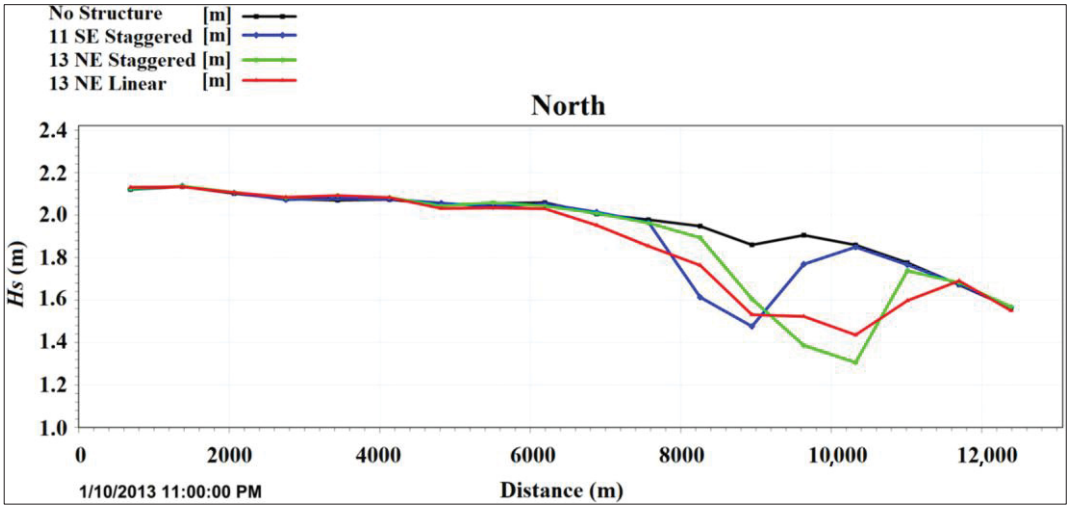

(b)

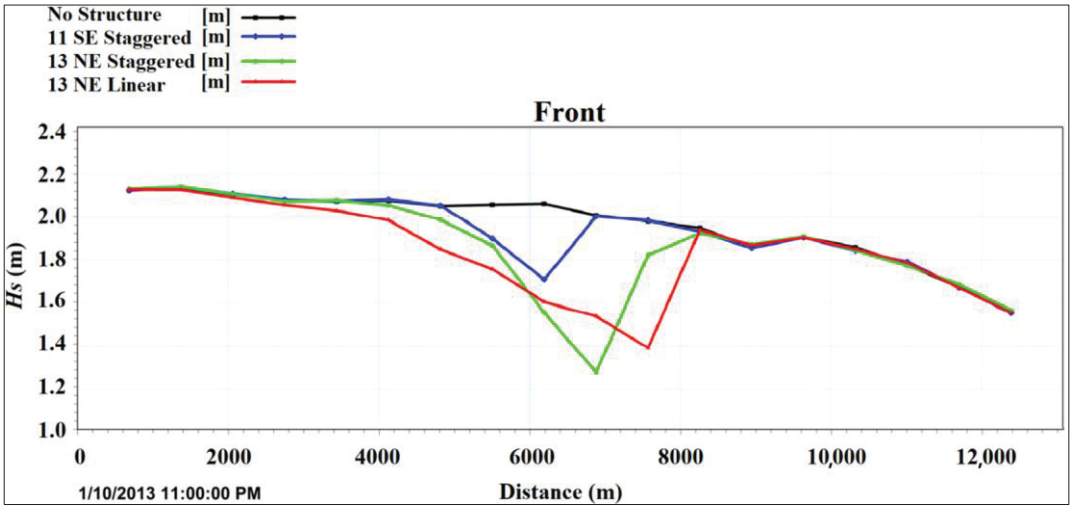

(c)

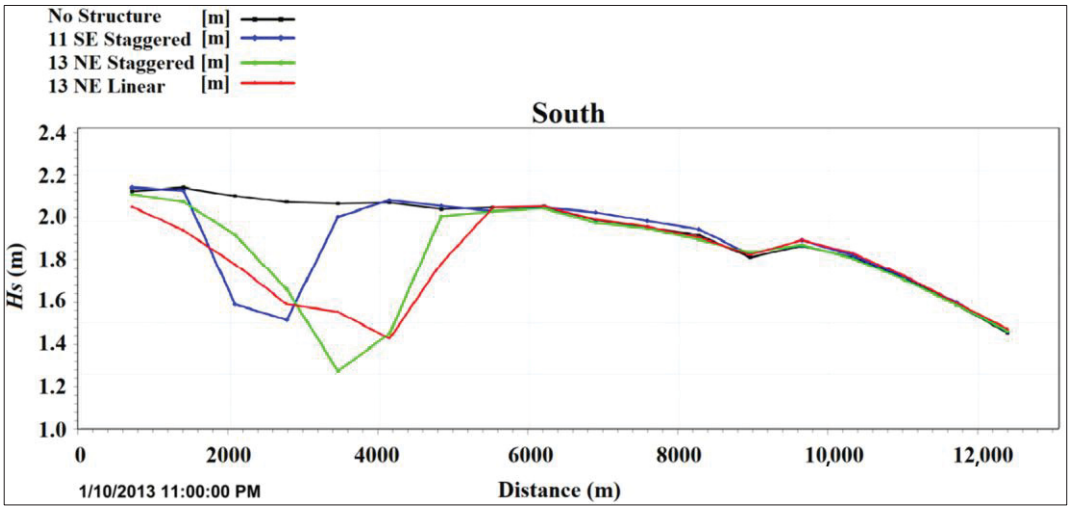

Figure 4.13 Line series of wave height for a line parallel to the coastline during a storm event for WECs located to the (a) north, (b) front, and (c) south of the port

Furthermore, the staggered arrangement in the 13 NE direction showed the highest decrease in significant wave height by 29.74%, 36.26%, and 31.86% when installed to the north, front, and south of the port, respectively. This proves that the maximum wave height reduction is observed when the WEC farm is in front of the port and staggered with the arrangement of 13 NE. The values of maximum wave height reduction for 13 NE linear are 22.75%, 29.62%, and 25.76% for north, front, and south of the port installation locations, respectively, and 26%, 17.1%, and 31.92% for 11 staggered de-vices to the north, front, and south of the port, respectively.

The data indicate that the 13 WECs with staggered arrangement facing northeast achieves the highest decrease in significant wave height during a storm across all placements. Specifically, the front placement scenario shows the most significant reduction, with a decrease of 36.26%. Therefore, it can be concluded that the optimal configuration for reducing significant wave height is 13 NE staggered, particularly when installed in front of the port.

However, the 13 NE linear arrangement demonstrated a broader length of effect (Figure 4.13), indicating superior performance in mitigating wave height across a wider region. The linear arrangement of WECs impacted 41.52%, 47.88%, and 46.6% of the total length of the local model boundaries for the north, front, and south of the port placements, respectively. For the 13 staggered WECs, these percentages were 35.59%, 35.84%, and 27.11% for the north, front, and south scenarios, respectively. Finally, the reduction percentages for the 11 staggered devices were 22.88%, 17.79%, and 21.18% for north, front, and south, respectively. The percentages show that linear arrangements tend to cover a larger portion of the coastline compared to staggered configurations, indicating potentially greater effectiveness in influencing wave heights and mitigating coastal erosion over a broader area. The highest percentage (47.88% length of the local model boundary), indicating the most significant coastline coverage, is observed for the front of port placement scenario. Therefore, it can be considered the optimum choice for the linear arrangement to maximize the coverage of coastline protection by WECs. These results suggest that the choice of WEC farm arrangement and location plays a significant role in determining the extent of the coastline affected.

4.3.3 Effect of Different Arrangements, Orientation, and Location on Aerial Wave Height Reduction

The significant wave height contours under various scenarios of WECs placement, orientation, and arrangement are depicted in Figure 4.14 to Figure 4.22. As mentioned in the pre-ceding section, the linear arrangement of WECs exhibits a broader impact on wave height across the area, whereas 13 staggered WECs oriented towards the northeast demonstrate more significant reductions in wave height values within a smaller spatial extent. Additionally, the configuration involving 11 WECs facing southeast has a marginal effect on wave height reduction. Furthermore, the southeast orientation of these WECs away from the dominant wave direction reduces their efficacy in power generation and wave capture.

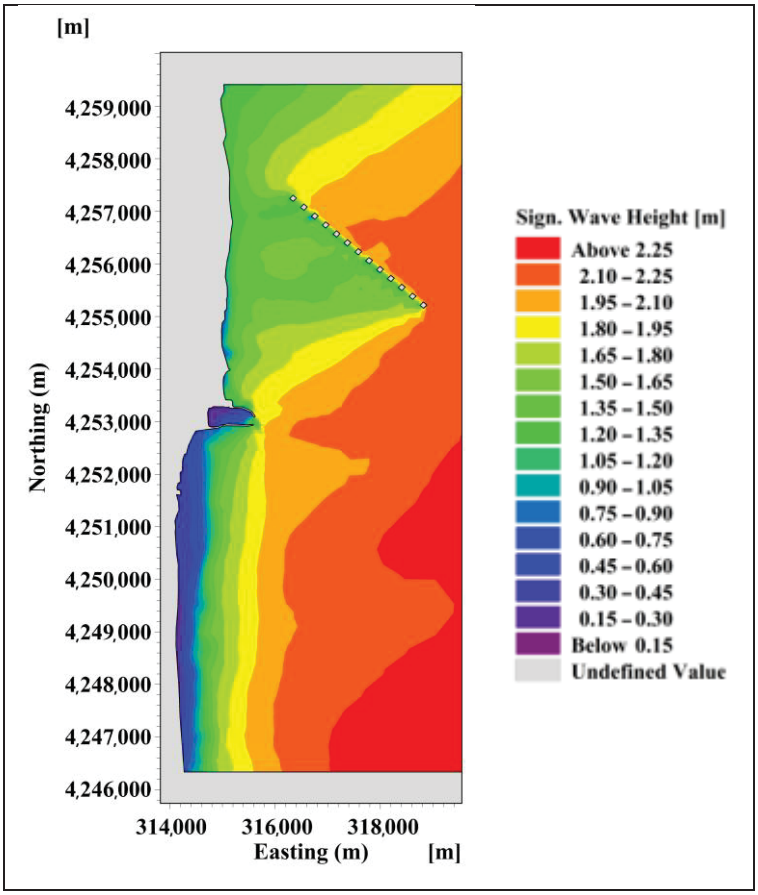

Figure 4.14 Wave height diagram in the presence of 13 linear wave energy devices on north of the port

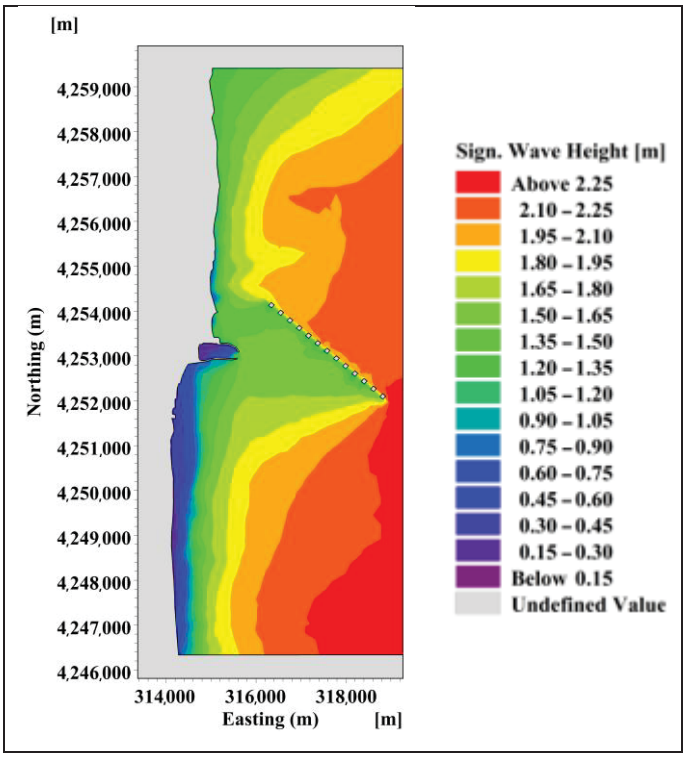

Figure 4.15 Wave height diagram in the presence of 13 linear wave energy devices in front of the port

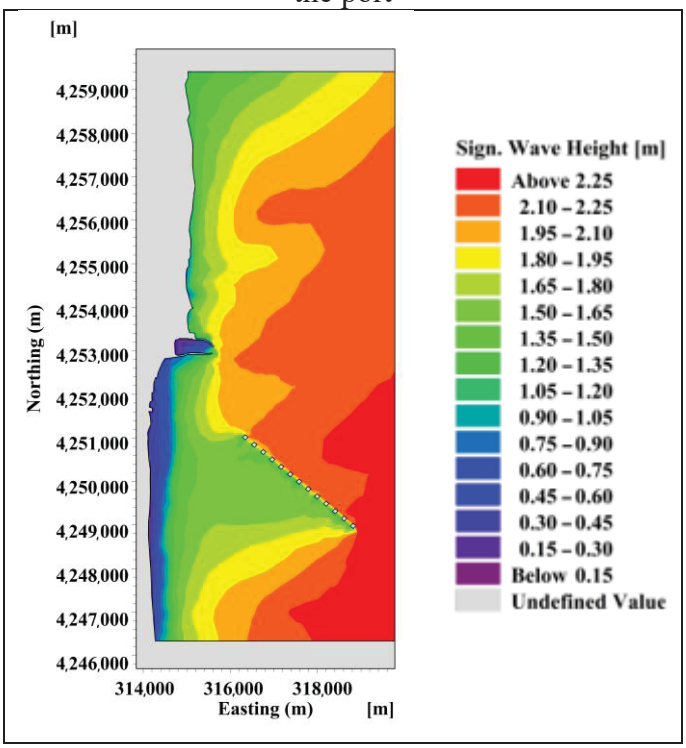

Figure 4.16 Wave height diagram in the presence of 13 linear wave energy devices on south of the port

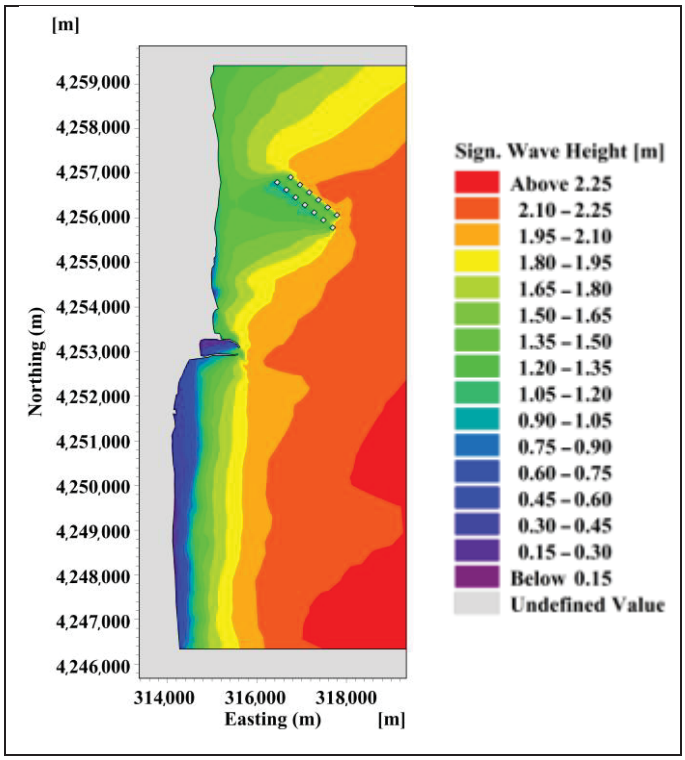

Figure 4.17 Wave height diagram in the presence of 13 staggered wave energy devices on north of the port

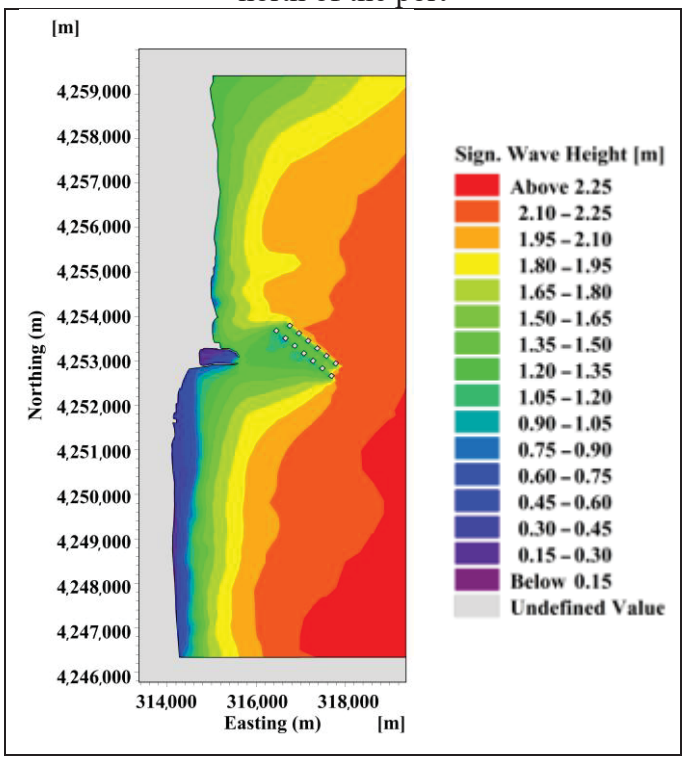

Figure 4.18 Wave height diagram in the presence of 13 staggered wave energy devices in front of the port

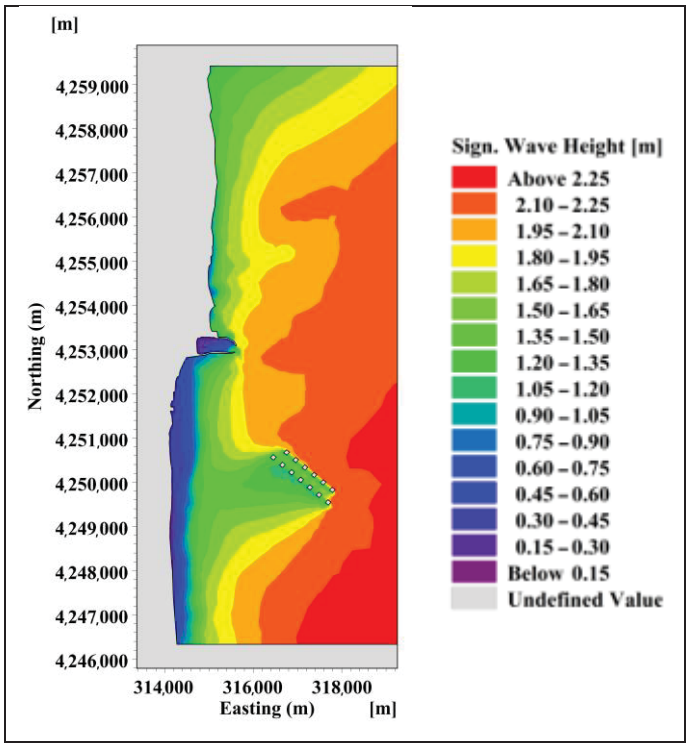

Figure 4.19 Wave height diagram in the presence of 13 staggered wave energy devices on south of the port

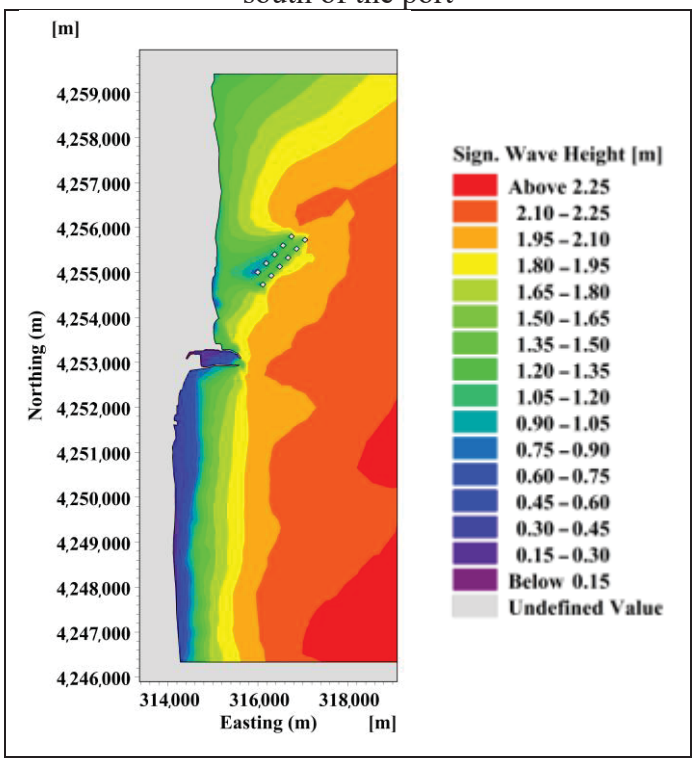

Figure 4.20 Wave height diagram in the presence of 11 staggered wave energy devices on north of the port

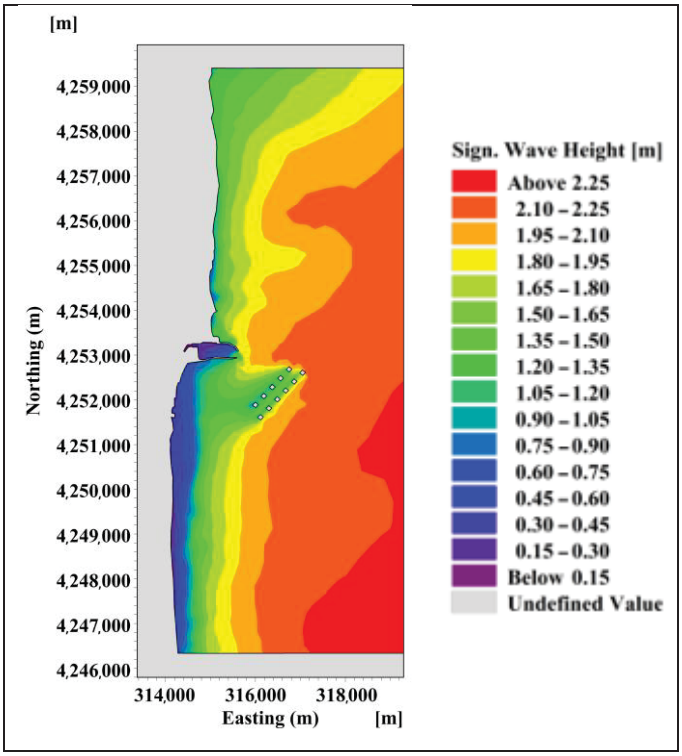

Figure 4.21 Wave height diagram in the presence of 11 staggered wave energy devices in front of the port

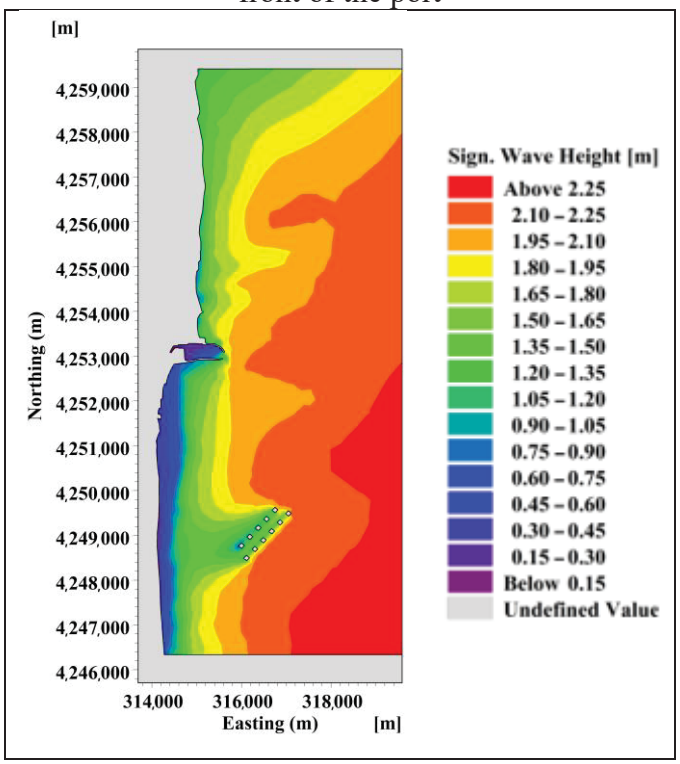

Figure 4.22 Wave height diagram in the presence of 11 staggered wave energy devices on south of the port

Selecting the most suitable wave farm arrangement and location is crucial for each region's specific needs and the prevailing erosion patterns. In this case, both linear and staggered arrangements facing northeast have demonstrated acceptable efficiency in wave height reduction and erosion mitigation. Moreover, more significant wave height reduction by these structures implies increased energy dissipation, indicating higher potential for power generation, especially evident in this study for the 13 staggered devices facing northeast.

4.3.4 The Impact of Harbor Layout on Near Port Current Speed and Sedimentation Pattern

The flow model (FM) and sand transport model (ST) were run for the year of 2013 using MIKE21 simulations to see the impact of placement of WECs in front of the port and port layout on sedimentation and flow pattern near the port entrance. The sediment transport model (ST) uses empirical equations to simulate sediment movement based on factors like grain size, sediment concentration, and flow velocity. On the other hand, the flow model (FM) relies on shallow water equations (Saint-Venant equations) to simulate water flow dynamics, considering factors such as water depth, flow velocity, and external forces like gravity and friction. As evident from the annual bed level change diagrams (Figure 4.23), there is a noticeable sediment deposition at the port entrance, which can have severe implications for commuting and the possibility of the port being closed due to accumulated sediments (Gao et al., 2021; Gao et al., 2024). As the first step to preventing the port's closure and reducing sedimentation, wave energy converters were proposed and modeled in simulations. Results showed that wave energy devices do not provide a complete solution to eliminate the necessity for dredging and may even make the sediment accumulation issue more severe (Figure 4.24).

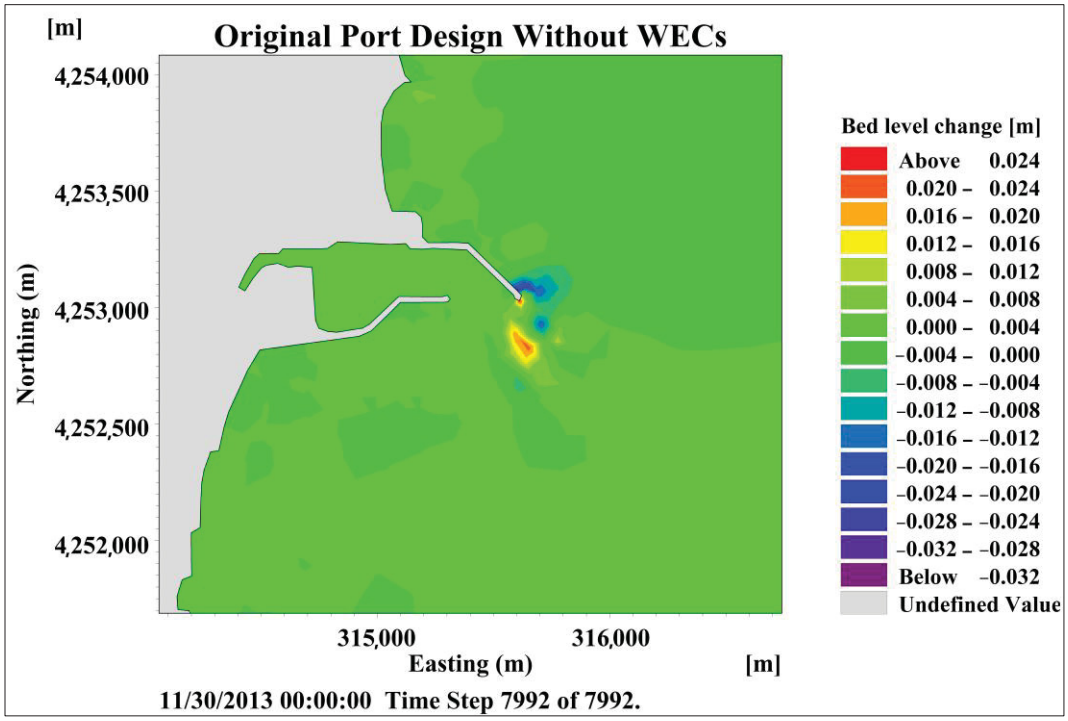

Figure 4.23 Sediment accumulation in the original port design

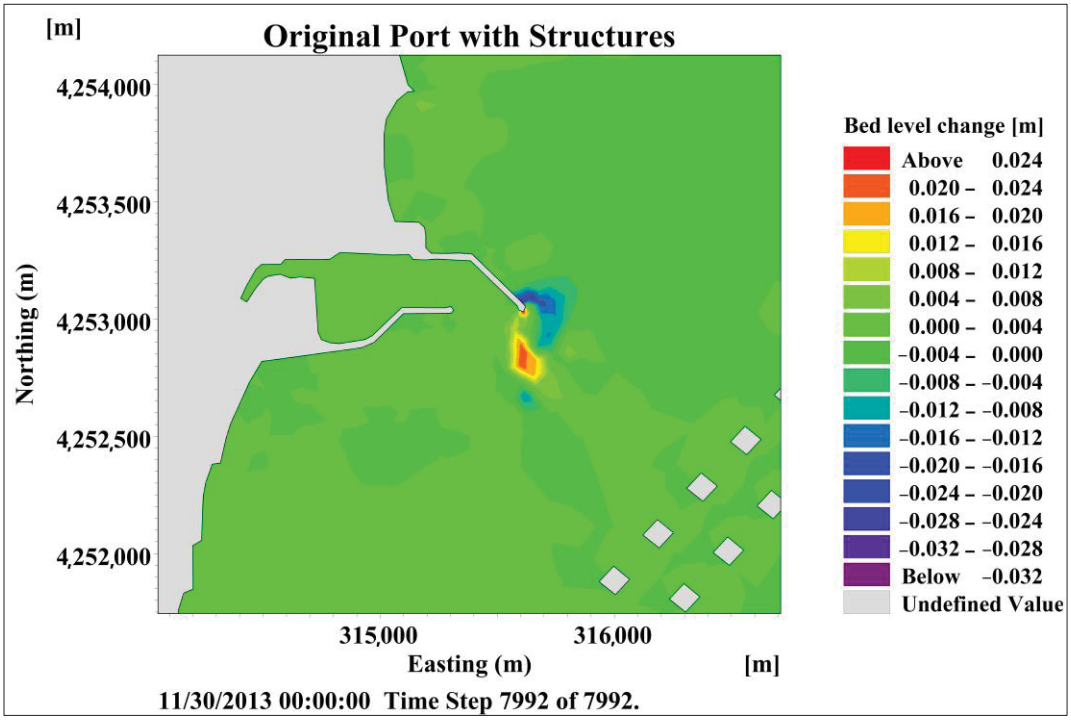

Figure 4.24 Sediment accumulation in the original port design in the presence of WECs in front of the port

Proposing a new design for the harbor was suggested to solve this problem. This modified design incorporates two curved arms that guide the high-velocity currents away from the harbor entrance. The intended outcome of this layout is a reduction in the formation of vortices and circular flows, which have been identified as the main reason behind the accumulation of sediment at the harbor entrance in the original layout of the port (Figure 4.25). Owing to this high-velocity flow passing by the port entrance without rotatory flow (Figure 4.26), sediment particles do not linger long enough to settle near the harbor opening. Instead, they are transported towards the port's southern reaches (the dominant flow direction of the region is north to south). Thus, sediment deposits (which were formerly located near the port's entry) have shifted to its southern portions (Figure 4.27).

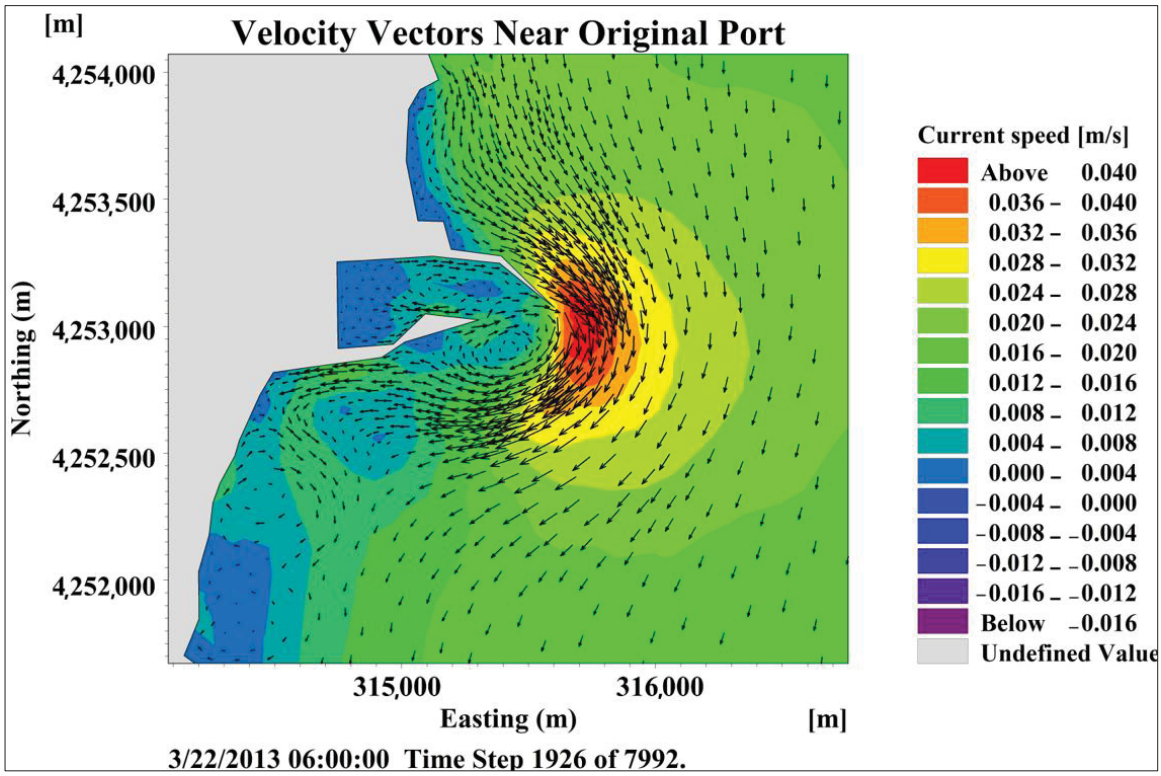

Figure 4.25 Velocity vectors and vortex formation near the original port layout

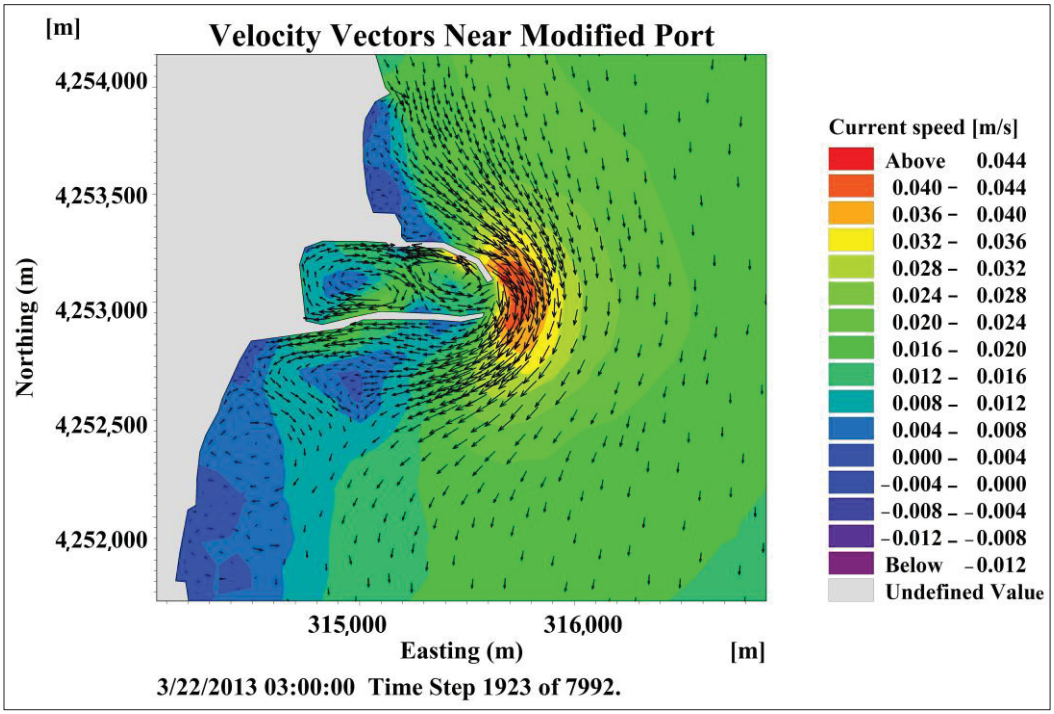

Figure 4.26 High-velocity flow passing by the port entrance of the modified port layout

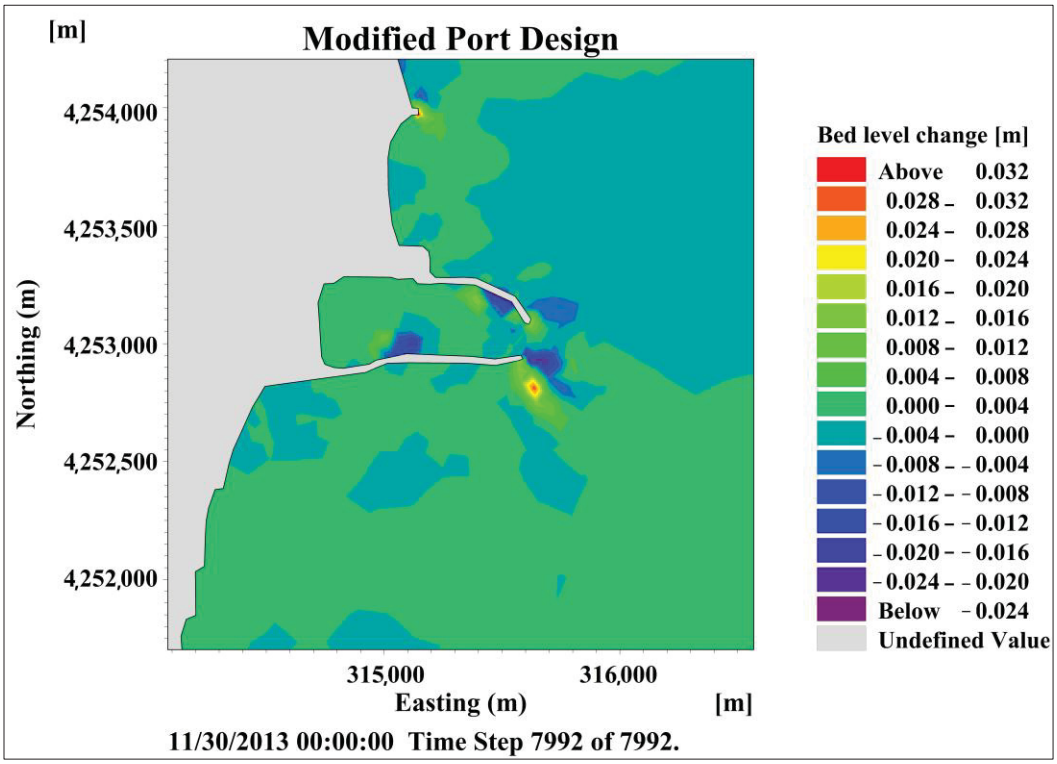

Figure 4.27 Annual bed level change south of the modified port layout

Furthermore, the rotatory flow contributes to higher bed shear stress (Moradi, Sajjadi, et al., 2022), thereby escalating erosion, especially notable in the southern regions of the original port layout. However, this rotatory flow has been eliminated in the modified port layout, reducing erosion in that part. These observations confirm that altering the flow dynamics can significantly impact sedimentation patterns, which in this case study results in a solution to the Astara Port entrance sediment accumulation problem and erosion issue. This can be utilized for ports with similar problems.

The sediment accumulation near the port in 2013 was analyzed using the bed level change output of the MIKE21 ST (Sand Transport) model (Figure 4.28). This analysis included three different WEC arrangements: 11 SE staggered, 13 NE staggered, and 13 NE linear. By the end of the year, the sediment accumulation values for these scenarios were 0.0358 m, 0.0943 m, and 0.1231 m, respectively. The sediment accumulation analysis near the port indicates that the 11 SE staggered arrangement demonstrated the lowest sediment accumulation at 0.0358 m, indicating its good potential in mitigating sedimentation. Conversely, the 13 NE linear arrangement exhibited the highest sediment accumulation of 0.1231 m.

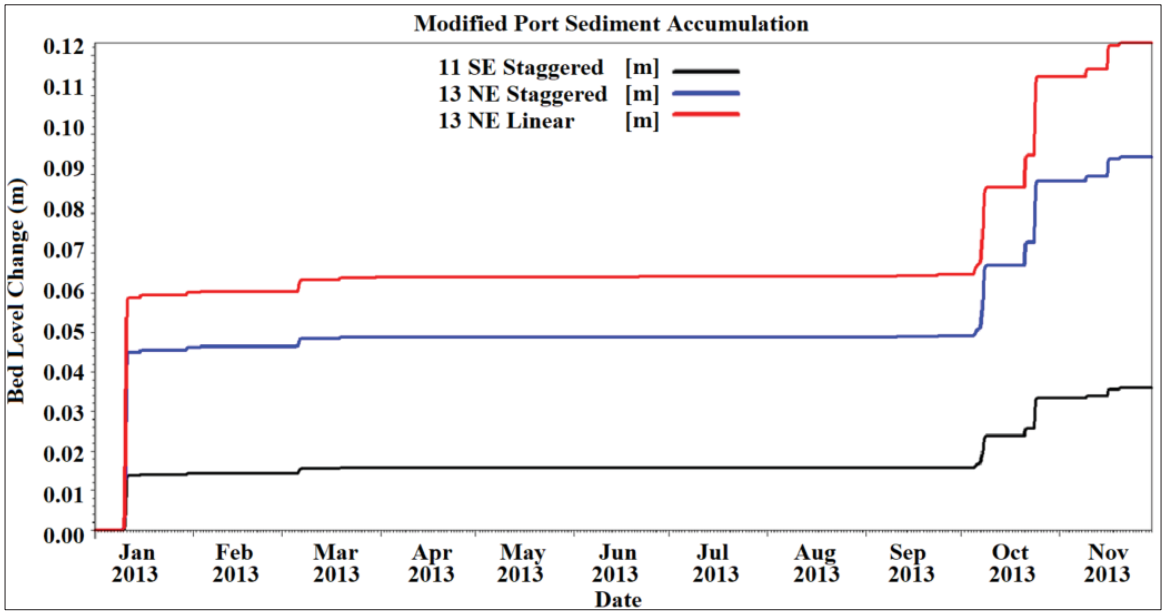

Figure 4.28 Comparison of the impact of different WEC arrangements on sediment accumulation downstream of the port

4.4 Discussion

Waves are significant sources of energy that deform beaches and marine structures, carrying sediments along the shoreline (through longshore sediment transport) and perpendicular to the shore (through onshore and offshore sediment transport). The main objective of this project is to achieve a stable pattern of how the waves operate around wave energy converters. The innovation of this study arises from examining the dual role of WECs in energy generation and coastal protection, comparing linear and staggered arrangements, analyzing WECs orientation effects, and proposing a novel port design for sedimentation management to move it away from the port entrance. Achieving the objectives of this study is feasible by recognizing the region's flow, wave, and wind pattern and studying the phenomena related to sea waves, such as wave height. These layouts were tested and simulated for both wave (SW) and flow (FM) models in 2013 and different scenarios.

The limitations of the MIKE21 2D model in capturing dynamic components highlight the need for future research to explore a 3D analysis of the flow field on a smaller scale. These studies need to aim to investigate how Wave Energy Converters (WECs), specifically Wave Dragon devices, influence flow and wave dynamics as they move within the water. This shift to 3D analysis aims to provide a more comprehensive understanding of the interactions between WECs and the flow field, ultimately shedding light on their impact on coastal erosion and energy production potential. The necessity for this becomes more evident as many existing studies overlook the dynamic behavior of the Wave Dragon device by treating it as a static object and neglecting the modeling of mooring lines.

4.5 Conclusions

In studying the impact of WECs and port layout on flow hydrodynamics, sediment dynamics, and wave climate, different scenarios, including various locations of wave farms, the number of WECs, and their arrangement and orientation, were investigated. The result of this study demonstrates significant reductions in wave height, particularly notable in the case of 13 staggered energy converters facing the dominant wave direction, resulting in a 23% to 25%

decrease in H_s values and effective erosion control. Moreover, among the configurations tested, the 13-staggered arrangement achieves the highest decrease in significant wave height during a storm event, especially evident in the front placement scenario with a reduction of 36.26%. This suggests that the optimal configuration for reducing wave height is the 13 NE staggered arrangement, particularly when positioned in front of the port. However, the linear arrangement of Wave Energy Converters (WECs) offers better coastline protection coverage due to its extended impact length during storm events (47.88% of the length of the local model boundary).

These conclusions can be practically applied to real-world projects, especially those focused on coastal protection. The findings suggest that the 13 NE staggered arrangement of WECs, particularly when positioned in front of a port, is the most effective scenario in reducing wave height during storm events. The linear arrangement of WECs, despite providing less localized wave height reduction, offers broader coverage for coastline protection during adverse weather conditions. Integrating linear WEC arrangements into coastal protection projects can enhance overall coastal resilience by extending protection along a significant portion of the coastline.
Finally, the study proposes a new port design to address sediment accumulation, directing high-velocity flow away from the port entrance, effectively mitigating sediment deposition near the harbor opening. This redirection of flow results in sediment deposits shifting to the southern portions of the port, contributing to overall sedimentation control measures and improved port functionality.

CHAPITRE 5

ANALYZING WAVE DRAGON UNDER DIFFERENT WAVE HEIGHTS USING FLOW-3D: A COMPUTATIONAL FLUID DYNAMICS APPROACH

M. Moradi [a] and A. Ilinca [b]

[a, b] Department of Mechanical Engineering, École de Technologie Supérieure, 1100 Notre-Dame West, Montréal, Quebec, Canada, H3C 1K3

Paper published in *Water*[4], February 2025

Abstract

Wave energy is an increasingly attractive renewable energy source due to its potential and predictability. Various Wave Energy Converters (WECs) have been developed, including attenuators, overtopping devices, and point absorbers. The Wave Dragon, an overtopping device, is a floating structure anchored to the seabed with a mooring system. It uses two reflectors to guide incoming waves into a central reservoir, where the captured water flows through turbines to generate electricity. This study enhances the realism of Wave Dragon simulations by modeling it as a moving structure with moorings, addressing key gaps in prior research. Real-time wave data from the Caspian Sea, collected over a year, were used to develop a 3D model and analyze the device's performance under varying wave conditions. Four significant wave heights (H_s) of 1.5, 2.5, 3.5, and 4.5 m were tested. The results demonstrate that higher wave heights increase water flow through the turbines, leading to higher energy output, with monthly energy generation recorded as 16.03, 25.95, 31.45, and 56.5 MWh for the respective wave heights. The analysis also revealed that higher wave heights significantly increase pressure forces on the Wave Dragon, from 2.97×10^5 N at 1.5 m to 1.95×10^6 N at 4.5 m, representing a 6.5-fold increase. These findings underscore the potential

---

[4] Moradi, M. and Ilinca, A., 2025. Analyzing Wave Dragon Under Different Wave Heights Using Flow-3D: A Computational Fluid Dynamics Approach. *Water*, *17*(5), p.613.

of Wave Dragons to enhance renewable energy production while ensuring structural robustness in varying wave conditions.

Keywords: wave energy converters (WEC); CFD; FLOW-3D; renewable energy; significant wave height

5.1 Introduction

In today's world, there is an increasing need to harness energy from renewable and green sources that have a minimal long-term impact on our climate (Bilgen et al., 2004). Among these sources, the most significant and widely utilized are wind energy, solar energy, and hydro-energy, including a specific subcategory focused on harnessing the energy of seas and oceans, particularly from incoming waves (Darmawi et al., 2013). Wave energy has significant potential as a clean and renewable resource, playing a crucial role in diversifying energy sources and mitigating environmental impacts. While wave energy holds great potential as a renewable resource, its practical implementation still requires thorough analysis and in-depth research. This is crucial because setting up wave energy technologies in real-world environments can be both expensive and risky. This shows the necessity for ongoing research to ensure wave energy's effectiveness and reliability (López et al., 2013).

Wave energy converters (WECs) can be classified as point absorbers, attenuators, and overtopping devices. Each category has advantages and challenges, highlighting the importance of selecting the most suitable type based on wave conditions and deployment location (Soares et al., 2012). Point absorbers utilize the motion between the buoy and a reference point, such as a fixed structure or a submerged platform. The buoy's motion caused by waves drives a power take-off system, such as hydraulic pumps or generators, to produce electricity (Amini et al., 2022; Guo et al., 2022; N. Zhang et al., 2021; Zurkinden et al., 2014). Attenuators lie parallel to the direction of the incoming waves. They capture the energy of the waves by utilizing the relative motion be-tween the segments as the waves pass (Liao et al., 2023; Matamala et al., 2023; J. Wang et al., 2023; Yang et al., 2018). Overtopping

devices guide water over a ramp into a raised reservoir, and the stored water's potential energy is converted into electricity as it flows through turbines.

One of the overtopping devices that have recently gained attention is the Sea-Wave Slot-Cone Generator (SSG), designed for shoreline installation. It captures wave energy using multiple stacked reservoirs; as waves run up their sloped face, they overflow into these reservoirs positioned at various heights. The stored water is then channeled through turbines, generating electricity as it flows back to the sea. This multi-level design enables the SSG to effectively harness energy from waves of different intensities, maximizing its power generation potential (Vicinanza et al., 2012).

The Wave Dragon is another specific overtopping device that uses curved wings to funnel waves into a central reservoir. The water is then released through turbines to generate electricity (Bevilacqua & Zanuttigh, 2011; Di Lauro et al., 2020; Liu et al., 2017; Moradi, Chertouk, et al., 2022). Tedd & Peter Kofoed, 2009, studied the overtopping flow of the Wave Dragon prototype in real sea conditions. They aimed to address the lack of time series data on overtopping flows for such structures. By comparing experimental data from October 2006 with their models, they tested the accuracy of their simulations. Measurements from pressure transducers showed that their simulation effectively models the overtopping flow.

Kofoed et al., 2006, studied the Wave Dragon prototype, which has been operational in Nissum Bredning, Denmark, since May 2003 and was the world's first offshore WEC. The results showed that the prototype device could gather accurate data about how much power it produced and the environmental conditions it operated in. This information helps improve the design of the device and the efficiency of its power take-off system, which converts wave energy into electricity.

Eskilsson et al., 2015, used a (Volume of Fluid) VOF-based incompressible Euler/Navier-Stokes solver in OpenFOAM to simulate the Wave Dragon's overtopping

behavior. They simulated a complete sea state with different crest heights and regular waves under various conditions. The results aligned reasonably well with experimental data, though the simulations for irregular waves predicted a larger overtop-ping discharge than observed.

Ahmad et al., 2024, investigated the effects of the angles between Wave Dragon's guiding walls and wave heights on Wave Dragon's performance using FLOW-3D software. The results showed that higher wave heights and an optimal guiding wall angle of 80 degrees achieved the highest overtopping value. The simulation model showed a 15% difference from experimental observations; however, these results provide valuable insights for enhancing the performance of the Wave Dragon and other wave energy systems. Cao et al., 2024, refined the empirical models for floating overtopping wave energy converters, particularly the Wave Dragon model, by incorporating correction coefficients to account for limited draft, inclination angle, and low relative freeboard, thereby improving overtopping predictions.

In another study, Moradi & Ilinca, 2024 utilized experimental data on the wave and current velocity and their direction to calibrate a MIKE21 2D model for simulating waves and current conditions in the Caspian Sea. In this research, real-time wave characteristics from this previous study by Moradi & Ilinca, 2024, were incorporated to model the Wave Dragon using the FLOW-3D software.

The Wave Dragon is designed for offshore deployment, making it suitable for moderate to high-energy wave climates. Its overtopping wave energy capture mechanism enables large-scale power generation, making it a viable option for areas with low tidal ranges but strong waves. From an economic perspective, precise modeling of power output under varying wave conditions is crucial for assessing project feasibility and return on investment. Moreover, the Wave Dragon can contribute to coastal protection by dissipating wave energy, reducing erosion, and potentially serving as a dual-purpose infrastructure that combines renewable energy generation with shoreline defense. Many recent studies focus on wave-structure interactions using CFD (Mi et al., 2025; Song et al., 2025), but very few have specifically analyzed the Wave Dragon's performance as a dynamic object and with a mooring system to

model interactions between the device and wave forces. The omission of the dynamic nature of the Wave Dragon limits the under-standing of flow patterns, pressure distributions, and energy capture efficiency under realistic operating conditions. This research accurately represents the complex hydro-dynamic behavior near the Wave Dragon by incorporating moorings and allowing the structure to move. It offers valuable insights for optimizing its design and performance. Modeling the Wave Dragon with moorings and as a moving object is crucial to accurately represent the complex flow structures near the device, as these flow structures directly impact the device's performance and reliability. For instance, they influence the distribution of pressure forces and turbulence around the structure, which is critical for optimizing energy capture and minimizing structural fatigue. Understanding these dynamics ensures that the Wave Dragon operates efficiently under varying wave conditions and can withstand the mechanical stresses induced by high-energy waves.

Thus, the uniqueness and novelty of this study are justified as it investigates the performance of the Wave Dragon under varying wave heights while incorporating dynamic motion and mooring systems, thereby addressing gaps in existing research. Additionally, a new approach was implemented in this study by positioning history probes within the turbines to precisely measure the flow quantity passing through each turbine. This represents a significant innovation in calculating precise generated power compared to traditional measurement techniques, such as stationary sensors or external baffles that measure pressure differences before and after WECs and apply efficiency conversion factors, which often fail to capture dynamic flow characteristics in moving structures. Embedding history probes directly within the turbines provides re-al-time, high-resolution data on flow velocities, enabling a more accurate assessment of energy generation across varying wave heights.

The paper is structured as follows. Section 2 describes the materials and methods, detailing the setup of the FLOW-3D model and its application to simulate the Wave Dragon. Section 3 outlines the results of the analysis, including energy output, pressure forces, and flow dynamics. Section 4 discusses the broader implications of these findings for renewable energy

and Wave Dragon optimization. Finally, Section 5 concludes the study, summarizing key contributions and suggesting directions for future re-search.

5.2 Material and Methods

5.2.1 Model Assumptions

This study made several assumptions to ensure computational feasibility while maintaining accuracy in numerical simulations. First, the fluid was assumed to be Newtonian, meaning its viscosity remains constant under shear stress, which is a valid assumption for seawater in typical ocean conditions. Additionally, the flow was considered incompressible, as density variations due to pressure changes in water are negligible. The Volume of Fluid (VOF) method was employed for free surface tracking, assuming a sharp interface between air and water without phase mixing. Furthermore, wave conditions were modeled based on linear wave theory, which reasonably approximates moderate wave heights and regular wave patterns.

5.2.2 FLOW-3D Model

The FLOW-3D model, a three-dimensional CFD tool recognized as one of the most powerful in fluid dynamics, was utilized in this research. The meshing structure of this model consists of rectangular cubic cells. This type of meshing has its advantages, such as easy production of mesh blocks, proper order of mesh cells, and the possibility of doing calculations with lower system memory. Moreover, by incorporating the VOF (Volume of Fluid) method, which effectively distinguishes between different fluid regions like air and water to simulate complex wave behaviors and interactions with structures, alongside the FAVOR™ method, which smooths out zigzag direction changes by blocking fractional portions of grid cells, the rectangular meshing structure in FLOW-3D is made both practical and user-friendly for enhanced fluid dynamic simulations. Additionally, the VOF method makes FLOW-3D an advanced tool for free surface tracking, which is crucial for modeling wave energy devices where surface fluctuations directly impact performance and outcomes.

FLOW-3D offers a selection of five distinct turbulence models that can be applied based on the project's specific requirements. This flexibility allows simulations that accurately capture the fluid dynamics involved, whether in scenarios involving laminar flows or more chaotic turbulent conditions. This CFD model solves the Navier-Stokes equations which describe the conservation of mass, momentum, and energy for fluid flow. In this section, only the most important equations are presented (Flow-3D, 2023).

Mass Conservation Equation

The Mass Conservation Equation plays a vital role across multiple engineering disciplines, such as hydraulic systems, aerodynamics, and environmental engineering, by ensuring the conservation of mass during fluid flow simulations and analyses. The equation of mass conservation is as follows:

$$\frac{\partial u}{\partial x}+\frac{\partial v}{\partial y}+\frac{\partial w}{\partial z}=0 \tag{5.1}$$

where the variables u, v, and w represent the velocity components of the fluid flow in x, y, and z directions (Flow-3D, 2023).

Momentum Conservation Equation

The Momentum Conservation Equation addresses the forces exerted on a fluid system, guaranteeing that momentum remains conserved during interactions between the fluid and solid boundaries, as well as within the fluid itself. Momentum (Navier-Stokes) equations are as follows:

$$\rho\left(\frac{\partial u}{\partial t}+u\frac{\partial u}{\partial x}+v\frac{\partial u}{\partial y}+w\frac{\partial u}{\partial z}\right)=-\frac{\partial p}{\partial x}+\mu\left(\frac{\partial^2 u}{\partial x^2}+\frac{\partial^2 u}{\partial y^2}+\frac{\partial^2 u}{\partial z^2}\right)+\rho f_x \tag{5.2}$$

$$\rho\left(\frac{\partial v}{\partial t}+u\frac{\partial v}{\partial x}+v\frac{\partial v}{\partial y}+w\frac{\partial v}{\partial z}\right)=-\frac{\partial p}{\partial y}+\mu\left(\frac{\partial^2 v}{\partial x^2}+\frac{\partial^2 v}{\partial y^2}+\frac{\partial^2 v}{\partial z^2}\right)+\rho f_y \tag{5.3}$$

$$\rho\left(\frac{\partial w}{\partial t}+u\frac{\partial w}{\partial x}+v\frac{\partial w}{\partial y}+w\frac{\partial w}{\partial z}\right)=-\frac{\partial p}{\partial z}+\mu\left(\frac{\partial^2 w}{\partial x^2}+\frac{\partial^2 w}{\partial y^2}+\frac{\partial^2 w}{\partial z^2}\right)+\rho f_z \quad (5.4)$$

In these equations, p is pressure, ρ is density, μ is dynamic viscosity, (u, v, w) are velocity components in three coordinate directions, and (f_x, f_y, f_z) are viscosity accelerations (Flow-3D, 2023).

5.3 Mesh Block and Boundary Conditions

In the present study, the solution domain meshing was critical due to the simultaneous motion of fluid and WEC. The mesh convergence analysis began with a coarse mesh to capture the overall flow features. Smaller mesh sizes were then tested to enhance the model's accuracy. With each reduction in mesh size, the simulation results were compared against the water surface elevation of the corresponding theoretical waves, considering different wave heights, periods, and wave types. For a specific mesh size, further reduction in mesh size led to negligible changes in the results while significantly increasing simulation time. The final mesh size of 1m was selected, balancing accurate results with computational efficiency.

To enhance the accuracy of the calculations, two rectangular mesh blocks were generated: a mesh that defined the overall calculation domain with a basic mesh size of 1m and a finer mesh nested within the primary grid and placed near the water sur-face. This area experiences significant water fluctuations and complex interactions between the waves and the WEC, making a finer resolution essential for capturing the flow dynamics accurately. The mesh size ratio of 1:2, with the basic mesh having a cell size of 1m and the finer mesh having a cell size of 0.5m, demonstrated the highest agreement with wave theory diagrams (Figure 5.1). Moreover, a finer ratio of 1:4 (1m base, 0.25m fine mesh) was also tested; however, this configuration significantly increased computational time without notable accuracy improvements. A constant mesh size of 1m was tested as well. The results for these configurations were not reported, as the results for the 1:4 mesh ratio were practically similar to the ones of the selected mesh. The results for the constant mesh size of 1m did not show acceptable similarity to wave theory diagrams, leading to their early termination.

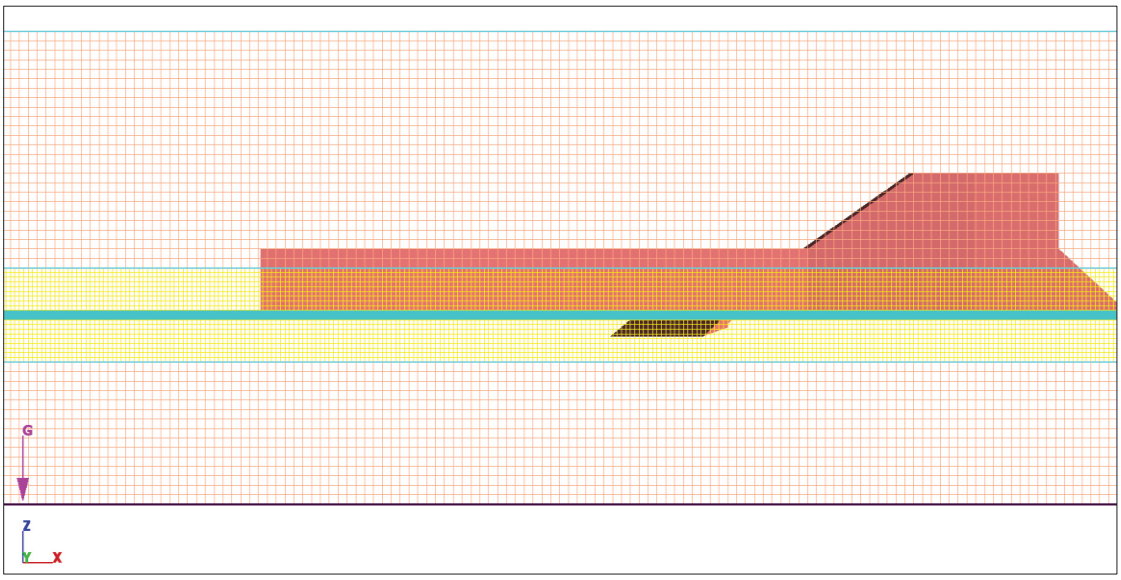

Figure 5.1 Side view of a main mesh block (1 m cell size, red) and a nested fine mesh block (0.5 m cell size, yellow) near the water surface

Figure 5.2 shows a rendered view of the solid component in FLOW-3D, which helps visualize whether the meshing structure is accurately modeling the details. As seen in this figure, there is acceptable accuracy, and the details are well-represented, demonstrating the effectiveness of the mesh configuration.

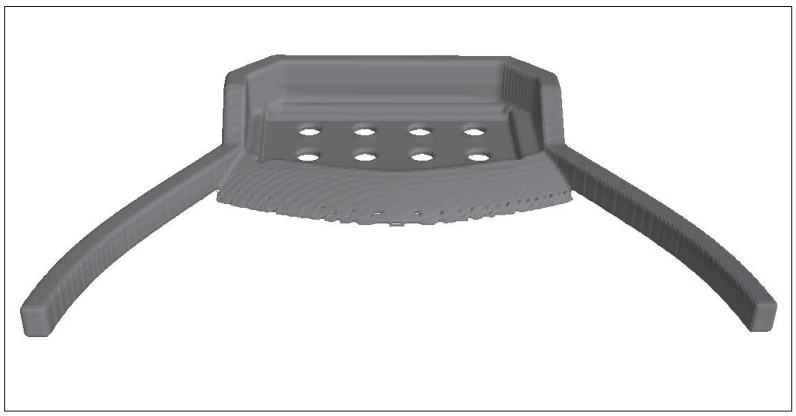

Figure 5.2 Render view of the Wave Dragon, showing the accuracy of the model

In Figure 5.3, the abbreviations WV, S, and O represent wave values, symmetry, and outflow boundary conditions, respectively. We use wave values boundary conditions on the WV boundary. The wave characteristics were defined with significant wave heights (H_s) of 1.5, 2.5, 3.5, and 4.5 m, a wave period of 8.9 s, and a mean flow depth of 20 m. Stokes waves were modeled using Fenton's 5th-order theory, chosen based on a wave theory diagram. A 35 m wave-absorbing layer was applied at the output boundary (identified with "O") to minimize wave reflections and ensure accurate flow modeling near the Wave Dragon. A symmetry boundary condition (face "S" located on the left and right-hand sides, as well as on the upper and lower sides of the domain) was used to mirror physical and flow properties, reducing computational effort while maintaining accuracy. The RNG (k-ε) turbulence model was employed to simulate turbulent flow and capture this study's complex fluid dynamics behavior. As the k-ω model is more suitable for boundary-layer flows and low-Reynolds-number regions, and Large Eddy Simulation (LES) is computationally expensive, requiring significantly finer meshes and longer simulation times, the RNG (k-ε) model was selected given the need for multiple simulations to assess different wave heights and configurations and due to its balance between accuracy and computational efficiency.

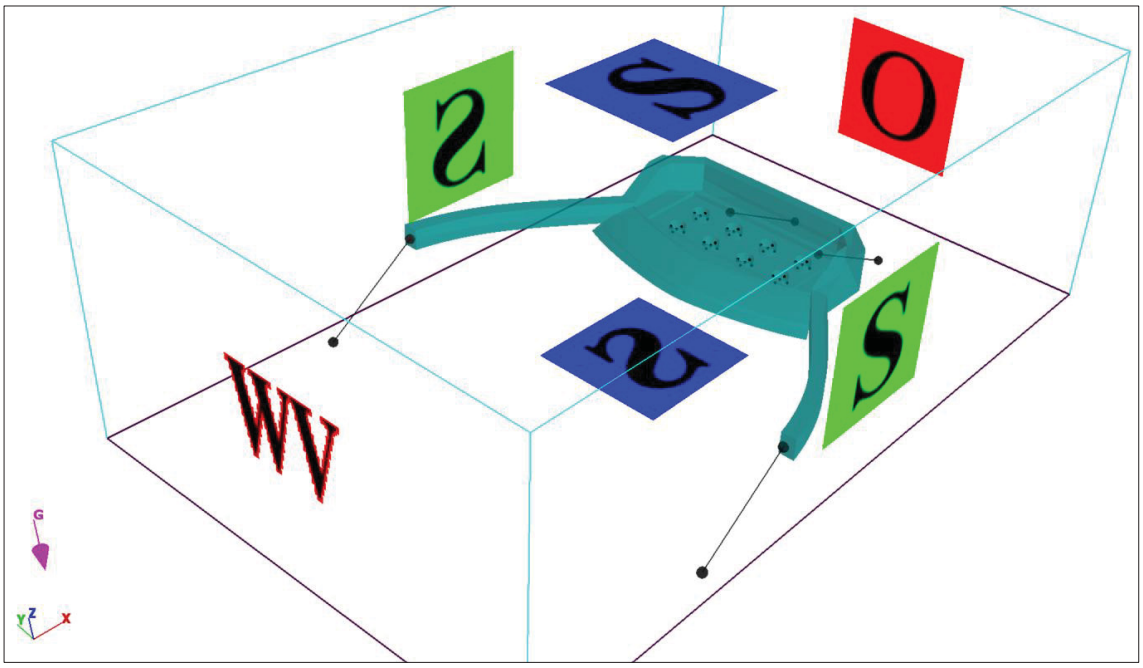

Figure 5.3 Defined boundary conditions, history probes, and mooring lines

5.4 Studied Waves

Identifying the wave height at which the WEC operates at peak efficiency is one of the goals of this study. This understanding can aid in optimizing the design and deployment of Wave Dragons, ensuring maximum energy capture under varying sea states. The wave data for this research is derived from a previous study that modeled the wave and current conditions of the Caspian Sea using the MIKE 21 software, validated with wave and current experimental data of one year data recorded in two buoy points in depth of 10m and 15m. The real-time wave data with wave heights of 1.5, 2.5, 3.5, and 4.5 m, and a wave period of 8.9 seconds were selected for analysis. The flow depth was maintained at a constant 20 meters, as water depths below this threshold do not significantly affect the flow regime within the study domain.

Table 5.1 below presents four representative waves from the MIKE 21 model results that have happened in the Caspian Sea in different seasons, characterized by their wave periods and significant wave heights (Moradi & Ilinca, 2024). The selected wave conditions provide realistic data exported from a previous study that used real-time wave and flow measurements. These waves actually occurred in the Caspian Sea, ensuring that the simulations reflect real sea conditions. Theoretical analyses of the waves were carried out, and wave verification diagrams were generated to ensure the simulated waves have an acceptable correlation with wave theory. To this purpose, the wavelength (L) is determined using the dispersion relation below:

$$L = \frac{gT^2}{2\pi} \tanh\left(\frac{2\pi d}{L}\right) \tag{5.5}$$

where g is the gravitational acceleration (9.81 m/s²), T is the wave period, and d is the water depth. Solving this iteratively for a depth of 20 meters and a period of 8.9 seconds, the wavelength was calculated to be 103.58 meters.

Table 5.1 Different wave scenarios studied

H_s (m)	T (s)	L (m)	d (m)
1.5	8.9	103.58	20
2.5	8.9	103.58	20
3.5	8.9	103.58	20
4.5	8.9	103.58	20

Based on these values, the wave was classified as an intermediate water wave, making Stokes' 5th-order theory the appropriate model for accurately simulating and predicting the wave's characteristics. In Figure 5.4, Figure 5.5, Figure 5.6, and Figure 5.7, the wave theory diagrams derived from Stokes' 5th-order theory for intermediate waves are compared with the FLOW-3D simulation results, focusing on wave features such as wave height and water surface elevation. The diagrams were plotted for at least ten consecutive waves. The results demonstrate acceptable accuracy in modeling wave periods, as well as wave crests and troughs. This consistency ensures that key wave characteristics are effectively captured in the simulations.

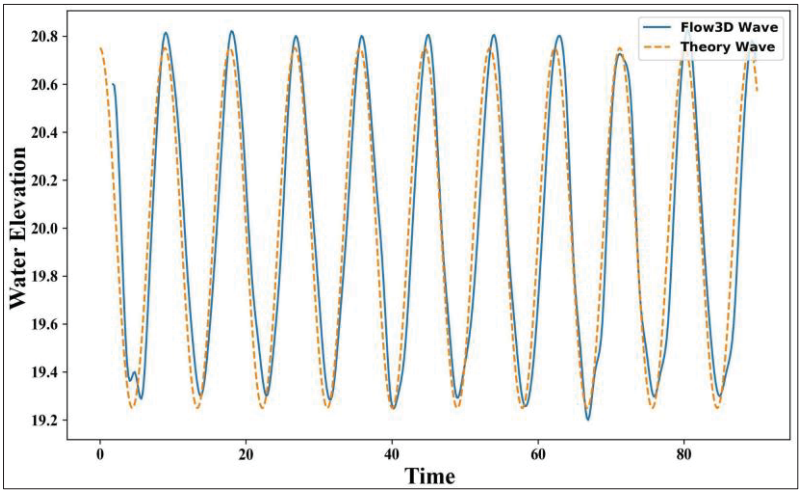

Figure 5.4 Wave theory and simulated wave diagram for H_s = 1.5 m

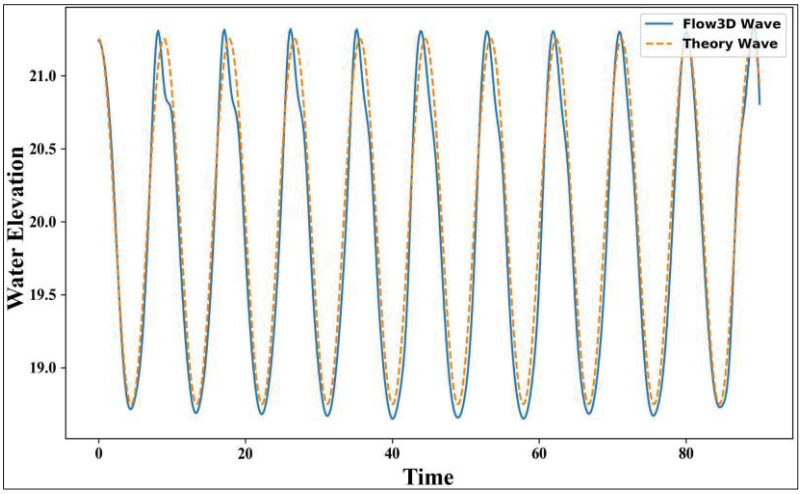

Figure 5.5 Wave theory and simulated wave diagram for H_s = 2.5 m

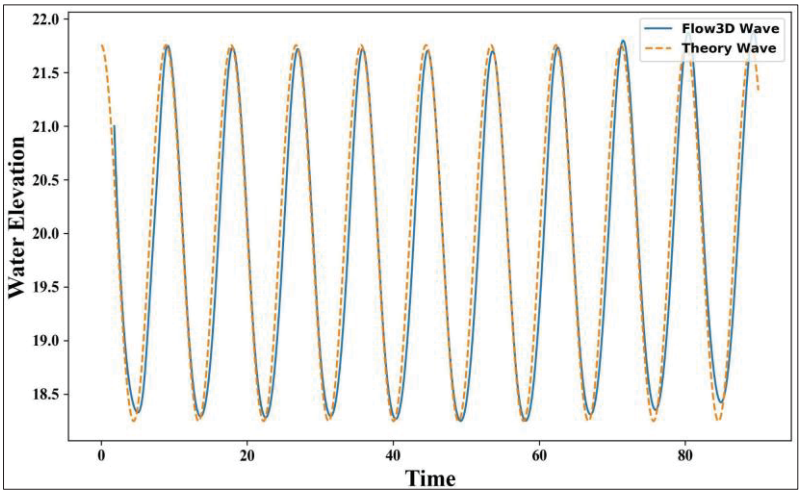

Figure 5.6 Wave theory and simulated wave diagram for H_s = 3.5 m

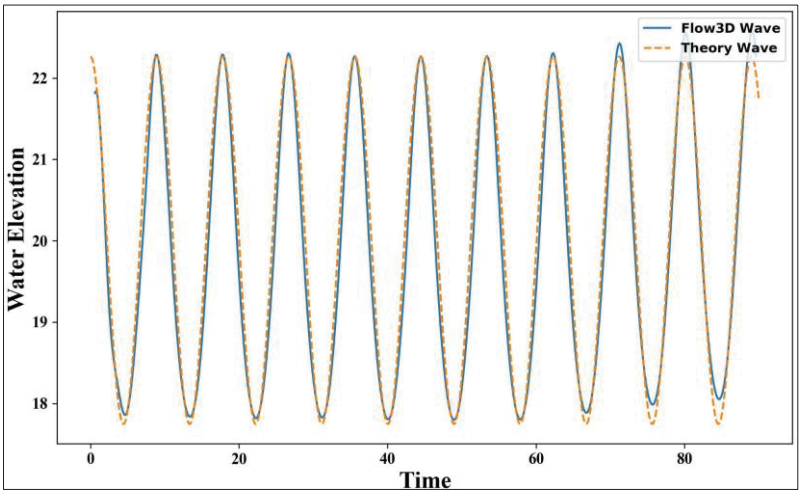

Figure 5.7 Wave theory and simulated wave diagram for H_s = 4.5 m

5.4.1 Statistical Analysis of Waves

A detailed statistical analysis of simulated waves further explores the accuracy of the simulations, providing deeper insights into the performance of the models. Table 5.2 compares theoretical wave heights with simulated wave heights for significant wave heights of 4.5, 3.5, 2.5, and 1.5 m. The comparisons are made by averaging the first 5, 8, and 10 simulated waves, respectively. The simulation results for H_s = 4.5 m show that the average wave height for the first five waves is 4.39 m, with an RMSE (Root Mean Square Error) of 0.129 m and an NRMSE (Normalized RMSE) of 2.87%.

For H_s = 3.5 m, averaging the first five waves yields an average wave height of 3.38 m, with an RMSE of 0.126 m and an NRMSE of 3.59%. For H_s = 2.5 m, the average wave height for the first five waves is 2.61 m, with an RMSE of 0.109 m and an NRMSE of 4.35%. As the data show, the accuracy of the simulated waves improves when compared to theoretical values for smaller wave heights.

The lowest errors occur at H_s = 1.5 m, where the average wave height for the first five waves is 1.50 m, with an RMSE of 0.0006 m and an NRMSE of 0.04%. This trend highlights that while the simulation closely aligns with theoretical wave values at lower heights, there is a noticeable deviation as wave height increases. Overall, based on the results, it is evident that there is good accuracy in simulating the wave approaching the Wave Dragon.

Table 5.2 Accuracy of simulated waves

H_s (m)	Averaged Waves	Average Simulated H_s (m)	RMSE (m)	NRMSE (%)
4.5	First 5 Waves	4.39	0.129	2.87
4.5	First 8 Waves	4.39	0.126	2.78
4.5	First 10 Waves	4.38	0.137	3.03
3.5	First 5 Waves	3.38	0.124	3.56
3.5	First 8 Waves	3.39	0.117	3.33
3.5	First 10 Waves	3.38	0.125	3.57
2.5	First 5 Waves	2.61	0.109	4.35
2.5	First 8 Waves	2.62	0.118	4.70
2.5	First 10 Waves	2.61	0.111	4.42
1.5	First 5 Waves	1.50	0.0006	0.0399
1.5	First 8 Waves	1.51	0.0006	0.0399
1.5	First 10 Waves	1.50	0.0006	0.0399

5.5 Flow Structure and Velocity Contours in the X-Z Plane

The vertical and horizontal components of velocity are used to compute two-dimensional velocity vectors in the X-Z plane, representing the flow dynamics within a vertical slice of the domain (Figure 5.8). Additionally, these components have been employed to generate contours of velocity magnitude for the slice, providing a clear visualization of the flow field in terms of speed and direction.

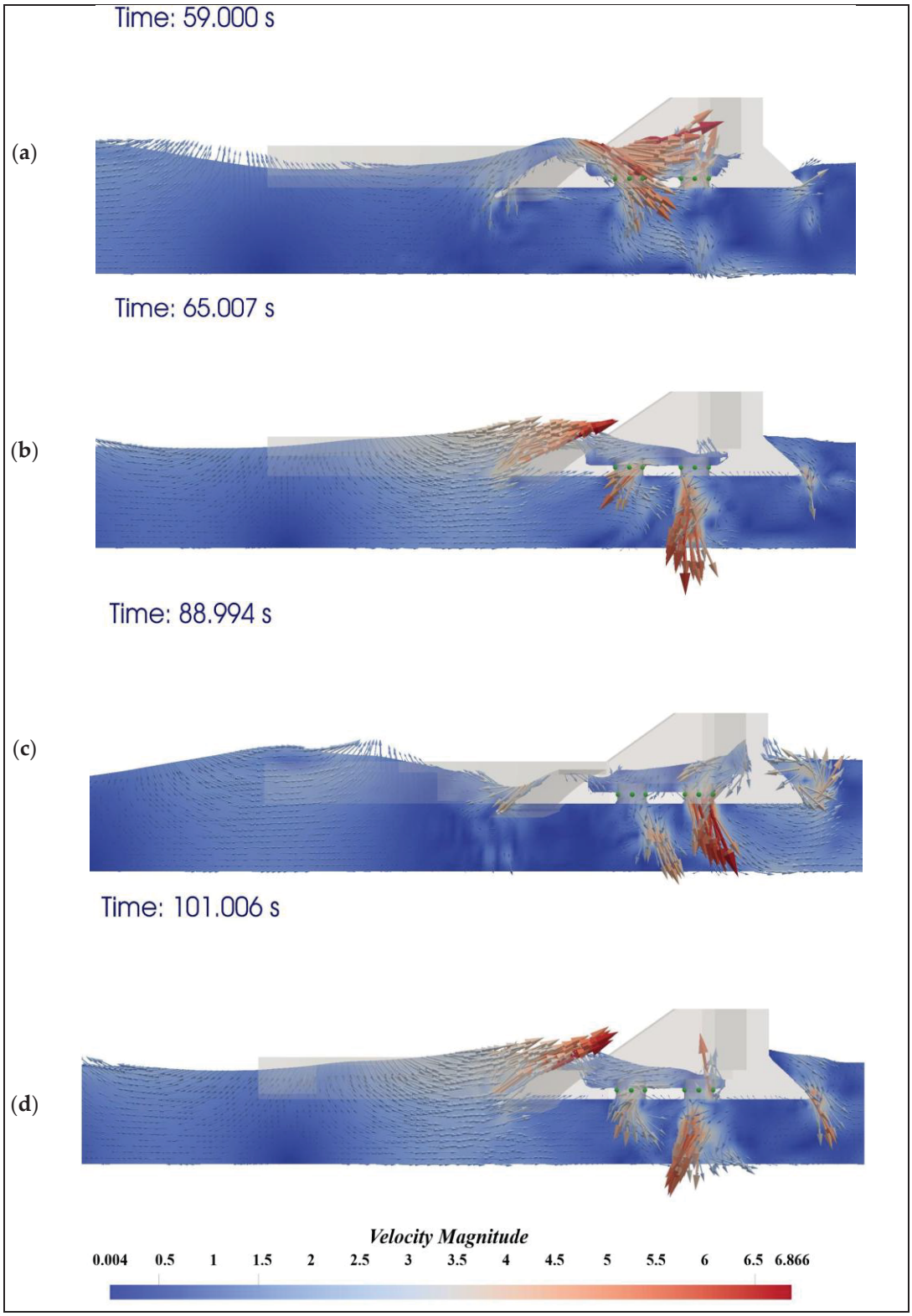

Figure 5.8 Flow structure and velocity contours at H_s = 4.5 m for time steps of (a) 59 s, (b) 65 s, (c) 88.99 s, and (d) 101 s

The velocity magnitude contours in the X-Z plane reveal significant energy concentration near the structure, with peak velocities of up to 6.8 m/s. The interaction between the wave crest and the structure results in strong flow acceleration and turbulence, particularly near the edges of the WEC, where flow separation and vortex formation occur. The flow becomes highly complex and chaotic near the structure when the waves hit, and the water enters the reservoir. Flow separation occurs when the flow interacts with the WEC, leading to increased pressure drag due to the pressure difference between the front and back of the structure. This drag-force opposes the WEC's motion, often causing uncontrolled oscillations that reduce energy capture efficiency.

Additionally, the energy that could be harnessed is instead lost to overcoming drag. By minimizing flow separation through streamlined and optimized designs or flow control techniques, pressure drag can be reduced, leading to greater stability and improved energy conversion efficiency. The key objective is to control motion, reduce drag, and maximize energy extraction. On the other hand, vortex formation downstream of the structure can impact WEC performance by creating unsteady flow conditions, leading to efficiency losses. Additionally, in WEC arrays, vortices from one device can interfere with neighboring units, further reducing overall system performance. To mitigate these effects, the spacing between devices should be carefully examined. Another notable observation is that the further back turbines experience higher flow velocities passing through them as they are positioned beyond the ramp. This allows for greater flow through these turbines, potentially leading to higher energy output, which will be discussed in detail in the following sections.

5.6 Pressure on the WEC

The analysis of pressure values applied to the WEC reveals a significant increase in pressure corresponding to higher wave heights, with average pressures measured at 2.97×10^5, 5.49×10^5, 6.65×10^5, and 1.95×10^6 N for wave heights of 1.5, 2.5, 3.5, and 4.5m, respectively. This trend indicates that as wave height increases, the pressure exerted on the WEC also rises, suggesting a non-linear relationship commonly seen in fluid dynamics. This

information is crucial for optimizing the design and operation of WECs, as higher pressures can lead to greater energy generation potential, underscoring the need for robust design considerations to handle maximum pressure scenarios effectively (Figure 5.9).

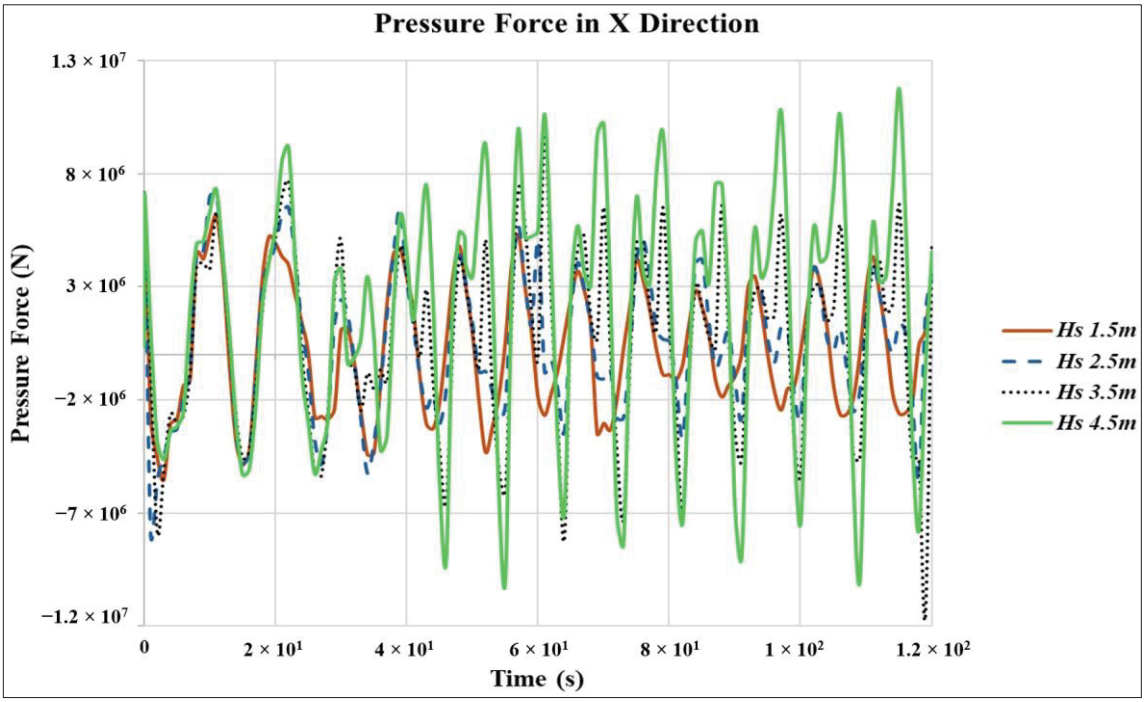

Figure 5.9 Pressure values in the x-direction applied to the Wave Dragon for different wave heights

The pressure distribution on the Wave Dragon is depicted in Figure 5.10a, which provides insight into the pressure forces acting on the structure. It is evident that the reflectors (curved arms) experience varying pressure levels, with higher pressures (green to yellow) concentrated near the base and lower surfaces, indicating stronger wave impact and flow resistance in these areas. The upper edges of the reflectors are mostly blue, implying low pressure due to reduced direct wave impact or flow separation effects. Moreover, the highest-pressure zones appear near the ramp's lower front edge and along certain reflectors' sections, indicating areas of significant hydrodynamic force concentration.

The pressure gradient suggests flow acceleration along the reflectors, supporting their role in guiding waves toward the central energy conversion system. Figure 5.10b shows the wall shear load distribution, where shear forces are higher near the base and edges of the reflectors due to flow interactions, aligning with the results of Figure 5.10a, as higher pressure corresponds to higher shear load. The highest shear load areas are near the junction of the reflectors with the main structure, suggesting stronger hydrodynamic effects at these points. These findings have significant engineering implications, as the reflectors must be designed to withstand shear forces in high-load areas while also optimizing their shape and material to enhance wave energy capture.

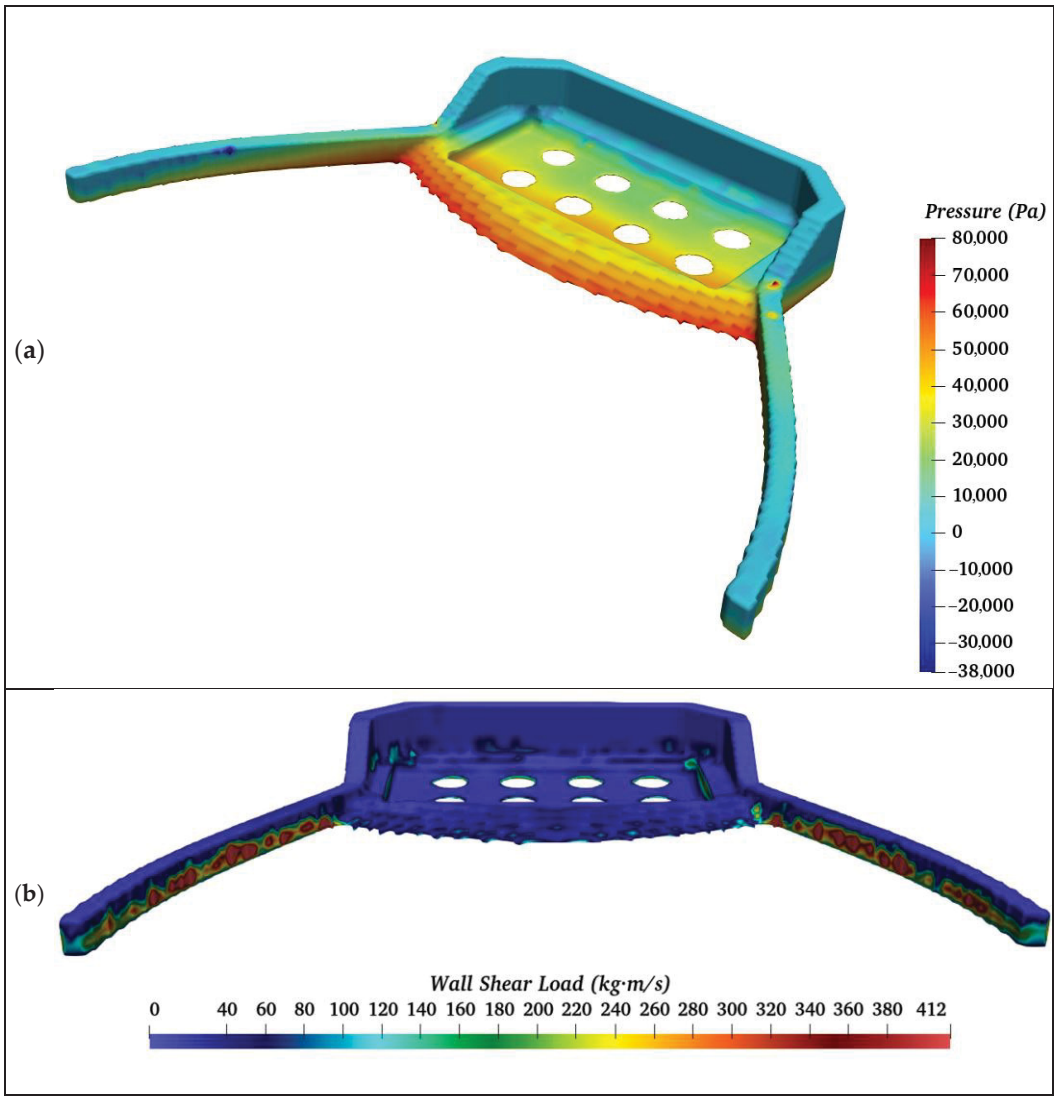

Figure 5.10 Pressure (a) and shear stress (b) distribution on the Wave Dragon structure

5.7 History Probes and Energy Generation Calculation

To quantify the flow passing through the turbines and the amount of generated energy, it was necessary to calculate the velocity of water passing through each turbine. The instantaneous power generated by each turbine could be determined by applying the appropriate formula. Given that the Wave Dragon is a dynamic structure, the most practical solution in FLOW-3D was to use history probes, which can track flow characteristics at specific points while attached to the Wave Dragon, unlike stationary baffles that do not move with the WEC. A total of 40 history probes were strategically placed, with five probes positioned within each turbine (Figure 5.11).

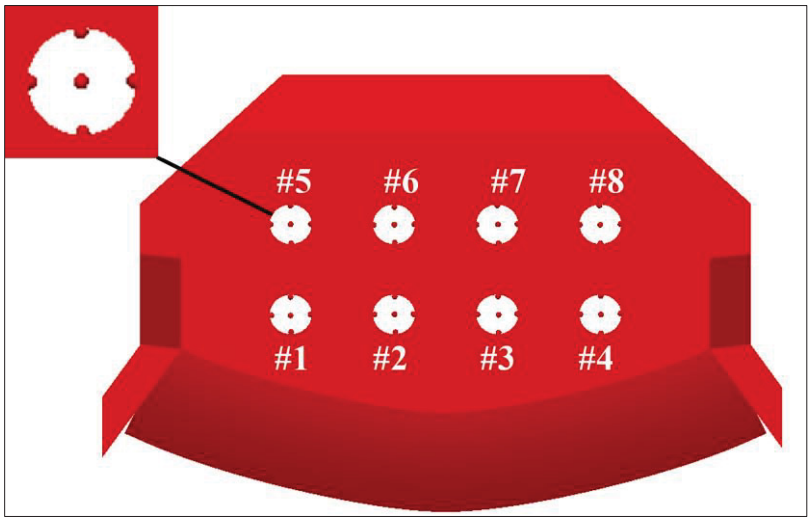

Figure 5.11 Placement of history probes within the turbines of the Wave Dragon for velocity measurement

A Kaplan turbine is a type of axial-flow turbine primarily designed for low-head hydroelectric installations. This turbine is particularly well-suited for situations where water flows continuously in one direction, such as in rivers or water channels (Frigaard et al., 2004), The area of each of the turbines with a diameter of 0.35 m can be calculated using the formula below, where D is the diameter of the turbine:

$$A = \frac{1}{4} \times \pi D^2 = \frac{1}{4} \times \pi \times 0.35^2 = 0.096\ m^2 \quad (5.6)$$

A computational study was conducted to estimate the energy generation potential under different wave scenarios over 120 s. According to standards for determining and modeling the motion of a structure under wave action, it is recommended to model at least 10 wave cycles. However, in this study, 12 cycles were modeled, 2 cycles more than the standard recommendation, to ensure the accuracy of the modeling (International Towing Tank Conference, ITTC, 2017). The procedure involved calculating the instantaneous velocity for each turbine based on the average readings from five velocity probes. These velocities were then used to compute the instantaneous power for each turbine using the equation below:

$$P(t) = 0.5 \times \rho \times A \times V(t)^3 \quad (5.7)$$

with ρ representing water density and A being the cross-sectional area of the turbines. An efficiency factor (η) of 90% for the Kaplan turbine was applied to reflect real-world turbine performance (M Odeh, 1999). The instantaneous power was integrated over the 120 s simulation period using the trapezoidal rule to determine the total energy generated by each turbine using the formula below:

$$E = \int_0^{120} P(t)dt \quad (5.8)$$

Where E is the integral of the instantaneous power and represents the total energy generated by a turbine over a period. Although this energy value corresponds to a brief interval, it can serve as a basis for extrapolating longer-term energy output. This approach allows for a preliminary assessment of the WEC system's potential in operational scenarios.

The results for varying significant wave heights (H_s) indicated that the power generation for different cases was 16.03, 25.95, 31.45, and 56.5 MWh per month for wave heights of 1.5, 2.5, 3.5, and 4.5 m, respectively. This demonstrates a direct relationship between wave height and

power output, as increased wave height allows a greater volume of water to enter the Wave Dragon reservoir and flow through the turbines, thereby enhancing energy conversion. This highlights the crucial role of wave height in optimizing energy production in wave energy systems. Moreover, these power output values show that a H_s of 4.5 m generates more than 50 MWh per month, slightly more than the expected power output of the Wave Dragon (Frigaard et al., 2006). However, the output power is relatively low for the other wave heights, possibly due to the lower wave heights and specific wave conditions like the wave period caused by wind patterns. Wind can significantly affect waves as there are no tides in the area, and the waves are wind-driven. Table 5.3 presents the energy generated by each of the eight turbines individually and the total output in kWh/day for different wave heights.

Table 5.3 Energy output (KWh/day) of the turbines for various wave heights

H_s(m)	**Turbine Number and Power Generated by Each Turbine (KWh/Day)**								**SUM (KWh/Day)**
	#1	**#2**	**#3**	**#4**	**#5**	**#6**	**#7**	**#8**	
1.5	62.7	62.8	136.05	16.63	182.3	15.39	45.27	13.2	534.38
2.5	52.06	14.38	17.24	68.16	10.18	199.9	317.05	185.93	865.03
3.5	57.35	79.85	96.29	28.16	240.46	68.15	45.07	433.17	1048.54
4.5	6.92	12.78	107.15	98.11	246.75	425.6	518.17	468.09	1883.6

5.8 Conclusions

Wave Energy Converters (WECs) are increasingly recognized as effective systems for harnessing wave energy. A 3D analysis is essential for gaining deeper insights into the interactions between WECs and the approaching waves, which is crucial for accurately assessing their energy production potential. This study models the Wave Dragon as a dynamic object, with mooring lines attached to the seabed, providing a more realistic simulation of its operation.

Based on experimental wave data, this study used FLOW-3D software to simulate a WEC device at different wave heights. Diagrams based on Stokes' 5th-order theory for intermediate waves were compared with the FLOW-3D simulation results for validation. The analysis revealed that the simulated waves aligned well with the theoretical values.

The results of pressure force analysis indicated a substantial rise as wave heights increase, with the lowest value recorded at 2.97 × 105 N for a 1.5 m wave and the highest reaching 1.95 × 106 N for a 4.5 m wave. This trend underscores the strong relationship between wave height and the pressure exerted on the device. The X-Z plane's velocity magnitude contours and velocity vectors demonstrate that the interaction between the wave crest and the structure generates significant flow acceleration and turbulence. Additionally, further back turbines experience higher velocities due to their position beyond the ramp, allowing for greater flow and potential increases in power generation. The analysis of different significant wave heights (H_s) revealed that monthly energy generation varied across cases, yielding 16.03, 25.95, 31.45, and 56.5 MWh for wave heights of 1.5, 2.5, 3.5, and 4.5 m, respectively. These results illustrate a clear correlation between wave height and energy output in Wave Dragons, demonstrating that higher waves significantly enhance energy generation, making wave height a critical factor in optimizing power production. Thus, the authors suggest that future studies explore Wave Dragon under various sea states with different wave heights to provide a more comprehensive understanding of its performance. Comparing Wave Dragon's efficiency with other wave energy devices could offer valuable insights.

CONCLUSION

This research addresses the escalating challenge of erosion, which is being exacerbated by climate change through rising sea levels, intensified storm activity, and increasingly variable flow regimes. These changes threaten the stability of both riverbanks and coastlines, with serious implications for infrastructure, ecosystems, and coastal communities. In response, this thesis adopts a dual-phase approach to erosion mitigation, targeting both riverine and coastal environments. The first phase centers on riverine erosion control through experimental analysis of stilling basins equipped with Multi-Horizontal Submerged Jets (MHSJ). The study examines how varying levels of submergence impact flow structures, energy dissipation, and shear stress distribution—critical parameters in preventing downstream scour and maintaining the structural integrity of hydraulic infrastructure. The second phase expands the scope to coastal regions, where the focus shifts to the deployment of Wave Energy Converters (WECs). Originally designed for renewable energy production, WECs are examined here for their dual function in sustainable development: harvesting marine energy while simultaneously reducing wave energy and sediment displacement.

The first article examines the hydrodynamics of flow downstream of submerged jets and river erosion. Laboratory velocity measurements were carried out to investigate the three-dimensional flow structure of submerged jets and assess the effects of downstream submergence on the flow field. The results indicated that Reynolds shear stress, vorticity magnitudes, and energy dissipation increased with greater jet submergence, leading to lower downstream erosion. Additionally, increasing submergence led to a 2.2% reduction in maximum bed (floor) shear stress and a 7.2% decrease in side-wall shear stress.

For the study of the dual function of Wave Energy Converters (WECs) in coastal protection and energy generation, it was shown that WECs contribute to wave height reduction, sediment deposition, and energy generation in coastal environments. Wave height reduction directly impacts shoreline stability, reducing erosion rates. When deployed in Palm Beach-Azur in Bou Ismail Bay, Algeria, WECs lowered shoaling coefficients as wave heights decreased by

approximately 0.3 meters. At the same time, sediment deposition increased by 0.8 meters, illustrating their effectiveness in shoreline protection.

Similarly, the influence of WEC configuration, placement, and orientation on wave and sediment dynamics was studied for the Astara port. Among the different setups, a staggered arrangement of 13 WECs oriented toward the dominant wave direction (northeast) proved the most effective. This specific configuration achieved wave height reductions of 23-25% in average conditions and up to 36.26% during peak storm events. In contrast, a linear configuration covering 47.88% of the coastline within the local model boundary was more beneficial in protecting longer stretches of the shoreline, suggesting that staggered setups offer localized protection, while linear arrangements extend coastal defense over a broader area. This result underscores the ability of WECs not only to harness energy but also to serve as adaptable coastal protection solutions. The flexibility of these configurations supports their use in diverse coastal environments tailored to both energy capture and shoreline management goals.

After the realization of the potential of WECs in coastal protection, detailed simulation of the Wave Dragon WEC, focusing on the relationship between wave height and energy output, was also performed. Results showed a direct correlation between wave height and power generation potential, with monthly energy outputs increasing from 16.03 MWh for 1.5 m waves to 56.5 MWh for 4.5 m waves.

Overall, this thesis demonstrates that MHSJ stilling basins have higher energy dissipation and lower downstream river erosion in higher submergences. Moreover, it was concluded that WECs can serve a dual role in energy production and coastal protection from erosion. The findings support their use in locations where both erosion control and renewable energy generation are priorities. WECs reduce the need for traditional erosion control structures and contribute to the coastal economy by harnessing marine energy. With optimized configurations, WECs can enhance coastal resilience against extreme weather events while

providing sustainable power, positioning them as versatile tools in coastal management and renewable energy portfolios.

Despite these findings, model limitations such as scale effects, temporal resolution, and uncertainties in bathymetry data should be acknowledged, as they may influence the accuracy of the results. Addressing these limitations can improve model reliability and practical applicability. Future research should focus on real-world monitoring campaigns to validate simulation results, AI-based optimization for WEC placement, and integrating social-ecological coastal resilience frameworks to address broader environmental and societal challenges.

BIBLIOGRAPHY

Abanades, J., Greaves, D., & Iglesias, G. (2015). Coastal defence using wave farms: The role of farm-to-coast distance. *Renewable Energy*, *75*, 572–582. https://doi.org/10.1016/J.RENENE.2014.10.048

Ahmad, M. F., Musa, M. A., Roslan, M. F., Giap, S. G. E., Ariffin, E. H., Eissa, Y. W. S. A., Salleh, M. H. M., & Alias, F. (2024). Study on Wave Overtopping Discharge Affected by Guiding Wall Angle of Wave Dragon Device Using FLOW-3D Software. *Journal of Advanced Research in Applied Sciences and Engineering Technology*, *41*(2), 208–222. https://doi.org/10.37934/ARASET.41.2.208222

Algeria - Summary | Climate Change Knowledge Portal. (n.d.). Retrieved November 3, 2024, from https://climateknowledgeportal.worldbank.org/country/algeria

Amini, E., Mehdipour, H., Faraggiana, E., Golbaz, D., Mozaffari, S., Bracco, G., & Neshat, M. (2022). Optimization of hydraulic power take-off system settings for point absorber wave energy converter. *Renewable Energy*, *194*, 938–954. https://doi.org/10.1016/J.RENENE.2022.05.164

Appendini, C. M., Urbano-Latorre, C. P., Figueroa, B., Dagua-Paz, C. J., Torres-Freyermuth, A., & Salles, P. (2015). Wave energy potential assessment in the Caribbean Low Level Jet using wave hindcast information. *Applied Energy*, *137*, 375–384. https://doi.org/10.1016/J.APENERGY.2014.10.038

Atan, R., Finnegan, W., Nash, S., & Goggins, J. (2019). The effect of arrays of wave energy converters on the nearshore wave climate. *Ocean Engineering*, *172*, 373–384. https://doi.org/10.1016/j.oceaneng.2018.11.043

Baird, W. F., & Hall, K. R. (1985). DESIGN OF BREAKWATERS USING QUARRIED STONES. *Proceedings of the Coastal Engineering Conference*, *3*, 2580–2591. https://doi.org/10.1061/9780872624382.174/ASSET/A198C8CC-31F5-429A-B98E-A202B8D914FC/ASSETS/9780872624382.174.FP.PNG

Balachandar, R., & Bhuiyan, F. (2007). Higher-Order Moments of Velocity Fluctuations in an Open-Channel Flow with Large Bottom Roughness. *Journal of Hydraulic Engineering*, *133*(1), 77–87. https://doi.org/10.1061/(ASCE)0733-9429(2007)133:1(77)

Battjes, J. A., & Janssen, J. P. F. M. (1978). Energy Loss and Set-Up Due to Breaking of Random Waves. *Coastal Engineering 1978*, 569–587. https://doi.org/10.1061/9780872621909.034

Bayon, A., Moradi, M., Sajjadi, M., & Valles-Morán, F. (2019). Numerical modeling of multi-horizontal submerged jets (MHSJ) stilling basins using CFD techniques. *In 38th IAHR World Congress. Panama City: Panamá*, 3495–3504.

Belkacem, Y. (2010). *Intégration des mesures in situ et des données satellitaires dans un système d'information géographique pour caractériser les eaux côtières*. (Doctoral dissertation).

Bevilacqua, G., & Zanuttigh, B. (2011). Overtopping Wave Energy Converters: general aspects and stage of development. *Coast Eng. Proc. 21,* 1–21. http://amsacta.unibo.it/3062/1/overtopping_devicex.pdf.

Bilgen, S., Kaygusuz, K., & Sari, A. (2004). Renewable Energy for a Clean and Sustainable Future. *Energy Sources*, *26*(12), 1119–1129. https://doi.org/10.1080/00908310490441421

Booij, N., Ris, R. C., & Holthuijsen, L. H. (1999). A third-generation wave model for coastal regions: 1. Model description and validation. *Journal of Geophysical Research: Oceans*, *104*(C4), 7649–7666. https://doi.org/10.1029/98JC02622

Cao, D., He, J., & Chen, H. (2024). Empirical Predictions on Wave Overtopping for Overtopping Wave Energy Converters: A Systematic Review. *Processes 2024, Vol. 12*, *12*(9), 1940. https://doi.org/10.3390/PR12091940

Carballo, R., & Iglesias, G. (2013). Wave farm impact based on realistic wave-WEC interaction. *Energy*, *51*, 216–229. https://doi.org/10.1016/J.ENERGY.2012.12.040

Castillo, L. G., Carrillo, J. M., & Carrillo, J. M. (2012). Numerical simulation and validation of intake systems with CDF methodology. *In Proceedings of the 2nd IAHR European Congress, Munich, Germany*, 27–29.

Chachereau, Y., & Chanson, H. (2011). Free-surface fluctuations and turbulence in hydraulic jumps. *Experimental Thermal and Fluid Science*, *35*(6), 896–909. https://doi.org/10.1016/J.EXPTHERMFLUSCI.2011.01.009

Chang, G., Ruehl, K., Jones, C. A., Roberts, J., & Chartrand, C. (2016). Numerical modeling of the effects of wave energy converter characteristics on nearshore wave conditions. *Renewable Energy*, *89*, 636–648. https://doi.org/10.1016/J.RENENE.2015.12.048

Chanson, H. (2013). Hydraulics of aerated flows: Qui pro quo? *Journal of Hydraulic Research*, *51*(3), 223–243.

Chanson, H. (2015). *Energy dissipation in hydraulic structures*. CRC Press, Taylor & Francis Group, London, UK.

Chanson, H., & Manasseh, R. (2003). Air entrainment processes in a circular plunging jet: Void-fraction and acoustic measurements. *Journal of Fluids Engineering*, *125*(5), 910–921. https://doi.org/10.1115/1.1595672

Chen, J. G., Zhang, J. M., Xu, W. L., Li, S., & He, X. L. (2013). Particle image velocimetry measurements of vortex structures in stilling basin of multi-horizontal submerged jets. *Journal of Hydrodynamics 2013 25:4*, *25*(4), 556–563. https://doi.org/10.1016/S1001-6058(11)60396-0

Chen, J. G., Zhang, J. M., Xu, W. L., & Peng, Y. (2013). Characteristics of the Velocity Distribution in a Hydraulic Jump Stilling Basin with Five Parallel Offset Jets in a Twin-Layer Configuration. *Journal of Hydraulic Engineering*, *140*(2), 208–217. https://doi.org/10.1061/(ASCE)HY.1943-7900.0000817

Chen, J. G., Zhang, J. M., Xu, W. L., & Wang, Y. R. (2010). Numerical simulation of the energy dissipation characteristics in stilling basin of multi-horizontal submerged jets. *Journal of Hydrodynamics*, *22*(5), 732–741. https://doi.org/10.1016/S1001-6058(09)60110-4/METRICS

Chen, J. G., Zhang, J. M., Xu, W. L., & Wang, Y. R. (2010). Scale effects of air-water flows in stilling basin of multi-horizontal submerged jets. *Journal of Hydrodynamics*, *22*(6), 788–795. https://doi.org/10.1016/S1001-6058(09)60117-7

Choupin, O., Pinheiro Andutta, F., Etemad-Shahidi, A., & Tomlinson, R. (2021). A decision-making process for wave energy converter and location pairing. *Renewable and Sustainable Energy Reviews*, *147*, 111225. https://doi.org/10.1016/J.RSER.2021.111225

Clemente, D., Rosa-Santos, P., & Taveira-Pinto, F. (2021). On the potential synergies and applications of wave energy converters: A review. *Renewable and Sustainable Energy Reviews*, *135*, 110162. https://doi.org/10.1016/J.RSER.2020.110162

Contardo, S., Hoeke, R., Hemer, M., Symonds, G., McInnes, K., & O'Grady, J. (2018). In situ observations and simulations of coastal wave field transformation by wave energy converters. *Coastal Engineering*, *140*, 175–188. https://doi.org/10.1016/J.COASTALENG.2018.07.008

Darmawi, Sipahutar, R., Bernas, S. M., & Imanuddin, M. S. (2013). Renewable energy and hydropower utilization tendency worldwide. *Renewable and Sustainable Energy Reviews*, *17*, 213–215. https://doi.org/10.1016/J.RSER.2012.09.010

Deng, J., Xu, W., Zhang, J., Qu, J., & Yang, Y. (2008). A new type of plunge pool-Multi-horizontal submerged jets. *Science in China, Series E: Technological Sciences*, *51*(12), 2128–2141. https://doi.org/10.1007/S11431-008-0237-Z

Dey, S., Nath, T. K., & Bose, S. K. (2010). Fully rough submerged plane wall-jets. *Journal of Hydro-Environment Research*, *4*(4), 301–316. https://doi.org/10.1016/J.JHER.2010.01.002

DHI MIKE. MIKE 21 Spectral Waves FM, Spectral Wave Module User Guide: Hørsholm, Denmark,. (2017). *DHI Water Environment Health*.

Di Lauro, E., Maza, M., Lara, J. L., Losada, I. J., Contestabile, P., & Vicinanza, D. (2020). Advantages of an innovative vertical breakwater with an overtopping wave energy converter. *Coastal Engineering*, *159*, 103713. https://doi.org/10.1016/J.COASTALENG.2020.103713

Drew, B., Plummer, A. R., & Sahinkaya, M. N. (2016). A review of wave energy converter technology. *Http://Dx.Doi.Org/10.1243/09576509JPE782*, *223*(8), 887–902. https://doi.org/10.1243/09576509JPE782

Dugué, V., Blanckaert, K., Chen, Q., & Schleiss, A. J. (2015). Influencing Flow Patterns and Bed Morphology in Open Channels and Rivers by Means of an Air-Bubble Screen. *Journal of Hydraulic Engineering*, *141*(2). https://doi.org/10.1061/(ASCE)HY.1943-7900.0000946

Ervine, D. A., & Falvey, H. T. (1987). Behaviour of turbulent water jets in the atmosphere and in plunge pools. *Proceedings of the Institution of Civil Engineers*, *83*(1), 295–314. https://doi.org/10.1680/IICEP.1987.353

Eskilsson, C., Eskilsson, C., Palm, J., Kofoed, J. P., & Friis-Madsen, E. (2015). CFD study of the overtopping discharge of the Wave Dragon wave energy converter. *Renewable Energies Offshore*, 287–294. https://doi.org/10.1201/b18973-42

Falcão, A. F. de O. (2010). Wave energy utilization: A review of the technologies. *Renewable and Sustainable Energy Reviews*, *14*(3), 899–918. https://doi.org/10.1016/J.RSER.2009.11.003

Falnes, J. (2007). A review of wave-energy extraction. *Marine Structures*, *20*(4), 185–201. https://doi.org/10.1016/J.MARSTRUC.2007.09.001

Fernandez, H., Iglesias, G., Carballo, R., Castro, A., Fraguela, J. A., Taveira-Pinto, F., & Sanchez, M. (2012). The new wave energy converter WaveCat: Concept and laboratory tests. *Marine Structures*, *29*(1), 58–70. https://doi.org/10.1016/j.marstruc.2012.10.002

Flow Science, Inc., FLOW-3D User Manual. (n.d.). *Version 9.3*.

Flow-3D® Version 2023R1 [Computer software]. (2023). https://www.flow3d.com. (n.d.). *Santa Fe, NM: Flow Science, Inc.*

Frigaard, P., Kofoed, J. P., & Knapp, W. (2004). Wave Dragon: wave power plant using low-head turbines. *In Hidroenergia 04: International Conference and Exhibition on Small Hydropower*.

Frigaard, P., Tedd, J., & JP, K. (2006). 3 years experience with energy production on the Nissum Bredning Wave Dragon prototype. *Proceedings of the Fourth CA-OE Workshop: Performance Monitoring of Ocean*, 16–17.

Gao, J., Ma, X., Zang, J., Dong, G., Ma, X., Zhu, Y., & Zhou, L. (2020). Numerical investigation of harbor oscillations induced by focused transient wave groups. *Coastal Engineering*, *158*, 103670. https://doi.org/10.1016/J.COASTALENG.2020.103670

Gao, J., Shi, H., Zang, J., & Liu, Y. (2023). Mechanism analysis on the mitigation of harbor resonance by periodic undulating topography. *Ocean Engineering*, *281*, 114923. https://doi.org/10.1016/J.OCEANENG.2023.114923

Garcia, C., & Canals, M. (2015). Wave energy resource assessment and recoverable wave energy in Puerto Rico and the US Virgin Islands. *MTS/IEEE OCEANS 2015 - Genova: Discovering Sustainable Ocean Energy for a New World*. https://doi.org/10.1109/OCEANS-GENOVA.2015.7271639

GEBCO. (n.d.). *GEBCO - The General Bathymetric Chart of the Oceans*. Retrieved January 5, 2022, from https://www.gebco.net/

Gonçalves, M., Martinho, P., & Guedes Soares, C. (2014). Wave energy conditions in the western French coast. *Renewable Energy*, *62*, 155–163. https://doi.org/10.1016/J.RENENE.2013.06.028

Greaves, D., & Iglesias, G. (2017). Wave and tidal energy. *Wave and Tidal Energy*, 1–691. https://doi.org/10.1002/9781119014492

Guiberteau, K., Lee, J., Liu, Y., Dou, Y., & Kozman, T. A. (2015). Wave Energy Converters and Design Considerations for Gulf of Mexico. *Distributed Generation & Alternative Energy Journal*, *30*(4), 55–76. https://doi.org/10.1080/21563306.2015.11667613

Guiberteau, K., Liu, Y., Lee, J., & Kozman, T. (2012). Investigation of Developing Wave Energy Technology In the Gulf of Mexico. *Distributed Generation & Alternative Energy Journal*, *27*(4), 36–52. https://doi.org/10.1080/21563306.2012.10554221

Guillou, N., & Chapalain, G. (2015). Numerical modelling of nearshore wave energy resource in the Sea of Iroise. *Renewable Energy*, *83*, 942–953. https://doi.org/10.1016/J.RENENE.2015.05.021

Guo, B., Wang, T., Jin, S., Duan, S., Yang, K., & Zhao, Y. (2022). A Review of Point Absorber Wave Energy Converters. *Journal of Marine Science and Engineering 2022, Vol. 10, Page 1534*, *10*(10), 1534. https://doi.org/10.3390/JMSE10101534

Harman, B. P., Heyenga, S., Taylor, B. M., & Fletcher, C. S. (2015). Global Lessons for Adapting Coastal Communities to Protect against Storm Surge Inundation. *Journal of Coastal Research*, *31*(4), 790–801. https://doi.org/10.2112/JCOASTRES-D-13-00095.1

Holthuijsen, L. H., Booij, N., & Herbers, T. H. C. (1989). A prediction model for stationary, short-crested waves in shallow water with ambient currents. *Coastal Engineering*, *13*(1), 23–54. https://doi.org/10.1016/0378-3839(89)90031-8

Houma, F. B. (2009). Modélisation et cartographie de la pollution marine et de la bathymétrie à partir de l'imagerie satellitaire [Université Paris-Est].

Iglesias, G., & Carballo, R. (2009a). Wave energy potential along the Death Coast (Spain). *Energy*, *34*(11), 1963–1975. https://doi.org/10.1016/J.ENERGY.2009.08.004

Iglesias, G., & Carballo, R. (2009b). Wave energy potential along the Death Coast (Spain). *Energy*, *34*(11), 1963–1975. https://doi.org/10.1016/J.ENERGY.2009.08.004

Iglesias, G., & Carballo, R. (2014). Wave farm impact: The role of farm-to-coast distance. *Renewable Energy*, *69*, 375–385. https://doi.org/10.1016/J.RENENE.2014.03.059

International Towing Tank Conference (ITTC). (2017). Recommended Procedures and Guidelines: Procedure for Seakeeping Experiments (7.5-02-07-02.1). ITTC Quality System Manual, Revision 6. (n.d.).

ISWM, Iranian Sea Wave Modeling. (2008). Technical report, Iranian sea wave modeling. Phase 3, ports and maritime organization. (n.d.).

Jafari, M., Babajani, A., Hafezisefat, P., Mirhosseini, M., Rezania, A., & Rosendahl, L. (2018). Numerical simulation of a novel ocean wave energy converter. *Energy Procedia*, *147*, 474–481. https://doi.org/10.1016/J.EGYPRO.2018.07.050

Khan, A., Xie, W., & Liu, L. W. (2020). Set-Membership Interval State Estimator Design Using Observability Matrix for Discrete-Time Switched Linear Systems. *IEEE Sensors Journal*, *20*(11), 6121–6129. https://doi.org/10.1109/JSEN.2020.2972315

Khan, A., Xie, W., Zhang, B., & Liu, L. W. (2021). A survey of interval observers design methods and implementation for uncertain systems. *Journal of the Franklin Institute*, *358*(6), 3077–3126. https://doi.org/10.1016/J.JFRANKLIN.2021.01.041

Kofoed, J. P., Frigaard, P., Friis-Madsen, E., & Sørensen, H. C. (2006). Prototype testing of the wave energy converter wave dragon. *Renewable Energy*, *31*(2), 181–189. https://doi.org/10.1016/J.RENENE.2005.09.005

Kofoed, J. P., Frigaard, P., Sorenson, H. C., & Friis-Madsen, E. (2000). *Development of the Wave Energy Converter - Wave Dragon*. OnePetro. https://dx.doi.org/

Lama, G. F. C., Sadeghifar, T., Azad, M. T., Sihag, P., & Kisi, O. (2022). On the Indirect Estimation of Wind Wave Heights over the Southern Coasts of Caspian Sea: A Comparative Analysis. *Water 2022, Vol. 14, Page 843*, *14*(6), 843. https://doi.org/10.3390/W14060843

Lian, J., Zhang, W., Guo, Q., & Liu, F. (2016). Generation Mechanism and Prediction Model for Low Frequency Noise Induced by Energy Dissipating Submerged Jets during Flood Discharge from a High Dam. *International Journal of Environmental Research and Public Health 2016, Vol. 13, Page 594*, *13*(6), 594. https://doi.org/10.3390/IJERPH13060594

Liao, Z., Sun, T., Al-Ani, M., Jordan, L. B., Li, G., Wang, Z., Belmont, M., & Edwards, C. (2023). Modelling and Control Tank Testing Validation for Attenuator Type Wave Energy Converter - Part I: Experiment Setup and Control-Oriented Modelling. *IEEE Transactions on Sustainable Energy*, *14*(3), 1747–1757. https://doi.org/10.1109/TSTE.2023.3246172

Liu, M., Rajaratnam, N., & Zhu, D. Z. (2004). Turbulence structure of hydraulic jumps of low Froude numbers. *Journal of Hydraulic Engineering*, *130*(6), 511–520. https://doi.org/10.1061/(ASCE)0733-9429(2004) 130:6(511)

Liu, Z., Shi, H., Cui, Y., & Kim, K. (2017). Experimental study on overtopping performance of a circular ramp wave energy converter. *Renewable Energy*, *104*, 163–176. https://doi.org/10.1016/J.RENENE.2016.12.040

López, I., Andreu, J., Ceballos, S., Martínez De Alegría, I., & Kortabarria, I. (2013). Review of wave energy technologies and the necessary power-equipment. *Renewable and Sustainable Energy Reviews*, *27*, 413–434. https://doi.org/10.1016/J.RSER.2013.07.009

Luczko, E., Robertson, B., Bailey, H., Hiles, C., & Buckham, B. (2018). Representing non-linear wave energy converters in coastal wave models. *Renewable Energy*, *118*, 376–385. https://doi.org/10.1016/J.RENENE.2017.11.040

M Odeh. (1999). A summary of environmentally friendly turbine design concepts. *US Department of Energy Idaho Operations Office*. https://www.academia.edu/download/106994601/doeid-13741.pdf

Matamala, P., Gallardo, Parra, C., Ahumada, J. M., Cifuentes, C., González, F., & Tampier, G. (2023). Numerical and experimental assessment of the hydrodynamic behaviour of an attenuator wave energy converter device. *Trends in Renewable Energies Offshore - Proceedings of the 5th International Conference on Renewable Energies Offshore, RENEW 2022*, 241–249. https://doi.org/10.1201/9781003360773-28

McCormick, M. E. (2007). *Ocean wave energy conversion*. 233.

Mendes, R. P. G., Calado, M. R. A., & Mariano, S. J. P. S. (2012). Wave energy potential in Portugal–Assessment based on probabilistic description of ocean waves parameters. *Renewable Energy*, *47*, 1–8. https://doi.org/10.1016/J.RENENE.2012.04.009

Mi, C., Gao, J., Song, Z., & Liu, Y. (2025). Hydrodynamic wave forces on two side-by-side barges subjected to nonlinear focused wave groups. *Ocean Engineering*, *317*, 120056. https://doi.org/10.1016/J.OCEANENG.2024.120056

Moradi, M., Chertouk, N., & Ilinca, A. (2022). Modelling of a Wave Energy Converter Impact on Coastal Erosion, a Case Study for Palm Beach-Azur, Algeria. *Sustainability (Switzerland)*, *14*(24), 16595. https://doi.org/10.3390/SU142416595

Moradi, M., & Ilinca, A. (2024). Impact of Wave Energy Converters and Port Layout on Coastal Dynamics: Case Study of Astara Port. *Energies 2024, Vol. 17, Page 2485*, *17*(11), 2485. https://doi.org/10.3390/EN17112485

Moradi, M., Sajjadi, M., Balachandar, R., Arman, A., & Ilinca, A. (2022). Experimental analysis of multi-horizontal submerged jets energy dissipater. *ISH Journal of Hydraulic Engineering*, *28*(3), 281–291. https://doi.org/10.1080/09715010.2021.1885508

Murzyn, F., & Chanson, H. (2009). Free-surface fluctuations in hydraulic jumps: Experimental observations. *Experimental Thermal and Fluid Science*, *33*(7), 1055–1064. https://doi.org/10.1016/J.EXPTHERMFLUSCI.2009.06.003

Nader, J. R., Fleming, A., Macfarlane, G., Penesis, I., & Manasseh, R. (2017). Novel experimental modelling of the hydrodynamic interactions of arrays of wave energy converters. *International Journal of Marine Energy*, *20*, 109–124. https://doi.org/10.1016/J.IJOME.2017.11.003

Newmann, J. N. (2018). *Marine Hydromechanics*. The MIT press.

Nørgaard, J. H., Andersen, T. L., & Kofoed, J. P. (2013). *WAVE DRAGON WAVE ENERGY CONVERTERS USED AS COASTAL PROTECTION*. 83–94. https://doi.org/10.1142/9789814412216_0008

Pastor, J., & Liu, Y. (2016). Wave Climate Resource Analysis Based on a Revised Gamma Spectrum for Wave Energy Conversion Technology. *Sustainability 2016, Vol. 8, Page 1321*, *8*(12), 1321. https://doi.org/10.3390/SU8121321

Peter, J., Dimon, J., Tedd, J., Kofoed, J. P., Jasinski, M., Morris, A., Friis-Madsen, E., Wisniewski, R., & Bendtsen, J. D. (2007). Advanced Control Techniques for WEC Wave Dragon. *In Proceedings of the 7th European Wave and Tidal Energy Conference: EWTEC 2007. European Ocean Energy Association.*

Peter, J., Tedd, J., Kofoed, J., Knapp, W., Friis-Madsen, E., & Sørensen, H. (2006). Wave Dragon: prototype wave power production. *In Proceedings of the 9th World Renewable Energy Congress: WREC IX, Florence, Italy. Pergamon Press.*

Ports and Maritime Organization (PMO). (2010). The Directorate General of Coasts and Ports, Modeling of sea waves Iran, Volume Two, the Persian Gulf and Sea of Oman. (n.d.).

Putnam, J. A., & Johson, J. W. (1949). The dissipation of wave energy by bottom friction. *Eos, Transactions American Geophysical Union*, *30*(1), 67–74. https://doi.org/10.1029/TR030I001P00067

Qingchao, L., & Drewes, U. (1994). Turbulence characteristics in free and forced hydraulic jumps. *Journal of Hydraulic Research*, *32*(6), 877–898. https://doi.org/10.1080/00221689409498696

Rajaratnam, N. (1965). The Hydraulic Jump as a Well Jet. *Journal of the Hydraulics Division*, *91*(5), 107–132. https://doi.org/10.1061/JYCEAJ.0001299

Rajaratnam, N. (1962). An experimental study of air entrainment characteristics of the hydraulic jump. *Journal of Inst Eng India*, *42*(7), 247–273.

Rajaratnam, N. (1976). *Turbulent jets. Elsevier.* Elsevier Scientific Publishing Company, Amsterdam, The Netherlands. Vol. 5.

Robertson, B. (2010). Ocean wave energy generation on the west coast of Vancouver island and the queen charlotte islands. *Guelph Eng*, 9–18.

Rodionov, S. N. (1994). *Global and Regional Climate Interaction: The Caspian Sea Experience* (Vol. 11). Springer Science & Business Media.

Ruol, P., Zanuttigh, B., Martinelli, L., Kofoed, J. P., & Frigaard, P. (2011). *Near-Shore Floating Wave Energy Converters: applications for coastal protection*. Coastal Engineering Research Council. https://vbn.aau.dk/en/publications/near-shore-floating-wave-energy-converters-applications-for-coast

Sierra, J. P., Martín, C., Mösso, C., Mestres, M., & Jebbad, R. (2016). Wave energy potential along the Atlantic coast of Morocco. *Renewable Energy*, *96*, 20–32. https://doi.org/10.1016/J.RENENE.2016.04.071

Smith, H. C. M., Pearce, C., & Millar, D. L. (2012). Further analysis of change in nearshore wave climate due to an offshore wave farm: An enhanced case study for the Wave Hub site. *Renewable Energy*, *40*(1), 51–64. https://doi.org/10.1016/J.RENENE.2011.09.003

Soares, C. G., Bhattacharjee, J., Tello, M., & Pietra, L. (2012). Review and classification of wave energy converters. *Maritime Engineering and Technology, Taylor & Francis Group London, UK*, 585–594.

Soerensen, H. C., Friis-Madsen, E., Panhauser, W., Dunce, D., Nedkvintne, J., Frigaard, P. B., Kofoed, J. P., Knapp, W., Riemann, S., Holmén, E., Raulund, A., Praest, J., Hansen, L. K., Christensen, L., Nöhrlind, T., Bree, T., & McCullen, P. (2003). *Development of Wave Dragon from Scale 1:50 to Prototype*.

Song, Z., Jiao, Z., Gao, J., Mi, C., & Liu, Y. (2025). Numerical investigation on the hydrodynamic wave forces on the three barges in proximity. *Ocean Engineering*, *316*, 119941. https://doi.org/10.1016/J.OCEANENG.2024.119941

SSMO, S. of S. M. O. (n.d.). *Summary of synoptic meteorological observations (SSMO) : Central American coastal marine areas, west... | National Library of Australia*. Retrieved January 5, 2022, from https://catalogue.nla.gov.au/Record/641700

SWAN User Manual. (2022). Delft University of Technology. Available online: https://swanmodel.sourceforge.io/. (n.d.).

Tedd, J., & Peter Kofoed, J. (2009). Measurements of overtopping flow time series on the Wave Dragon, wave energy converter. *Renewable Energy*, *34*(3), 711–717. https://doi.org/10.1016/J.RENENE.2008.04.036

Thorpe, T. W. (1999). *A Brief Review of Wave Energy. A report produced for the UK Department of Trade and Industry.*

Vaidya, A. M., Kori, S. K., & Kudale, M. D. (2015). Shoreline Response to Coastal Structures. *Aquatic Procedia*, *4*, 333–340. https://doi.org/10.1016/J.AQPRO.2015.02.045

Vicinanza, D., Margheritini, L., Kofoed, J. P., & Buccino, M. (2012). The SSG Wave Energy Converter: Performance, Status and Recent Developments. *Energies 2012, Vol. 5, Pages 193-226*, *5*(2), 193–226. https://doi.org/10.3390/EN5020193

Wallace, J. M., Eckelmann, H., & Brodkey, R. S. (1972). The wall region in turbulent shear flow. *Journal of Fluid Mechanics*, *54*(1), 39–48. https://doi.org/10.1017/S0022112072000515

Wang, H., & Chanson, H. (2015). Air entrainment and turbulent fluctuations in hydraulic jumps. *Urban Water Journal*, *12*(6), 502–518. https://doi.org/10.1080/1573062X.2013.847464

Wang, J., Wang, S. qi, Jiang, Q. dian, Xu, Y. xin, & Shi, W. chao. (2023). Effect of Different Raft Shapes on Hydrodynamic Characteristics of the Attenuator-Type Wave Energy Converter. *China Ocean Engineering*, *37*(4), 645–659. https://doi.org/10.1007/S13344-023-0055-X/METRICS

Wang, K., Jin, S., & Liu, G. (2009). Numerical modelling of free-surface flows with bottom and surface-layer pressure treatment. *Journal of Hydrodynamics, Ser. B*, *21*(3), 352–359. https://doi.org/10.1016/S1001-6058(08)60156-0

Witt, A., Gulliver, J., & Shen, L. (2015). Simulating air entrainment and vortex dynamics in a hydraulic jump. *International Journal of Multiphase Flow, Elsevier*, *72*, 165–180.

Wu, J. H., & Ai, W. Z. (2010). Flows through energy dissipaters with sudden reduction and sudden enlargement forms. *Journal of Hydrodynamics, Ser. B*, *22*(3), 360–365. https://doi.org/10.1016/S1001-6058(09)60065-2

Yang, L., Lyu, Z., Yang, P., Pavlidis, D., Fang, F., Xiang, J., Latham, J.-P., & Pain, C. (2018). *Numerical Simulation of Attenuator Wave Energy Converter Using One-Fluid Formulation*. OnePetro. https://dx.doi.org/

Zemenzer, S. (2024). Ensablement du port par transport sédimentaire simulation et application du modèle de Gao et Collins (1994) au port de Sidi Fredj. *Mémoire d'ingéniorat, Institut de Sciences de La Mer et de l'Aménagement Du Littoral: Dély Ibrahim, Alger.*

Zhang, G., Wang, H., & Chanson, H. (2013). Turbulence and aeration in hydraulic jumps: Free-surface fluctuation and integral turbulent scale measurements. *Environmental Fluid Mechanics*, *13*(2), 189–204. https://doi.org/10.1007/S10652-012-9254-3/METRICS

Zhang, J. M., Chen, J. G., Peng, Y., & Xu, W. L. (2014). Characteristics of vortex structure in multi-horizontal submerged jets stilling basin. *Proceedings of the Institution of Civil Engineers: Water Management*, *167*(6), 322–333. https://doi.org/10.1680/WAMA.12.00071

Zhang, J. M., Chen, J. G., Xu, W. L., Wang, Y. R., & Li, G. J. (2011). Three-dimensional numerical simulation of aerated flows downstream sudden fall aerator expansion-in a tunnel. *Journal of Hydrodynamics*, *23*(1), 71–80. https://doi.org/10.1016/S1001-6058(10)60090-X/METRICS

Zhang, J., Peng, Y., & Xu, W. (2017). Hydraulic Prediction of Near-Field Vibrations Induced by Releasing Flood. *Journal of Hydraulic Engineering*, *143*(9), 05017002. https://doi.org/10.1061/(ASCE)HY.1943-7900.0001310

Zhang, N., Zhang, X., Xiao, L., Wei, H., & Chen, W. (2021). Evaluation of long-term power capture performance of a bistable point absorber wave energy converter in South China Sea. *Ocean Engineering*, *237*, 109338. https://doi.org/10.1016/J.OCEANENG.2021.109338

Zurkinden, A. S., Ferri, F., Beatty, S., Kofoed, J. P., & Kramer, M. M. (2014). Non-linear numerical modeling and experimental testing of a point absorber wave energy converter. *Ocean Engineering*, *78*, 11–21. https://doi.org/10.1016/J.OCEANENG.2013.12.009